

Incorporation of the Effects of Future Anthropogenically Forced Climate Change in Intensity-Duration-Frequency Design Values

SERDP project number:
RC-2517

Performing institution:
North Carolina Institute for Climate Studies (NCICS)
North Carolina State University

Lead principal investigator:
Dr. Kenneth E. Kunkel

Date and version:
September 4, 2020
Version 2

Table of Contents

Table of Contents.....	i
List of Figures.....	iv
List of Tables	viii
Acronyms and Abbreviations.....	ix
Keywords	xii
Acknowledgements	xiii
Abstract.....	1
Objectives.....	1
Technical Approach.....	1
Results	2
Benefits	2
Objective.....	3
1. SERDP Relevance	3
2. Technical Objective.....	3
Background.....	5
Exclusive Use of Recent Historical Data.....	6
Historical Observations Calibrated to GCMs for a Simulated Future.....	6
Historical Observations Calibrated to the Best GCMs	7
Preferred Approach in This Work	7
Material and Methods	9
General	9
Datasets.....	11
Reanalysis.....	11
Precipitation.....	12
Meteorological Fronts.....	12
GCM Simulations	13
Regional Definitions	15
Task 1: Perform a historical analysis of U.S. and global trends in precipitation in the range of frequencies and durations of relevance to civil engineers (e.g., NOAA NWS 2020 covers ARIs of 1 through 1,000 years and durations of 5 min through 60 days).	16
Task 2: Modify existing software and develop new software to automatically identify key weather systems that cause heavy precipitation in historical reanalyses and climate model simulations.	19
North American Monsoon.....	19
Water Vapor	19
Extratropical Cyclones.....	19
Fronts	19
Task 3: Perform a thorough analysis of the meteorological causes of heavy precipitation increases over the last few decades, building on previous work.	25
North American Monsoon.....	25
Water vapor	26
Weather Systems	27

Task 4: Perform extensive analyses of CMIP5 model simulations, identifying the occurrence of weather systems causing heavy precipitation for historical and future simulations.	28
Precipitation.....	28
North American Monsoon.....	28
Water Vapor	28
Fronts	29
Extratropical Cyclones.....	29
Task 5: Determine the meteorological causes and trends of heavy precipitation events at global military installation sites identified by DoD.	31
Station Selection	32
Methods and Analysis.....	32
Task 6: Develop applications, including adjustment factors for current IDF values, and incorporate them into the delivery mechanism for current IDF values to provide convenient and reliable access to appropriate values by the civil engineering community.	34
Results and Discussion	36
Task 1: Perform a historical analysis of U.S. and global trends in precipitation in the range of frequencies and durations of relevance to civil engineers (e.g., NOAA NWS 2020 covers ARIs of 1 through 1,000 years and durations of 5 min through 60 days).	36
United States.....	36
Water Vapor Trends.....	39
Summary	39
Global Analysis	40
Task 2: Modify existing software and develop new software to automatically identify key weather systems that cause heavy precipitation in historical reanalyses and climate model simulations.	41
Fronts	41
Task 3: Perform a thorough analysis of the meteorological causes of heavy precipitation increases over the last few decades, building on previous work.	46
Water Vapor	46
Summer Fronts	56
Weather Systems	57
Extratropical Cyclones.....	65
North American Monsoon.....	66
Task 4: Perform extensive analyses of CMIP5 model simulations, identifying the occurrence of weather systems causing heavy precipitation for historical and future simulations.	68
Precipitation.....	68
North American Monsoon.....	71
Water Vapor	71
Fronts	73
Extratropical Cyclones.....	74
Task 5: Determine the meteorological causes and trends of heavy precipitation events at global military installation sites identified by DoD.	75

Task 6: Develop applications, including adjustment factors for current IDF values, and incorporate them into the delivery mechanism for current IDF values to provide convenient and reliable access to appropriate values by the civil engineering community.	77
Water Vapor Adjustment Component	77
Weather System Adjustment Component	78
Uncertainty Range	80
Sub-Daily Duration Adjustments	82
Website.....	82
Conclusions and Implications for Future Research/Implementation.....	85
Literature Cited.....	88
Appendices.....	93
Supporting Data	93
Additional Water Vapor Analyses.....	93
Scientific/Technical Publications.....	103

List of Figures

Figure 1. IDF curves for a rain gauge in Lafayette, Louisiana (Latitude: 30.2050, Longitude: -91.9875) (Source: NOAA NWS 2020).....	5
Figure 2. The National Centers for Environmental Information (NCEI) climate regions used in this study. Abbreviations for the regional titles are: Northwest — NW; West North Central — WNC; East North Central — ENC; Northeast — NE; West — W; Southwest — SW; South — S; Central — C; Southeast — SE.	15
Figure 3. $10^{\circ} \times 10^{\circ}$ grid cells used in selected analyses.....	16
Figure 4. The locations of 3,098 stations used for the extreme precipitation trend analysis.....	18
Figure 5. Schematic of the DL-FRONT 2D CNN architecture. The five-category input data grid on the left contains the five input surface meteorological 2D fields (temperature, humidity, pressure, u-component of wind, v-component of wind). The five-category output data grid on the right contains five 2D likelihood estimates for the five front categories (cold, warm, stationary, occluded, and none).	22
Figure 6. Side-by-side comparison of CSB (a) and DL-FRONT (b) front boundaries for 2009-08-01 12:00:00. The CSB fronts were drawn three grid cells wide. The intensities of the colors for the different front types in the DL-FRONT image represent the likelihood value (from 0.0 to 1.0) associated with each grid cell.....	24
Figure 7. Time series of annual total precipitation for four locations, one for each region analyzed in the determination of meteorological causes of heavy precipitation events. The Eielson AFB case required the creation of a composite data series using nearby observations (light green) due to missing data at the end of the data series.....	33
Figure 8. Sample image from animation loops of the various NCEP/NCAR reanalysis fields used to identify the meteorological causes of each heavy precipitation event.....	34
Figure 9. Precipitation climatology statistics for the nine NCEI climate regions and the United States as a whole. P is the total average precipitation without regard to season (label A for annual) and for the warm (W) and cold (C) seasons, $T(P)_{mm}$ is the linear trend (1949–2016; mm per decade), and $T(P)\%$ is the trend in percent per decade of the total [$T(P)_{mm}/P$] $\times 100\%$. Statistically significant trends (two-tailed test) are noted by *.	36
Figure 10. Trends (percent per decade) in the frequency of occurrences for each region during the (a) 1949–2016 and (b) 1979–2016 periods for the 35 ARI–duration combinations. Decreasing trends are displayed in shades of brown, and increasing trends are displayed in shades of green. Statistically significant trends are shown in red-colored numbers (0.05 significance level for a two-tailed test).	37
Figure 11. Values of $\delta_{ARI,d,annual}$, with red denoting statistical significance of T(EP) at the 0.05 level. The rotated numbers to the right of each table are annual values of T(P) (mm/decade). The W region is blank since $T(P)_{annual}$ is near zero.	38
Figure 12. Least-squares trends in water vapor (% per decade) from the (left column) NCEP/NCAR reanalysis and (right column) MERRA2 reanalysis for (a and b) annual, (c and d) warm season, and (e and f) cold season.	40

Figure 13. The 1951–2014 trend of the number of 5-day total precipitation events exceeding the station-specific threshold for an average 10-yr recurrence interval. White dots indicate that the trend is significant at the $0.05 < p \leq 0.10$ (small dots) or $p \leq 0.05$ (large dots) level.	41
Figure 14. Maps of seasonal front-crossing rate climatologies (2003–2015) for the CSB and DL-FRONT datasets.	42
Figure 15. Scatterplots comparing the DL-FRONT and CSB seasonal front-crossing rate climatologies over the CONUS-centered ROI.	44
Figure 16. Comparison of the front/no-front CSB and DL-FRONT MERRA2 monthly front-crossing rate climatologies spatially averaged across the entire CONUS ROI.	45
Figure 17. Monthly time series of the domain-averaged frontal-crossing rate anomalies for CSB and for MERRA-2 analyzed by DL-FRONT.	46
Figure 18. Annual fractional probability distribution of all days (black line) and days with an extreme (1-yr, 1-day recurrence) precipitation event (green line) vs. precipitable water (the 3-hr maximum during the day of the event) in 2 mm increments by NCEI climate region (from Kunkel et al. 2020a).	47
Figure 19. Correlation coefficients of AMS EP event magnitude vs PW for (a) NCEP/NCAR reanalysis for 1949–2017, (b) NCEP/NCAR reanalysis for 1980–2017, and (c) MERRA-2 reanalysis for 1980–2017.	49
Figure 20. Boxplot distributions for the 1-yr, 1-day partial duration series of (a) precipitation event amount vs the same-day 3-hour maximum PW sorted into 10mm interval bins and (b) as in panel (a) but for the amplification factor A (EP/PW). Boxplot parameters include mean (green diamonds), median (orange horizontal lines), 25th and 75th percentiles (box limits), and 5th and 95th percentiles (whiskers). Statistical significance (0.05 level) of the difference between A across adjacent intervals of PW is denoted where “–” and “+” denote a significant decrease and increase, respectively (the value of A in the higher PW bin minus lower PW bin). The observation count in panel (b) used in the statistical tests is depicted above the top whisker, and the 95th percentile value for bin 0–10 is 10.75.	50
Figure 21. Observed and fitted relationship between PW and α . These are the values of α that are used in the CAUSES equation (3).	52
Figure 22. Correlation coefficients for the annual maximum series of (a) EP event magnitude with $-\omega$, (b) PW with $-\omega$, and (c) A with $-\omega$. PW and $-\omega$ are the simultaneous day’s 3-hr maximum precipitable water and 3-hr maximum vertical velocity, respectively. Triangles indicate statistically significant (0.05 level) correlations.	54
Figure 23. Percentage changes in precipitable water by month for daily extreme precipitation events with a 1-in-5-year recurrence for four quadrants of the United States.	55
Figure 24. Average amplification factor (A) for each station for precipitation events exceeding the 1-yr, 1-day threshold for (a) warm season, (b) cold season, and (c) cold-to-warm season ratio of A	56
Figure 25. Percentage of the five largest daily precipitation events that are caused by fronts. The period of analysis is 1908–2013.	57

Figure 26. Percentages of meteorological causes for 1-day duration extreme precipitation events for each $10^{\circ}\times 10^{\circ}$ grid box for 1980–2017.	58
Figure 27. Seasonal correlations between the occurrence of extreme events and the incidence of frontal passages for a) winter (DJF), b) spring (MAM), c) summer (JJA), and d) fall (SON). Data tables containing correlation coefficients for each return interval/duration pair are shown for each $10^{\circ}\times 10^{\circ}$ degree grid box. Values are multiplied by 100 (e.g., a correlation coefficient of 0.23 is represented as 23). Rows indicate values for a return period of (from bottom to top) 1, 2, 5, 10, and 20 years. Columns indicate values for durations of (from left to right) 1, 2, 3, 5, 10, 20, and 30 days. Brown shades depict negative correlations, and teal shades depict positive correlations. Correlation coefficients displayed in red indicate a statistically significant correlation ($p<0.05$). Values are masked out if the number of events in that grid cell and season are less than 10% of the total number of events for all seasons. If all return period/duration pairs are masked out, the entire data table is blank.....	61
Figure 28. Seasonal correlations between the occurrence of extreme events and the incidence of extratropical cyclones (ETCs) for a) winter (DJF), b) spring (MAM), c) summer (JJA), and d) fall (SON). Data tables containing correlation coefficients for each return interval/duration pair are shown for each $10^{\circ}\times 10^{\circ}$ degree grid box. Values are multiplied by 100 (e.g., a correlation coefficient of 0.23 is represented as 23). Rows indicate values for a return period of (from bottom to top) 1, 2, 5, 10, and 20 years. Columns indicate values for durations of (from left to right) 1, 2, 3, 5, 10, 20, and 30 days. Brown shades depict negative correlations, and teal shades depict positive correlations. Correlation coefficients displayed in red indicate a statistically significant correlation ($p\leq 0.05$). Values are masked out if the number of events in that grid cell and season are less than 10% of the total number of events for all seasons...	64
Figure 29. Percentage of ETCs over CONUS by minimum sea level pressure and average speed of movement during 1980–2016 (from NCEP/NCAR reanalysis).....	65
Figure 30. Percentage of ETCs that caused a daily 1-yr recurrence event somewhere over CONUS by minimum sea level pressure and average speed of movement during 1980–2016 (from NCEP/NCAR reanalysis).	66
Figure 31. Frequency distribution functions for moisture divergence at the vertical pressure level of 700 hPa for the months of June, July, August, and September for the states of Arizona and New Mexico for the period 1979–2013. The red line is the climatological distribution, including all days. The blue line is the distribution for the days with the highest state-wide average precipitation. This includes the top 51 events for Arizona and the top 51 events for New Mexico.	67
Figure 32. Projected change in the 5-yr and 100-yr return period amounts for 24-hr and 30-day precipitation for 2070–2099 relative to 1976–2005 under the RCP8.5 emissions scenarios using the LOCA downscaled data.	68
Figure 33. RCP8.5 5-day extreme precipitation totals for the 100-year return interval for the early 21st century, mid-21st century, and late 21st century.....	70
Figure 34. Future changes (%) in the frequency of moisture flux convergence. These are averages for 13 CMIP5 models.	71

Figure 35. Projected change (%) in maximum daily precipitable water (PW_{max}) by late 21st century relative to late 20th century under the high (RCP8.5) emissions scenario. This is an average of 13 CMIP5 models.	72
Figure 36. Change (%) in the frequency of fronts during 2070–2099 (relative to 1985–2015) under the high emissions scenario (RCP8.5) from an ensemble of 5 global climate models. Decreases are projected across the southern and western United States. The changes are small for the northern United States.	74
Figure 37. Future change (%) in the number of ETCs for 2070–2099 under the high emissions scenario (RCP8.5). These are averages of 23 CMIP5 models.	75
Figure 38. Meteorological causes of heavy precipitation events, by season, for four regions: Central Alaska, Southern Alaska, Hawai‘i, and Guam. Five different causes were included: tropical cyclone (blue), extratropical cyclone (orange), fronts (gray), subtropical low (yellow), and air mass convection (green).	76
Figure 39. Average PW by region for events of an approximate 25-yr return level.	78
Figure 40. Precipitation amounts for selected return levels for 1-day duration events for grid box #10. These are averages for LOCA grid points within that box.	79
Figure 41. Display of website showing installation selection dropdown menu.	83
Figure 42. Display of website showing adjusted IDF values for 2055 under the RCP8.5 emissions scenario.	84

List of Tables

Table 1. Reanalysis datasets used in this project. The period of record, spatial resolution, and time resolution are included.	12
Table 2. Global climate models used in the analyses of extratropical cyclone tracks, precipitable water extremes, monsoon moistures, and identification of fronts.	14
Table 3. Counts of CSB and DL-FRONT grid cells over the training and validation time ranges and fraction of grid cells occupied by different front types.	25
Table 4. Change in event-averaged maximum PW [(1992–2013) minus (1971–1991)] for four U.S. quadrants (center divisions 100°W and 38°N) and three recurrence levels for daily precipitation.	48
Table 5. Regional average PW values (expressed as standardized anomalies) for three tiers of years: the top third, middle third, and bottom third of the magnitude of daily maximum precipitation. The regions follow the NCEI definitions (see Figure 2), except that Central is an aggregate of the Northern Rockies and Plains, Upper Midwest, and Ohio Valley and South/Southeast is an aggregate of the South and Southeast.	48
Table 6. Percent of all stations with statistically significant (0.05 two-tailed t-test) correlations between the specified variables.	53
Table 7. Moisture flux convergence terms ($10^{-5} \text{g Kg}^{-1} \text{s}^{-1}$) for 50 extreme summer precipitation events in Arizona and New Mexico.	66
Table 8. The CAM5 simulation assigned to each future period. The scaling factor is also shown.	73
Table 9. Future change (%) in the winter 30-yr maximum daily PW for Honolulu, Hawai‘i for seven 30-year overlapping blocks to the end of the 21st century using climate models forced with the RCP8.5 emissions scenario. Reference period is 1976–2005.	77

Acronyms and Abbreviations

AFB	Air Force Base
AMS	annual maximum series
ARI	average recurrence interval
AT	advection term
C	Celsius
C	Central (NCEI climate region)
CC	Clausius–Clapeyron
CAM5	Community Atmosphere Model Version 5.0
CAUSES	ClimAtological effects Under Synoptic Extreme States
CLIVAR HWG	Climate Variability and Predictability Program Hurricane Working Group
CMIP5	Climate Model Intercomparison Project Phase 5
CNN	convolutional neural network
CONUS	contiguous United States
CRS	coordinate reference system
CSB	Coded Surface Bulletin
CT	convergence term
DJF	December–January–February (winter)
DL	deep learning
DL-FRONT	deep learning neural network fronts detection algorithm
DLNN	deep learning neural network
DoD	Department of Defense
DOE	Department of Energy
ENC	East North Central (NCEI climate region)
EP	extreme precipitation
EPD	statistically downscaled extreme precipitation design value
EPC	extreme precipitation design value estimated from CAUSES equation
ETC	extratropical cyclone
FRT	front
GEV	generalized extreme value statistical distribution and methodology
GCM	global climate model
GHCND	Global Historical Climatology Network-Daily
GHG	greenhouse gas
GIS	Geographic Information System
gr	grain
HAPPI	Half a degree Additional warming, Prognosis and Projected Impacts
hPa	hectopascal
HUC	hydrologic unit code
IBTrACS	International Best Track Archive for Climate Stewardship
IDF	Intensity-Duration-Frequency
IGRA	Integrated Global Radiosonde Archive
JJA	June–July–August (summer)

kg	kilogram
km	kilometer
LOCA	Localized Constructed Analogs
MAM	March–April–May (spring)
m	meter
mb	millibar
mm	millimeter
MC	Extreme precipitation events caused by North American monsoon
MERRA-2	Modern-Era Retrospective analysis for Research and Applications Version 2
MFC	moisture flux convergence
NARR	North American Regional Reanalysis
NASH	North Atlantic Subtropical High
NCAR	National Center for Atmospheric Research
NCEI	National Centers for Environmental Information
NCEP	National Centers for Environmental Prediction
NE	Northeast (NCEI climate region)
NN	neural network
NOAA	National Oceanic and Atmospheric Administration
NW	Northwest (NCEI climate region)
NWS	National Weather Service
OCONUS	outside the contiguous United States
PC	precipitation causes method of estimating design values
PD	precipitation downscaled method of estimating design values
PDF	probability density function
PDS	partial duration series
POT	peaks over threshold
PW	precipitable water (total column water vapor)
QC	quality control
RCD	Regional Climate Division
RCP	Representative Concentration Pathway
REA	reliability ensemble averaging method
ROI	region of interest
S	South (NCEI climate region)
s	second
SE	Southeast (NCEI climate region)
SF	scaling factor
SLP	sea level pressure
SON	September–October–November (fall)
SW	Southwest (NCEI climate region)
TC	tropical cyclone
2D	two dimensional
USGS	United States Geological Survey
UTC	Coordinated Universal Time
VV	vertical velocity
W	West (NCEI climate region)

WNC	West North Central (NCEI climate region)
WPC	Weather Prediction Center
WS	weather system

Keywords

climate change
extreme precipitation
global warming
Intensity-Duration-Frequency
precipitation design values

Acknowledgements

The project progress and report contents are the results of the combined contributions of a team of scientists. David Easterling serves as the co-Principal Investigator. Thomas Karl served as a co-Principal Investigator for the early phases of the project and as a senior consultant for latter phases of the project. Team scientists include James Biard, Sarah Champion, Ronnie Leeper, Olivier Prat, Steven Stegall, Laura Stevens, Scott Stevens, Michael Squires, Liqiang Sun, and Xungang Yin. Editorial and graphical support was provided by Jessica Griffin, Thomas Maycock, and Andrea McCarrick.

This report can be cited as:

Kunkel, K.E., D.R. Easterling, T.R. Karl, J.C. Biard, S.M. Champion, B.E. Gleason, K.M. Johnson, A. Li, S. Stegall, L.E. Stevens, S.E. Stevens, M. Squires, L. Sun, and X. Yin, 2020: Incorporation of the Effects of Future Anthropogenically Forced Climate Change in Intensity-Duration-Frequency Design Values: Final Report. North Carolina Institute for Climate Studies, North Carolina State University, 104 pp.

Abstract

Objectives

Numerous scientific assessments have shown that human-induced climate changes are occurring, and more changes are expected as atmospheric composition is altered. This work focuses on how these changes affect extreme precipitation rates. In particular, design values are sought for extreme precipitation rates ranging from sub-daily to multi-day events. These values are typically quantified as extreme precipitation Intensity-Duration-Frequency values and, when plotted, are used by engineers and others for planning, design, and operations as Intensity-Duration-Frequency curves. The most comprehensive set of existing Intensity-Duration-Frequency curves developed over the past two decades is based on the assumption of a stationary climate. A key ultimate objective of this work is to transform Intensity-Frequency-Duration values into a new set that accounts for a non-stationary climate with varying degrees of climate change.

A prerequisite to developing non-stationary Intensity-Duration-Frequency values is to complete a comprehensive trend assessment across broad geographies. This includes both a representative set of Intensity-Duration-Frequency values and the weather and climate conditions known to affect these values across the U.S. and worldwide. Weather events of interest include those systems that generate upward vertical velocity over geographies with ample water vapor. Since it has been previously shown that particular weather types are needed to trigger extreme precipitation rates, an automated and objective method is needed to identify those weather types, not only in past data but in the enormous quantity of data generated from various global climate model (GCM) simulations, including their ensemble members of future climate.

Although GCMs are the backbone of understanding past and future climate, they are known to have deficiencies in simulating extreme precipitation rates of interest here. A number of methods have been developed to help overcome many of these deficiencies. Key objectives of this work include building on these existing methods to enable robust uncertainty estimates of future Intensity-Duration-Frequency values and, most importantly, provide an understanding of why changes in the Intensity-Duration-Frequency values are expected for specific locations and future times.

Technical Approach

Two complementary, but different methods were used to provide best estimates for future Intensity-Duration-Frequency values. The differing methods provide a basis for assessing uncertainty of future changes. The sources of uncertainty include 1) differing rates of human-caused changes to atmospheric composition, 2) the sensitivity of the climate to changes in atmospheric composition, 3) parameter estimation uncertainty of model coefficients, 4) structural uncertainty related to the approach used, and 5) statistical sampling uncertainty. The first approach used to estimate future changes—the precipitation downscaled (PD) method—uses a statistical method known as generalized extreme value (GEV) applied to a downscaled precipitation dataset, where changes in extreme precipitation rates, both historically and from global climate models, are calculated and used to project changes in Intensity-Duration-Frequency values by modifying existing Intensity-Duration-Frequency values based on a stationary climate. The second method, called the precipitation causes (PC) approach, makes use

of changes in well-simulated meteorological factors shown to contribute to extreme precipitation rates. These factors include column-integrated water vapor (i.e., precipitable water [PW]) and the weather systems causing upward vertical velocity responsible for condensing the water vapor into precipitation. Changes in PW, weather fronts, and extratropical cyclones (ETCs) are calculated from GCM simulations of past and future climate, and they are used to transform Intensity-Duration-Frequency values from stationary to non-stationary estimates.

Machine learning is used to develop an objective and automated algorithm for identifying fronts both in GCM output and model-assimilated observed data. This includes warm, cold, stationary, and occluded fronts associated with extreme precipitation events. The frontal identification is validated through comparison with human expert weather map analyses regularly produced by the National Oceanic and Atmospheric Administration (NOAA). Additionally, other objective methods were used to identify ETCs, both in observed data as well as past and future simulated climates. Changes in PW are also examined both historically and within GCM simulations of future climate and in relation to changes of extreme precipitation and upward vertical velocity.

Results

Observations show that over the past several decades the interval between extreme precipitation events is decreasing as they become more frequent across a wide range of durations. This is not evident in all areas, but it is the predominant trend and it is strongly linked to increases in PW. Global climate models project widespread increases in PW as the climate warms with various scenarios of human-induced changes of atmospheric composition. As a result, as time evolves, the projected Intensity-Duration-Frequency values generally lead to greater frequency of, and shorter intervals between, extreme precipitation events for a wide range of thresholds and duration times. Additionally, the rarer events tend to increase more than less-rare events (e.g., 50-year return period versus 1-year return period), regardless of duration. These projected changes are well beyond standard uncertainty intervals. The projected changes in other factors, such as fronts and extratropical storms, are not ubiquitous, and the magnitude of extreme precipitation is shown to be less sensitive to these changes compared to PW. This is because even when weather systems change in frequency, they still occur often enough to trigger copious precipitation when PW is high. The projected weather system changes do, however, combined with varying degrees of increases in water vapor, add to the spatial and temporal variability of projected Intensity-Duration-Frequency values.

Benefits

Planners, designers, and operation managers can now get access to a set of extreme precipitation Intensity-Duration-Frequency values for thousands of locations to help assess future risks of extreme precipitation events. The Intensity-Duration-Frequency values incorporate varying degrees of climate change associated with human alterations of atmospheric composition. Additionally, it is now possible to unravel specific causes associated with projected changes to better understand the risks of extreme precipitation events.

Objective

1. SERDP Relevance

The FY 2015 Statement of Need in the Program Area, “Adapting to Changes in the Hydrologic Cycle Under Non-stationary Climate Conditions,” indicates a need to “improve our fundamental and applied understanding of “the non-uniform spatial and temporal distribution of potential climate-induced changes in the intensity and variability of heavy precipitation and run-off events” and of adaptation of these changes to Department of Defense (DoD) needs in particular and the civil engineering community in general. Prior to this project, the most comprehensive and readily available method to project the intensity, duration, and frequency of heavy precipitation events was to use the Intensity-Duration-Frequency (IDF) curves developed by the National Oceanic and Atmospheric Administration (NOAA) and made available through the NOAA Atlas 14 and its numerous regional updates. The problem with using NOAA Atlas 14 IDF curves to estimate future extreme precipitation (EP) return intervals is that there is no inclusion of climate change in future estimates. This is a major dilemma, as numerous scientific assessments have clearly shown that the climate is changing, and this is very likely to continue in the foreseeable future. The rate and magnitude of climate change, however, is strongly dependent on the rate of changes in, and the resulting concentrations of, human-induced atmospheric greenhouse gases (GHGs) and other atmospheric constituents. This is an important uncertainty that is addressed in our approach.

Our work directly addresses the requirements of the solicitation, building upon extensive previous work related to heavy precipitation. This includes our own work where we have examined historical trends and potential future changes in heavy precipitation attributed to climate change. We have developed regional climate change adjustment factors that incorporate the effects of climate change that can be applied to existing IDF curves from NOAA Atlas 14. We provide results outside the NOAA Atlas 14 geographic domain for selected locations of specific interest to DoD. The adjustment factors include ranges that reflect uncertainties about the sensitivity of the climate system to changes in various scenarios of human-induced atmospheric composition and related radiative forcing. Our approach also includes both structural and statistical uncertainties related to our methodology in addition to uncertainty related to future changes in climate. This framework will provide information that can be used to assess the overall risks of various decision design alternatives.

2. Technical Objective

The overriding objective of this project was to develop a framework for incorporating future climate change into the IDF values of EP used by civil engineers. Our work leveraged the large amount of previous work on EP we had completed in addition to the delivery of IDF values done by the developers of NOAA Atlas 14. The underlying basis for making changes to IDF values is the robust, physically based projection of global warming with increasing GHG concentrations. Global warming, in turn, will increase atmospheric water vapor concentrations with an equally high level of confidence, producing the potential for more intense precipitation. Actual changes in IDF values will result from changes in atmospheric water **capacity**, i.e., vertically integrated water vapor concentrations, and **opportunity**, i.e., the number and intensity of heavy precipitation-producing storm systems. We evaluated these two components at frequencies and durations relevant to civil engineering and provide adjusted IDF values, along

with uncertainty estimates, that are based on a fundamental understanding of future changes in the climate system, an understanding that was more fully developed in this project.

We have developed a framework for incorporating the potential impact of future climate change into the IDF values of EP. IDF values are used in design regulations and guidance by the DoD as well as local, state, and other federal agencies. Temporal changes are especially important because non-stationary climate processes will impose changes in the IDF values that will vary over the lifetime of the infrastructure or other systems of interest.

The basis for projected changes is the suite of future projections from global climate model (GCM) experiments that simulate the response of the climate system to different scenarios of future changes in atmospheric composition. These projections were analyzed with respect to EP using two different methods. In the first method, called precipitation downscaled (PD), EP estimates were derived from GCM downscaled precipitation estimates that simulate future conditions. The second method, called precipitation causes (PC), made use of projected GCM-derived changes of atmospheric water vapor (without which precipitation does not occur) and specific weather systems that trigger EP events. In the PC approach, actual changes in IDF values are derived from both changes in atmospheric water vapor capacity and triggering mechanisms (the number of precipitation-producing atmospheric circulation systems, such as fronts and storm systems). This method enables an understanding of the key drivers of EP events and their changes in intensity, duration, and frequency. By contrast, with the PD method, it is uncertain what the primary meteorological causes are for changes in the IDF curves because this information is statistically projected onto the NOAA Atlas 14 IDF curves.

The two methods are applied to a wide range of IDF values used by civil engineers. The range of IDF values spans all but the lowest durations (less than 6 hours) of the IDF values used in NOAA Atlas 14, but for a changing climate.

The research was organized around the following scientific hypotheses:

Hypothesis 1: *Historically observed and anthropogenically forced future changes in IDF values used in the engineering community arise primarily from two principal meteorological sources: 1) changes in atmospheric water vapor concentration (potential) and 2) changes in the frequency and intensity of the weather systems that cause heavy precipitation (triggers).*

Hypothesis 2¹: *As the time horizon increases, IDF values will increase primarily because GCMs project increasing temperature and related water vapor altered by concomitant changes in the frequency and intensity of fronts and storm tracks and other changes in circulation.*

Hypothesis 3: *Regional variations in the changes of IDF values arise primarily from regional differences in water vapor, weather/climate systems, and regional aspects of terrain and ocean influence.*

¹ Hypotheses 2 and 3 are slightly revised from the original proposal to better focus the results of the analyses on IDF curves.

Background

The primary environmental issue is how the intensity, duration, and frequency of EP events will be affected by human-induced climate change. Ongoing and future changes in climate are now unequivocal (IPCC 2013). Given that EP has always been an important consideration in the design and construction, maintenance, and operation of many of DoD's assets, incorporating climate change information into IDF curves is the challenge of this research.

Historically, engineering approaches have relied on sets of IDF curves to assess likely return periods for various amounts of EP over specified durations. An example of a set of IDF curves that was based on the assumption of a stationary climate is shown in Figure 1. These IDF curves represent the best estimate for EP amounts if the climate was stationary. As the time horizon of interest increases, relying on IDF curves that assume no climate change increasingly jeopardizes effective planning and operations decisions. Increasingly, scientists have recognized this problem, and there is now a large body of work that addresses the climate change issue related to the IDF curves. Unfortunately, it still does not provide a comprehensive set of IDF curves with climate change information that can be used for operations and planning. It is useful to categorize the various methods that have been devised for the development of EP IDF curves, despite the fact that they have not been comprehensively applied to a broad range of IDF curves or geographies impacted by climate change.

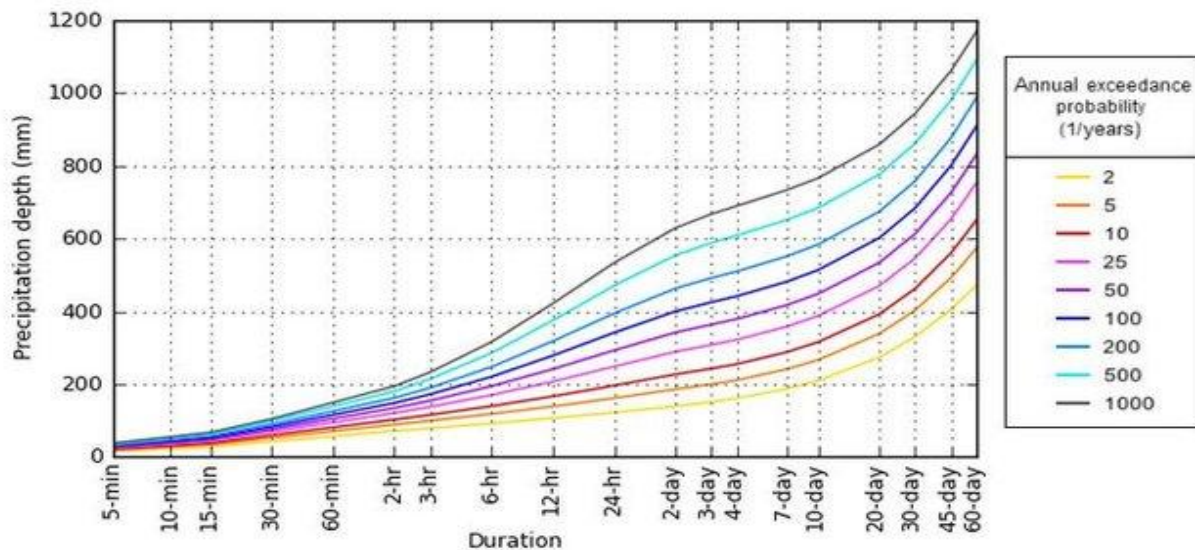


Figure 1. *IDF curves for a rain gauge in Lafayette, Louisiana (Latitude: 30.2050, Longitude: -91.9875) (Source: NOAA NWS 2020).*

It should be noted that the use of climate global climate model (GCM) simulations is playing an increasing role for estimating future values of IDF extreme precipitation. Recent research and applications for estimating EP with IDF curves can be categorized into three approaches. First, there are analyses that rely exclusively on historical observations (e.g., Ganguli and Coulibaly 2017, Cheng and Aghakouchack 2014, and NOAA Atlas 14 [Bonnin et. al. 2005]) with numerous regional updates). Second, other analyses use historical observations to

calibrate or downscale GCM projections of precipitation with the use of non-stationary statistics (e.g., DeGaetano and Castellano 2017, Srivastav et al. 2014, and Lima et al. 2016). Finally, there are analyses that also use historical observations to calibrate or downscale the output from a subset of the “best” GCMs and also use non-stationary statistics (e.g., Simonovic et al. 2016, Chandra et al. 2015, and Agilan and Umamahesh 2016). This brief review will highlight the ability of each approach in terms of providing effective future IDF values. All these approaches have provided useful tools for assessing the likelihood of various types of EP probabilities, but in general they have not been extensively applied to broad geographies and a full set of IDF curves.

Exclusive Use of Recent Historical Data

There is evidence to suggest that the use of recent historical observations and non-stationary statistics can provide useful estimates of IDF out to about a decade or so (Ganguli and Coulibaly 2017). The advantage of using this approach is tied to at least three issues. First, at short time horizons of a decade or less, natural climate variability can readily swamp longer-term forced changes (Easterling and Wehner 2009). Second, by focusing only on historical observations, high-time-resolution sub-daily (minutes, hours) extreme event data, which sometimes are of key importance to users, are often directly available without resorting to any loss of information through downscaling techniques. Finally, the differences between IDF statistics using stationary or non-stationary statistics for relatively short future time horizons are competing with errors related to estimating the statistical model parameters derived from the precipitation time series and the measurement errors of precipitation at high intensity among other kinds of errors. The former has been recognized, but the latter has rarely been included in the error estimates of the precipitation IDF. The error characteristics of the measurement of precipitation data vary with precipitation rate, instrument type, precipitation type, and ambient weather conditions. In a field comparison of various precipitation gauges, Lanza et al. (2007) show that depending on the gauge used, errors and systematic biases in the range of 5–15% are common.

There is some evidence to suggest that the use of non-stationary versus stationary statistics has the largest impact at the sub-daily hourly durations versus the longer multi-day durations (Cheng and Aghakouchack 2014), but this needs more evaluation prior to generalizing. Additionally, caution is required for users of stationary IDFs for long time horizons (e.g., NOAA Atlas 14), because differences between stationary and non-stationary methods can grow substantially as shown by Cheng and Aghakouchack (2014) and others as described in the next two subsections.

Historical Observations Calibrated to GCMs for a Simulated Future

The use of GCMs greatly enhances consideration of various types of non-stationarity that can manifest as future climate. Although these methods have added considerable value in our ability to define future IDF curves, the use of GCMs for future IDF curves does come with a few caveats. Bias corrections as well as spatial and temporal downscaling are all required in the use of the climate model output. These are related to the assumption that the relationships developed to remove biases and downscale the data are time invariant, and this is questionable. An extreme case in point includes regions where surface boundary conditions change dramatically, such as the presence of lake- or sea-ice to no lake- or sea-ice. This change influences regional vertical profiles of temperature and humidity, which may not be well reflected in the historical record. Lanzante et al. (2018) demonstrate that discrepancies can arise in the derived relationships of model–historical observations, which vary geographically, seasonally, and across weather

conditions and the types of downscaling methods used. They conclude that “whether a particular pitfall may be a serious concern depends on the details of a study’s climate data needs and sensitivities—a factor that can preclude simple one-size-fits-all guidance.” Other concerns include evidence suggesting that the relationships that are required between daily total precipitation (generally available from the models) and hourly and minute precipitation intensities (often requested by users) appear to depend on the rate of change in temperature or atmospheric water vapor (Westra et al. 2014).

The use of GCMs in the development of IDF curves has now been applied across a variety of regions. In one of the larger applications, DeGaetano and Castellano (2017) develop IDF curves using well over a hundred stations across the state of New York, dozens of climate models, and a variety of downscaling methods. Their results showed that biases were reduced most by pooling together the output from all the GCMs, but it was not readily apparent what downscaling method delivered the best results, although they did not include a weather generator downscaling method whereas some analyses have done so (Chandra et al. 2015). Other analyses (e.g., Srivastav et al. 2014, following Li et al. 2010) have focused on downscaling methods that ensure preservation of any changes in the distribution of annual maximum precipitation produced by the GCMs from current to future climate. Nonetheless, it remains unclear whether or not there is a universally best downscaling method.

In terms of identifying the best extreme value distribution, often necessary when using the output of GCMs to develop IDF curves, there is also ambiguity, but Lima et al. (2016) argue that the Bayesian beta distribution provides a unique advantage of being able to identify the error bounds associated with the parameters of the statistical extreme value distribution. The Bayes formulation is more complex than classical generalized extreme value (GEV) methods, so the merits would have to be considered, along with the ability to address other sources of errors (e.g., spatial downscaling, temporal downscaling, measurement, and future sources of atmospheric composition). Some (e.g., Chandra et al. 2015) have argued that statistical model parameter uncertainty is more important than GCM model uncertainty, although this was based on an analysis of a single station, highlighting the quandary of assessing uncertainties.

Historical Observations Calibrated to the Best GCMs

Given the relatively large variability of future values of maximum precipitation arising from many different GCMs, a number of studies have sought to identify the “best” GCM in terms of its ability to simulate climate. One of the most popular approaches is the method of reliability ensemble averaging (REA) proposed by Giorgi and Mearns (2003), where the similarity of the GCM-simulated climate to the observed climate for selected variables is weighted along with the similarity of the future climate to those simulated by other models. The variables to be assessed are left to the analyst. For IDF applications, daily precipitation amounts have often been used (Agilan and Umamahesh 2016, Simonovic et al. 2016). Chandra et al. (2015) provide an example for one station showing that the use of the REA method also favorably influences the uncertainty related to the selection of the statistical extreme value distribution and its parameters.

Preferred Approach in This Work

Our work here is contained within the approach described as “historical observations calibrated to GCMs for a simulated future,” subdivided into a statistically based downscaled GCM model projection approach and another focused on the capability of GCMs to project precipitable water (PW) and synoptic and mesoscale weather disturbances. Kunkel et al. (2012)

provide an extensive analysis of the causes of EP events in the U.S. They find that different types of fronts and various storms are key triggers related to EP events. In this caused-based approach, future estimates of EP make use of the relationships between EP and key synoptic meteorological and climate systems for a given amount of column-integrated water vapor (or PW). In addition to providing projections needed to produce EP IDF curves, our approach also provides insights into the causes of future EP events. Developing the relationships between EP events and key synoptic meteorological/climatological systems known to directly affect EP rates with respect to PW values is a crucial component of our work.

Material and Methods

General

Present-day extreme precipitation (EP) IDF design values are assessed and revised using two complementary methods that enable us to best assess uncertainty of future projected changes in EP. This two-phased effort includes 1) a generalized extreme value (GEV) analysis (Coles 2001) of projected changes of precipitation in the downscaled projections of global climate models (GCMs) and 2) the use of known relationships between extreme rainfall events and the key synoptic meteorological/climatological systems known to directly affect extreme precipitation rates. This two-phased effort enables us to more effectively assess the degree of confidence in projected changes of EP.

In the first method, we make use of downscaled GCM precipitation estimates to estimate future values of EP denoted by EPD (D for downscaled). This is written as:

$$EPD_{d,f}^{fut}(x, y, t) = \frac{EP_{d,f}^{NA14}(x, y) \cdot GEV_{d,f}[AMS_{DGCM}(x, y, t)]}{GEV_{d,f}[AMS_{DGCM}(x, y, curr)]} \quad (1)$$

where:

$EP_{d,f}^{NA14}(x, y)$ = current precipitation design value for duration d and frequency f at location (x, y) . These values will be taken from NOAA Atlas 14,

$EPD_{d,f}^{fut}(x, y, t)$ = precipitation design value at future year t for duration d and frequency f at location (x, y) based on downscaled data,

$GEV_{d,f}$ = the precipitation design value for duration d and frequency f derived from a GEV analysis of GCM extreme rainfall/snowfall at location (x, y) ,

$AMS_{DGCM}(x, y, t)$ = annual maximum series of downscaled GCM extreme rainfall/snowfall at location (x, y) for a 30-yr period centered around year t

Because of the known limitations of GCM-simulated extreme rainfall events, including events from downscaled data and the lack of clarity related to the causes of those events from a statistically based downscaled approach, our second means of developing future estimates of EP make use of the relationships between EP and key synoptic meteorological and climate conditions known to directly cause EP. This includes atmospheric water vapor and the vertical motion associated with synoptic weather and climate systems (Kunkel et al. 2012, Kunkel et al. 2013, Kunkel et al. 2020a). Changes of the causes of extreme precipitation are assessed within GCM simulations to estimate future values of EP and will be denoted as EPC (C for causes). Formally, this set of relationships is defined by the equation of Climatological effects Under Synoptic Extreme States (the CAUSES equation), which is written as:

$$EPC_{d,f}^{fut}(x, y, t) = EP_{d,f}^{NA14}(x, y)[1 + \alpha\Delta PW(x, y, t)]\{1 + G[\sum_{s=1}^4 \beta(FRT(x, y, s)\Delta FRT(x, y, s, t) + \gamma ETC(x, y, s)\Delta ETC(x, y, s, t)) + \delta TC(x, y)\Delta TC(x, y, t) + \epsilon MC(x, y)\Delta MC(x, y, t)]\} \quad (2)$$

where weather system influences are quantified by:

$FRT(x,y,s)$ = the fraction of all events at point (x,y) that are caused by fronts in season s for the current climate,

$ETC(x,y,s)$ = the fraction of all events at point (x,y) that are caused by extratropical cyclones in season s for the current climate,

$TC(x,y)$ = the fraction of all events at point (x,y) that are caused by tropical cyclones in the tropical cyclone season for the current climate,

$MC(x,y)$ = the fraction of all events at point (x,y) that are caused by the North American Monsoon in the monsoon season for the current climate,

$\Delta FRT(x,y,s,t)$ = fractional change in frontal frequency in season s at point (x,y) at future year t ,

$\Delta ETC(x,y,s,t)$ = fractional change in frequency of extratropical cyclones in season s at point (x,y) at future year t ,

$\Delta TC(x,y,t)$ = fractional change in frequency of landfalling tropical cyclones at point (x,y) at future year t ,

$\Delta MC(x,y,t)$ = fractional change in frequency of North American Monsoon moisture surges at point (x,y) at future year t ,

$\Delta PW(x,y,t)$ = fractional change in precipitable water in future year t at point (x,y) ,

G = function which transforms the weather system frequency changes into quantitative changes in IDF values,

$\alpha, \beta, \gamma, \delta$, and ε = coefficients defined by the empirical relationships between the respective variable and extreme precipitation amounts in the observed data

Based on current GCM capability, ΔTC and ΔMC are set to zero. The rationale for $\Delta TC = 0$ is based on a comprehensive assessment of confidence related to changes in TC climatology as the climate warms (Knutson et al. 2020). In that assessment the highest confidence was associated with TC precipitation rates scaling with water vapor increases as the climate warms. This is already included in our CAUSES equation through PW. Lowest and mixed confidence was given to changes in the frequency of tropical cyclone frequency and thus ΔTC is set to zero. Until GCMs increase resolution and reduce parameterization to resolve eye wall characteristics and clouds, it would be risky to project any change in TC frequency at regional and local space scales. Regarding the MC, future changes remain uncertain. Depending on the model, model resolution, and bias corrections, projections range from an intensified circulation with more intense rainfall to reduced early-season circulation and less rainfall (Meyer and Jin 2017, Pascale et al. 2017). As a result, ΔMC is also set to zero. With these changes, the CAUSES equation (2) simplifies to:

$$EPC_{d,f}^{ut}(x,y,t) = EP_{d,f}^{NA14}(x,y)[1 + \alpha\Delta PW(x,y,t)] \{1 + G[\sum_{s=1}^4 \beta(FRT(x,y,s)\Delta FRT(x,y,s,t) + \gamma ETC(x,y,s)\Delta ETC(x,y,s,t))]\} \quad (3)$$

The development of the EPD and EPC values were subdivided into the following set of six tasks, with the first five tasks also addressing the three hypotheses:

Task 1: Perform a historical analysis of U.S. and global trends in precipitation in the range of frequencies and durations of relevance to civil engineers (e.g., NOAA Atlas 14 covers average recurrence intervals [ARIs] of 1 through 1,000 years and durations of 5 min through 60 days).

Task 2: Modify existing software and develop new software to automatically identify key weather systems that cause heavy precipitation in historical reanalyses and climate model simulations.

Task 3: Perform a thorough analysis of the meteorological causes of heavy precipitation increases over the last few decades, building on previous work.

Task 4: Perform extensive analyses of Climate Model Intercomparison Project Phase 5 (CMIP5) model simulations, identifying the occurrence of weather systems causing heavy precipitation for historical and future simulations.

Task 5: Determine the meteorological causes and trends of heavy precipitation events at global military installation sites identified by DoD.

Task 6: Develop applications, including adjustment factors for current IDF values, and incorporate them into the delivery mechanism for current IDF values to provide convenient and reliable access to appropriate values by the civil engineering community.

Datasets

Reanalysis

Several reanalysis datasets were used in this project, including the NCEP/NCAR Reanalysis 1 (Kalnay et al. 1996), NCEP/DOE Reanalysis 2 (Kanamitsu et al. 2002), MERRA-2 (Gelaro et al. 2017), and NARR (Mesinger et al. 2006). Table 1 provides the basic characteristics of these datasets, including the resolution and time period of available data. The NCEP/NCAR Reanalysis 1 has the longest period of record of these and was used for water vapor analyses to match the period for extreme precipitation trends analysis. The MERRA-2 has a much higher spatial resolution than NCEP/NCAR Reanalysis 1. It was used to investigate the robustness of results found with the NCEP/NCAR Reanalysis 1. It was also used for the development of the frontal detection algorithm, which required a higher resolution than the NCEP/NCAR Reanalysis 1, and for the subsequent development of a historical fronts dataset. The NARR was originally chosen for use in the development of the fronts detection algorithm, but we found that the MERRA-2 gave better results. Finally, the NCEP/DOE Reanalysis 2 was used in some of the monsoon moisture convergence analysis because it is an improved version of the NCEP/NCAR Reanalysis 1, and we considered its results for moisture transport to be more reliable.

Table 1. *Reanalysis datasets used in this project. The period of record, spatial resolution, and time resolution are included.*

Title	Abbreviation	Period of Record	Spatial Resolution	Time Resolution
National Centers for Environmental Prediction/National Center for Atmospheric Research	NCEP/NCAR Reanalysis 1	1948–present	2.5° latitude x 2.5° longitude	6-hourly
National Centers for Environmental Prediction/Department of Energy Reanalysis 2	NCEP/DOE Reanalysis 2	1979–present	2.5° latitude x 2.5° longitude	6-hourly
Modern-Era Retrospective analysis for Research and Applications, Version 2	MERRA-2	1980–present	0.5° latitude x 0.625° longitude	1-hour
National Centers for Environmental Prediction North American Regional Reanalysis	NARR	1979–present	32 km, Northern Lambert Conformal Conic grid	3-hourly

Precipitation

A network of observing stations taking daily observations (24 hr) of total precipitation was necessary to perform the analysis. These data came from the Global Historical Climatology Network-Daily (GHCND), which is made up of observing stations from the U.S. Cooperative Observer Program that was established in the late 1800s and managed by the National Weather Service. GHCND is subjected to rigorous quality control (QC) methods to flag spurious data to ensure robust results (Durre et al. 2008, Durre et al. 2010). Included in the QC are duplicate checks that flag successive observations that are identical. Duplicates were separately verified for authenticity and not used if found to be erroneous.

There were some specialized datasets that were also used. We obtained from the Air Force 14th Weather Squadron daily precipitation data for Fort Wainwright and Eielson Air Force Base in Alaska, both with long periods of record.

Meteorological Fronts

The NOAA National Centers for Environmental Prediction has a manually produced dataset of frontal boundaries known as the Coded Surface Bulletin (CSB; Zenodo 2019). Each CSB message contains lists of latitudes and longitudes that specify the locations of pressure centers, fronts, and troughs identified by NOAA meteorologists as part of the 3-hourly operational North American surface analysis they perform at the Weather Prediction Center (WPC). Each front or trough is represented by a polyline.

A dataset (1908–2009) was produced in a previous project (Kunkel et al. 2012), which identified 1-day extreme precipitation events exceeding a 5-yr recurrence interval associated with fronts. Identification was done manually. Since the publication of that study, the dataset has been extended to 2017 using the same methodology. We extracted from that dataset all frontal events for the period of 1980–2017—the overlap between that dataset and the MERRA-2 reanalysis data.

GCM Simulations

Projections of future climate conditions were developed from GCM simulations produced for the Climate Model Intercomparison Project (CMIP). CMIP includes a set of experiments with protocols that are followed by modeling groups. For most of the work in this project, simulations were used from CMIP5 (Taylor et al. 2012). For the frontal analysis, a few models from CMIP Phase 6 were used. The final climate model used was the CAM5 (Community Atmosphere Model Version 5.0) under the HAPPI (“Half a degree Additional warming, Prognosis and Projected Impacts”) protocol, which is motivated by the Paris Agreement of 2015. The HAPPI simulations investigate global climate changes for global warming targets of 1.5°C and 2.0°C. The CAM5 was used to produce such simulations by Michael Wehner of Lawrence Berkeley National Laboratory and provided to us by him. He also added a simulation for 3.0°C global warming.

A major challenge encountered in this project derived from differing data requirements for the various project tasks. The ETC analysis needed only daily surface pressure data. The precipitable water and monsoon moisture surge analyses required upper-level daily data. The fronts analysis required 3-hourly-resolution data. Data availability in the CMIP5 archive is highly variable across models. Most models had only a subset of desired data. For each individual task, we decided to use all available models to maximize the robustness of the outcomes. Table 2 shows the models used in each type of analysis. There were 23, 13, 13, and 5 models available for the extratropical cyclone, precipitable water, monsoon, and fronts analyses, respectively.

Table 2. Global climate models used in the analyses of extratropical cyclone tracks, precipitable water extremes, monsoon moistures, and identification of fronts.

GCM	Extratropical Cyclones	Precipitable Water	Monsoon	Fronts
bcc-csm1-1	x			
bcc-csm1-1-m	x			
BCC-CSM2-MR (CMIP6)				x
CAM5				x
CanESM2	x	x	x	
CCSM4		x	x	
CMCC-CM	x	x	x	
CNRM-CM5	x	x	x	
EC-Earth3 (CMIP6)				x
FGOALS-g2	x	x	x	
GFDL-CM3	x	x	x	
GFDL-ESM2G	x	x	x	
GFDL-ESM2M	x	x	x	
HadGEM2-CC	x			
HadGEM2-ES	x			
Inmcm4	x	x	x	
IPSL-CM5A-LR	x			
IPSL-CM5A-MR	x			
IPSL-CM5B-LR	x			
MIROC5	x	x	x	
MIROC-ESM	x	x	x	
MIROC-ESM-CHEM	x		x	
MPI-ESM-LR	x			
MPI-ESM-MR	x	x		
MPI-ESM1-2-HR (CMIP6)				x
MRI-CGCM3	x	x		
MRI-ESM1	x			
MRI-ESM2-0 (CMIP6)				x
NorESM1-M	x		x	

Regional Definitions

To ensure adequate sample sizes and robust relationships, our work included integrating across various regions. This included regions (Figure 2) that are linked on the basis of climatology and shared political boundaries (Karl and Koscielny 1982, Karl and Koss 1984) as well as large regional-scale grid cells (e.g., 10 by 10 degrees of latitude and longitude; Figure 3).

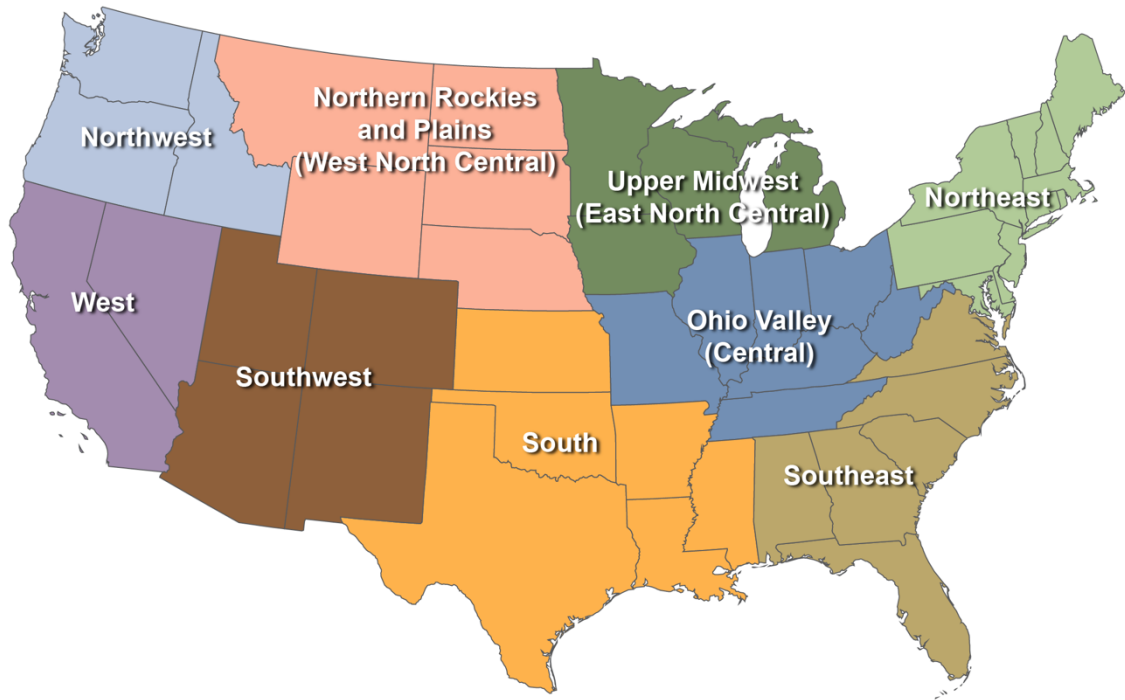


Figure 2. The National Centers for Environmental Information (NCEI) climate regions used in this study. Abbreviations for the regional titles are: Northwest — NW; West North Central — WNC; East North Central — ENC; Northeast — NE; West — W; Southwest — SW; South — S; Central — C; Southeast — SE.

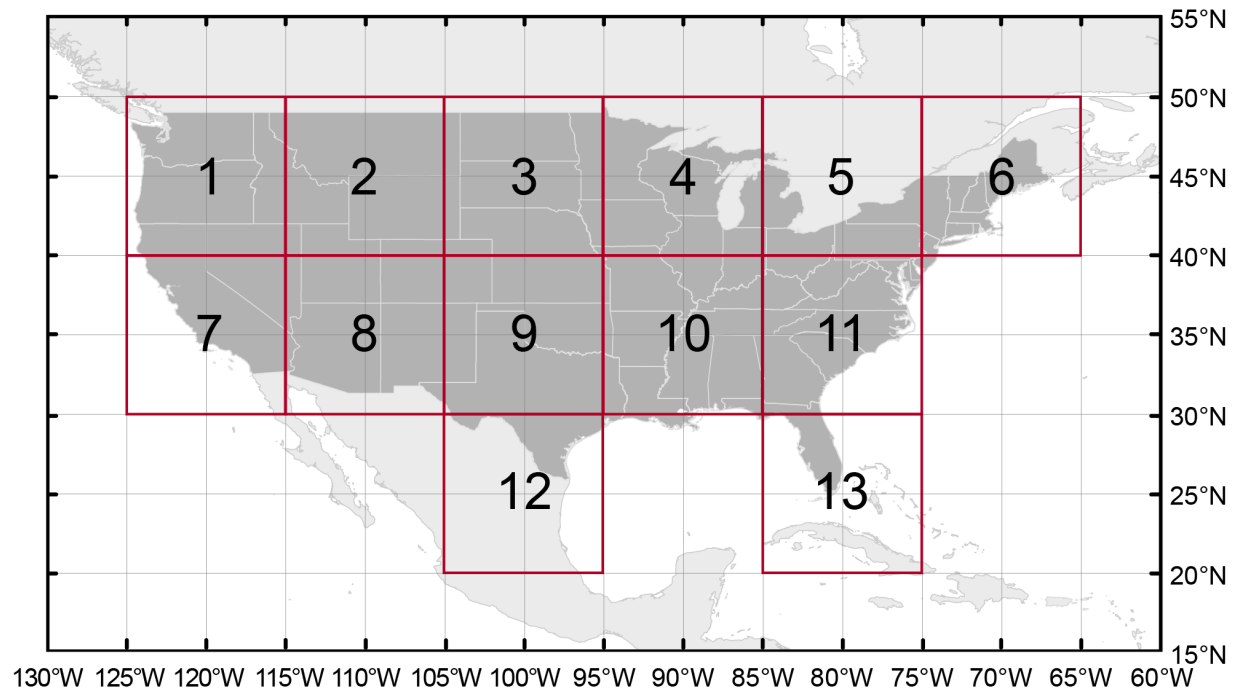


Figure 3. $10^{\circ} \times 10^{\circ}$ grid cells used in selected analyses.

In the following tasks, data analysis was accomplished primarily through the development and application of custom computer programs and scripts. Computer programs were written in FORTRAN, Python, or R. In some cases, where noted, the programs were derivative of software used in other projects and described in journal articles. In other cases, standard packages were used. For example, the least-squares regressions Python module “`scipy.stats.linregress`” (<https://docs.scipy.org/doc/scipy/reference/generated/scipy.stats.linregress.html>) was used for some of the trends analyses. The Generalized Extreme Value (GEV) analysis in Task 4 utilized the R package “`ismev`” (<https://cran.r-project.org/web/packages/ismev/index.html>)

Task 1: Perform a historical analysis of U.S. and global trends in precipitation in the range of frequencies and durations of relevance to civil engineers (e.g., NOAA NWS 2020 covers ARIs of 1 through 1,000 years and durations of 5 min through 60 days).

In order to understand how regional changes in precipitation extremes relevant to the civil engineering community have changed, a wide range of durations and return intervals was analyzed for the contiguous United States (CONUS). The period of analysis was 1949–2016, which corresponds to observed increases in extreme events documented in a number of other studies (e.g., Walsh et al. 2014). In addition to analyzing extreme precipitation (EP) changes, we also analyzed how these changes relate to total annual precipitation and to changes in precipitable water (PW).

Nearly all observing stations have some level of data missing, and strict criteria were used when evaluating missing data at individual stations. To be included in this analysis, an individual station was required to have a maximum of 10% of its data missing (90% complete)

over the analysis period 1949–2016. Since the analysis time series were compiled by region, for a station to be included in the calculation of its regional time series for a given year, that station had to have at least 300 days with a valid precipitation observation in that year. Lastly, for specific events, an individual event of a specific duration had to have at least 90% of all possible days in that duration period (e.g., a 20-day event had to have at least 18 days with valid observations). For events of less than 10 days, no missing data were allowed.

The final analysis dataset contained the 3,098 U.S. stations shown in Figure 4. Some regions, particularly in the western U.S., had somewhat sparse coverage. However, the use of larger areas for regional aggregation increased the number of stations per region, thereby reducing coverage issues.

The durations and rarities of the events chosen for the analysis were determined by the needs of the civil engineering field when designing long-lived infrastructure. These events are commonly defined by use of an average return interval, or “return period,” which is defined using the annual exceedance probability (the inverse of the average recurrence interval, or ARI).

For this task, the NCEI regional definition for the 48 contiguous United States was used. This 9-region definition (Figure 2) was determined using the Palmer Drought Severity Index and thus has strong links to precipitation regimes (Karl and Koscielny 1982). FORTRAN programs were developed to ingest the data and perform an empirical peaks-over-threshold (POT) analysis for each station. These programs were derivative versions of software used in Kunkel et al. (2003, 2007, 2015) and employed the same methods as described in those publications. A first analysis of POT results for a set of ARIs, or return periods (1-yr, 2-yr, 5-yr, 10-yr, and 20-yr) and durations (1-day, 2-day, 3-day, 5-day, 10-day, 20-day, and 30-day), indicated some lingering precipitation data-quality issues, despite the 14 separate data-quality checks previously applied to the data by data scientists (Durre et al. 2008, Durre et al. 2010). A total of 35 combinations of duration and frequency were analyzed. Although sub-daily data are available, the period of record and spatial density of available stations at that frequency are too short and sparse to allow a robust analysis, and thus sub-daily observations were not used here.

An example of the calculation of the POT time series for a given station for a 5-day event with an ARI of 10 years is as follows: for a 68-year period of record, the expectation is that we would identify 6.8 ($68/10$), rounded up to 7, events. Thus, the seven highest 5-day totals in the period of analysis would make up the time series. Since this results in a large number of zero values in a station time series, 9 regional time series were computed for each of the 35 duration/frequency combinations by first gridding the data. Kunkel et al. (2020b) provide more detailed information on this process.



Figure 4. *The locations of 3,098 stations used for the extreme precipitation trend analysis.*

A trend analysis was performed for event counts for annual, warm season, and cold season periods. Least-squares linear trends and their significance were computed for each time series, mainly to use as a metric of the direction of change (positive or negative). The non-parametric Kendall's Tau was used to assess the significance of the trend. This helped guard against non-linearities, large interannual variability, or non-normality compounding the statistical significance.

Since part of Task 1 includes analysis of annual and seasonal trends in total precipitation, and their relationship to extremes, we computed time series of annual, warm season, and cold season total precipitation and analyzed them in the same way as described in the preceding paragraph. This allowed an assessment of the time of year that contributes the most to the annual and seasonal POT trends for each of the 35 combinations of ARI/durations in each region. For a detailed description of the analysis metrics used, see Kunkel et al. (2020b).

An analysis of trends in PW using data from the NCEP/NCAR and MERRA-2 reanalyses was also performed. Linear trends of the seasonal and annual averages of PW were calculated across CONUS, including by region and nationally. Seasonal and annual average values were used here, rather than extracting only those days that were included in the extremes analysis, since many of the precipitation stations used here only take observations once per day, typically either at 7 am or 5 pm, and it is difficult to determine the exact date the precipitation in an event fell. The assumption here is that annual and seasonal trends in PW are reflective of trends in the higher end of the distribution of PW.

To ascertain the relationship between trends in EP and trends in PW, a correlation coefficient, R , was computed using the seasonal trends (cold or warm) for each region. This resulted in 36 pairs (2 seasons \times 9 regions \times 2 reanalyses) of trends in PW and EP that were cross correlated (for more information, see Kunkel et al. 2020b).

A global analysis was also performed for two ARI–duration combinations using a GEV analysis. The analysis used a partial duration series analyzed over the period 1949–2013.

Task 2: Modify existing software and develop new software to automatically identify key weather systems that cause heavy precipitation in historical reanalyses and climate model simulations.

North American Monsoon

It was expected that moisture flux convergence would be highly correlated with the occurrence of extreme rainfall. Moisture flux convergence estimates were calculated using 6-hr wind and humidity for the 700 mb pressure level for 13 CMIP5 models. In addition, vertically integrated moisture and its convergence using 6-hourly NCEP/DOE Reanalysis 2 were calculated for a set of extreme precipitation events in the summer monsoon period over Arizona and New Mexico for 1979–2013.

Water Vapor

The water vapor environment in the vicinity of extreme precipitation events was characterized by precipitable water. The primary data used in these analyses were the NCEP/NCAR and MERRA-2 reanalyses.

Extratropical Cyclones

An objective feature tracking algorithm is used to identify and track individual extratropical cyclones (ETCs) in the NCEP/NCAR Reanalysis 1 and CMIP5 model simulations. It uses six-hourly sea level pressure (SLP) interpolated onto a Lambert Azimuthal grid with uniform spacing of 0.025 on a unit sphere. The interpolation was performed using a Cressman interpolation with a scale distance of 300 km. Each grid represents approximately 25 000 km² on earth. A point is identified as a candidate ETC center if it meets the following two criteria: 1) it is a local minimum in the SLP field enclosed by an isobar of 2 hPa or more, and 2) the central pressure is lower than any other local pressure minima within 1,500 km—this prioritizes the strongest local minimum in situations where there are broad areas of low pressure that may be disorganized. ETC tracks were assembled by connecting ETC centers from one six-hourly interval to the next, provided that one can be found within 750 km. In this study, we focus on the longer-lived ETCs that exist for at least 72 hours and travel a minimum of 1,000 km.

Fronts

An automated method using machine learning to identify fronts in meteorological data was developed. The specific details of the method are described in Biard and Kunkel (2019). A summary of this method is given here.

In operational meteorological analysis, fronts are identified visually based on the approximate spatial coincidence of a number of quasi-linear localized features: a trough (relative minimum) in air pressure in combination with gradients in air temperature and/or humidity and a shift in wind direction (Stull, 2016). Fronts are categorized as cold, warm, stationary, or occluded, with each type exhibiting somewhat different characteristics. We used a deep learning neural network (DLNN) to mimic the visual fronts-recognition task performed by meteorologists.

The goal for the DLNN front-detection algorithm (DL-FRONT) differs from that in many visual-recognition problems. Front detection does not involve identification of whole-image characteristics or distinct, bounded regions. Instead, the goal is to estimate the likelihood that each cell in a geospatial data grid lies within a frontal zone of a particular category—cold, warm, stationary, occluded, or none. The “none” category allows the algorithm to positively identify

cells that do not appear to lie within any front region. These results are then used to identify paths along which there is a maximum likelihood that a front of a particular type is present in order to produce front lines similar to those drawn by meteorologists.

As explained by Goodfellow et al. (2016), “deep learning” (DL) refers to machine learning algorithms that use multiple layers of non-linear transformations to derive features from input fields. Each successive layer learns to transform the output from one or more previous layers into ever more abstract, conceptual representations of the original inputs. The outputs of a layer are called feature maps in recognition of their conceptual character. Most of these DL algorithms are composed of artificial neural networks (NNs), with 2D convolutional neural networks (CNNs) in common use for learning to detect features in image arrays. Our network uses a technique known as supervised learning, where a “label” dataset containing the desired network outputs for each input is compared with the network outputs, and the differences between them are used to modify the non-linear transformations in the different layers (Deng and Yu 2014).

The DL-FRONT 2D CNN is trained by iteratively optimizing the values of the weights and biases in the convolution filters to minimize the difference between a label dataset and a “predicted” dataset produced by the network from a corresponding input dataset. The difference is measured using a cost, or loss, function. We use the categorical cross-entropy loss function (equation [4]) for training the network, which has the form

$$H(p, t) = - \sum_{i=1}^I \sum_{c=1}^C w_c \log(p_{ic}) t_{ic} \quad (4)$$

where:

$H(p, t)$ = the magnitude of the loss,

p = a set of category vectors taken from the network output,

t = corresponding set of category vectors from the labeled dataset,

w = per-category weight,

I = the number of vectors,

C = the number of categories

Each predicted and label vector has five elements, one for each of the five possible cold, warm, stationary, occluded, and none categories. Each label vector is assigned one and only one category by giving the appropriate element a value of 1 and the others a value of 0. The elements of each predicted vector contain values between 0 and 1, inclusive, which are the estimated category likelihoods for that cell. The lower the likelihood value in the predicted vector for the category marked as correct in the label vector, the larger the contribution to the loss. The per-category weights are used to adjust the relative significance of the contributions from the different categories. Approximately 88% of our data grid cells have no front present, so the loss function is at risk of being dominated by the contribution of the “none” category. Reducing the weight for the “none” category relative to the weights for the other categories will make the loss function less sensitive to that category. Similarly, increasing the weight for a seldom-seen category will make the loss function more sensitive to that category.

The Adam adaptive moment estimation technique (Kingma and Ba, 2015) is the loss minimization strategy used when training the network. Adam is a form of stochastic gradient descent (SGD) that has been shown to perform well in a variety of networks. As with most SGD techniques, Adam has a primary initial learning rate parameter. The learning rate sets the initial magnitude range of the changes to the network weights and biases.

We implemented the DL-FRONT network in Python using numpy (van der Walt et al., 2011) and the Keras deep learning library (Chollet, 2015) on both Tensorflow (Abadi et al., 2015) and The Theano Development Team et al. (2016) (Bergstra, 2010) computational backends. The training application made use of the scikit-learn package (Pedregosa et al., 2011) to provide k -fold cross-validation and hyperparameter search. The “outer” network parameters such as learning rate, number of layers, etc. are referred to as hyperparameters. A significant part of the time spent developing a NN is devoted to optimizing the hyperparameters.

We initially chose a network based on 2D convolution layers with 5x5 kernels because of the structural similarity we saw between a layer of this sort and a finite-difference, second-order spatial derivative function. The visual front detection task described at the beginning of this section, if expressed mathematically, can be thought of as synthesizing the results of various spatial derivatives of the different input measurements at each point in the data grid.

Figure 5 shows a schematic of the resulting DL-FRONT 2D CNN architecture. At the far left of the figure is the input data grid, which is composed of five “feature maps” of 2D meteorological fields (as compared to three feature maps of 2D color fields for an RGB image) on a 1° geospatial grid. These meteorological fields are 3-hourly instantaneous values of air temperature at 2 meters, specific humidity at 2 meters, air pressure reduced to mean sea level, east–west (u) component of wind velocity at 10 meters, and north–south (v) component of wind velocity at 10 meters. The meteorological fields were obtained from the MERRA-2 reanalysis (Gelaro et al. 2017) and were sampled on a 1° latitude longitude grid over a domain of 10° – 77° N and 171° – 31° W. We obtained 37,984 sets of grids for the time span 2003–2015.

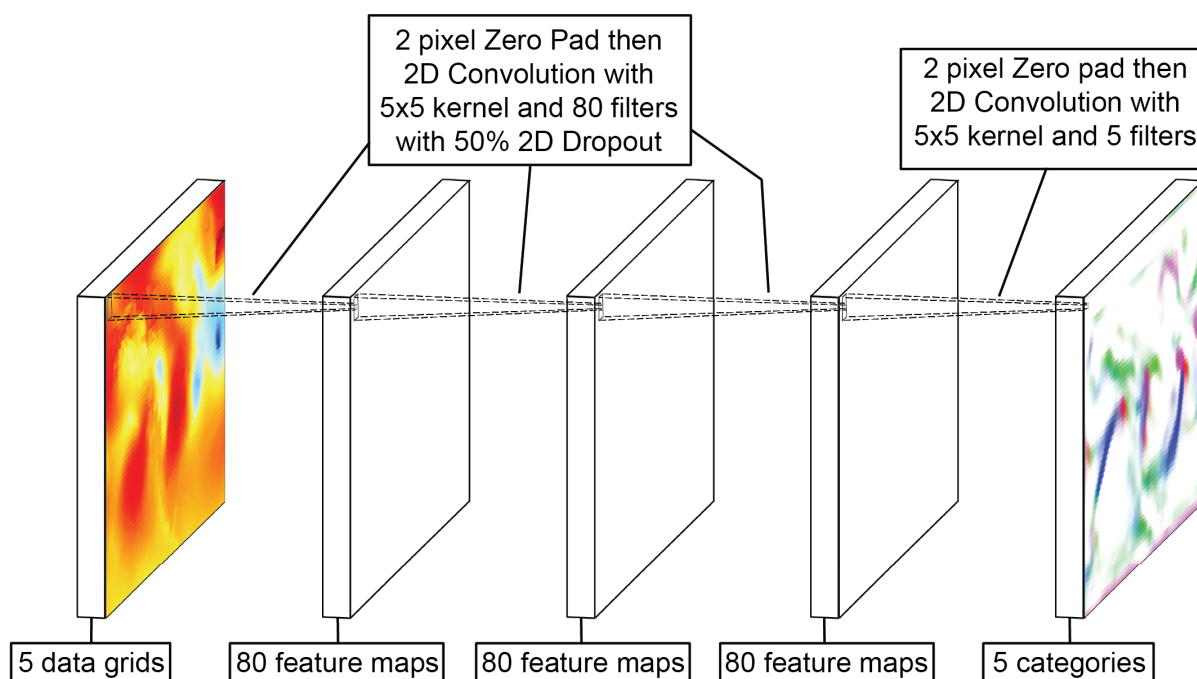


Figure 5. Schematic of the DL-FRONT 2D CNN architecture. The five-category input data grid on the left contains the five input surface meteorological 2D fields (temperature, humidity, pressure, u-component of wind, v-component of wind). The five-category output data grid on the right contains five 2D likelihood estimates for the five front categories (cold, warm, stationary, occluded, and none).

The output of the DL-FRONT 2D CNN is a set of spatial grids that are, in essence, maps of likelihood of the presence of the five different front categories (cold, warm, stationary, occluded, and none). In order to use these results in follow-on studies, we needed to obtain polylines describing the locations of the front boundaries. We developed an application using numpy (van der Walt et al. 2011) and scikit-image (van der Walt et al. 2014) that traces out “ridgelines” of the likelihood fields for the different front types and reduces them to a set of latitude–longitude polylines labeled by front type.

A data grid for each time step consisted of the frontal boundary lines that matched the resolution and spatial extents of the MERRA-2 data grids for each of the frontal types. Each front was drawn with a transverse extent of 3° (3 grid cells) to account for the fact that a front is not a zero-width line and to add tolerances for possible transverse differences in position between the Coded Surface Bulletin (CSB) polylines and front signatures in the MERRA-2 dataset. The training, validation, and evaluation were restricted to a region around North America where the rate of front crossings recorded by the CSBs was at least 40 per year to ensure adequate sample size for robust validation methods.

Initial algorithm development was done using the NARR (Mesinger et al. 2006) data with a resolution of ~ 32 km on a Lambert Conformal Conic coordinate reference system (CRS) grid centered on North America. Because fronts are inherently characterized by large spatial gradients perpendicular to the front, our initial hypothesis was that the best results would be achieved by using data with the highest available spatial resolution. However, tests indicated that better results were obtained by using a subset of grid points at a coarser resolution of ~ 96 km (three NARR grid cells). We speculate that the analysis of a larger spatial region is better able to detect the differences between the two air masses demarcated by a front, particularly when state variables change gradually across a frontal boundary. In such cases, the natural spatial heterogeneity may mask the frontal signal at the 96 km (3 NARR) spatial scale. We then trained with the MERRA-2 dataset and found that the validation accuracy and loss when training were better than what we found with the NARR dataset. As a result, we switched to using MERRA-2 on a latitude–longitude grid.

Frontal boundary crossing rates (the frequency of days on which fronts pass a point location) were used as the climatological metric in our goal to produce accurate climatologies of extreme events. This was important for determining how well DL-FRONT performs in comparison to the CSB labeled dataset. Comparisons of monthly or seasonal front-crossing rates over a spatial grid are much less subject to minor differences in front location than comparisons of polylines at individual time steps. These comparisons can also be used to analyze any variations in results that depend on geographic location or time. The rates were calculated for each front type and for the aggregate case of all front types.

The monthly front-crossing rate for a given front type and month was calculated by selecting the appropriate front polylines from the 3-hourly time steps for the month and accumulating front-crossing counts in a spatial grid with cells of 1° latitude by 1° longitude. At each time step, we determined which grid cells were intersected by the selected front polylines and incremented counts for those grid cells. To keep slow-moving or stationary frontal

boundaries from exaggerating the counts, we implemented a 24-hour blanking period. When the count in a grid cell was incremented in a time step, any following intersections for that grid cell were ignored for the next seven 3-hourly timesteps, the counts thus representing “front days.” Once the month’s counts were accumulated, the rate in crossings per day for each grid cell was determined by dividing the total count by the number of time steps used and multiplying by eight. We calculated “all fronts” rates by selecting the front polylines for all types in each time step. We followed the same overall process to calculate seasonal rates as well, using the standard meteorological seasons of December–January–February, March–April–May, June–July–August, and September–October–November.

By studying initial results using the CSB front polylines, we determined that grid cells were regularly skipped when the polylines from successive time steps were rasterized with a width of one grid cell. The rate at which frontal boundaries move transverse to their length is often high enough that two sets of width-one rasterized polylines from adjacent three-hour time steps do not cover adjacent grid cells. This led to coverage gaps when accumulating the front crossings for a single day, where it was clear that the fronts should be sweeping out contiguous regions. These gaps produced spatial striping in the monthly and seasonal front-crossing-rate data grids, with repeated bands of lower rate values visible in various locations across the data grid. We found that the spatial striping effect disappeared if we rasterized our polylines with a width of three grid cells. The 24-hour blanking period in our counting algorithm prevents overcounting if fronts are moving slowly enough that the wider rasterized polylines overlap.

The final DL-FRONT network was trained with 14,353 input and labeled data grid pairs (the number of time steps over the period with available CSB data) covering the years 2003–2007 using 3-fold cross-validation. Each of the three folds used 9,568 (two-thirds of total) data grid pairs randomly chosen from the full set and randomly ordered in time. Training stopped when the loss did not improve for 100 epochs (passes through the training dataset), leading to training that lasted 1,141, 1,142, and 1,136 epochs, respectively.

A sample output of the DL-FRONT algorithm and the corresponding CSB front locations for August 1st, 2009, at noon UTC (a period not used in training) is shown in Figure 6. The DL-FRONT results are very similar to the CSB fronts in terms of the general locations. There are spatial discrepancies that are sometimes large enough that the fronts locations do not overlap, and there are several discrepancies regarding the type of front. The DL-FRONT results are missing a Pacific coast cold front and a Western mountains stationary front from the CSB observations. DL-FRONT identifies additional fronts in the Pacific Ocean and on Baffin Island in the Arctic; these are beyond the areas regularly analyzed for fronts by the National Weather Service.

The trained network was evaluated by calculating the metrics discussed below for both the 2003–2007 training data and the 2008–2015 validation data. We combined the results for the four different front types to produce a two-category front/no-front dataset and produced metrics for the same two date ranges.

The percentage of grid cells in the 5 different types is shown in Table 3 for the CSB and DL-FRONT. In the CSB, the percentage of grid cells categorized as front is in the range of 12.3–12.6% for the training and validation periods. The DL-FRONT algorithm identifies fronts in 11.7–11.9% of the grid cells. Thus, there is a slight undercount but little difference between the training and validation periods. The percentage of the different frontal types is similar between the CSB and DL-FRONT except for warm fronts, which are undercounted by DL-FRONT. Table

3 also shows that there is a major asymmetry between the front type categories, with ~88% of the grid cells falling into the no-front category.

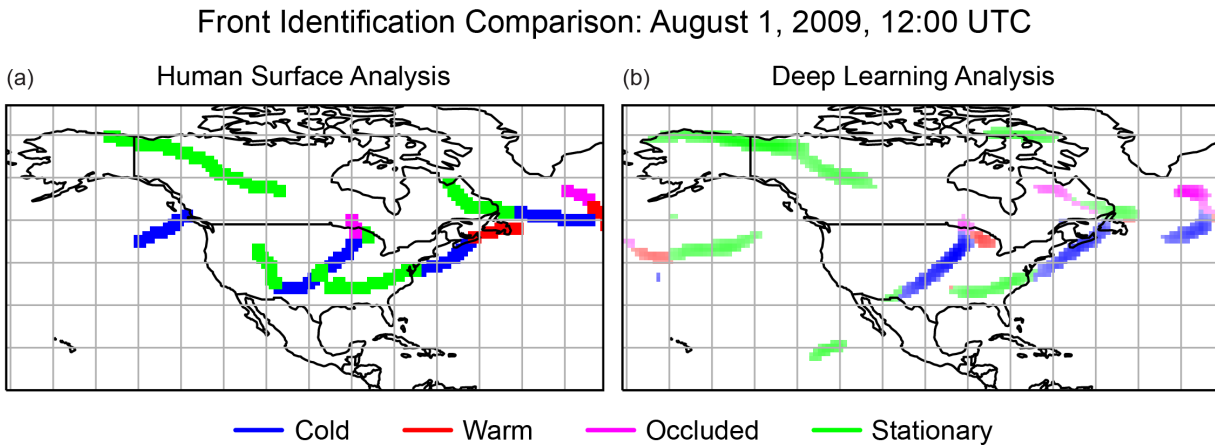


Figure 6. Side-by-side comparison of CSB (a) and DL-FRONT (b) front boundaries for 2009-08-01 12:00:00. The CSB fronts were drawn three grid cells wide. The intensities of the colors for the different front types in the DL-FRONT image represent the likelihood value (from 0.0 to 1.0) associated with each grid cell.

Table 3. Counts of CSB and DL-FRONT grid cells over the training and validation time ranges and fraction of grid cells occupied by different front types.

	2003–2007	2008–2015	2003–2015
Total	65,679,328	106,877,056	172,556,384
Cold			
CSB	3.71%	3.94%	3.85%
DL-FRONT	3.81%	3.75%	3.77%
Warm			
CSB	1.65%	1.82%	1.75%
DL-FRONT	1.16%	1.17%	1.16%
Stationary			
CSB	5.34%	5.23%	5.27%
DL-FRONT	5.31%	5.20%	5.24%
Occluded			
CSB	1.59%	1.60%	1.60%
DL-FRONT	1.61%	1.58%	1.59%
Any			
CSB	12.29%	12.58%	12.47%
DL-FRONT	11.89%	11.70%	11.77%
None			
CSB	87.71%	87.42%	87.53%
DL-FRONT	88.11%	88.30%	88.23%

The polyline extraction application was run to obtain front polylines from the full DL-FRONT front likelihoods dataset. The result was a front polyline dataset covering the same 2003–2015 time span as the CSB dataset. The CSB and DL-FRONT polylines were then used to calculate corresponding sets of monthly front-crossing rates. Monthly and seasonal front-crossing rates were calculated for both datasets for each front type and for the simplified front/no-front case. The front-crossing rates were used to calculate monthly and seasonal climatologies using the entire 13-year span.

Task 3: Perform a thorough analysis of the meteorological causes of heavy precipitation increases over the last few decades, building on previous work.

North American Monsoon

The moisture flux convergence (MFC) was investigated as a large-scale indicator of extreme precipitation. This can be separated into two terms:

$$MFC = CT + AT \quad (5)$$

where:

MFC = moisture flux convergence,

CT = convergence term,

AT = advection term

The convergence term represents the product of the specific humidity and horizontal mass convergence. The advection term denotes the horizontal advection of specific humidity.

Fifty extreme daily precipitation events in the observations are identified for the period of summer 1979–2015 over Arizona and New Mexico, respectively. Our analysis indicates that all 50 extreme daily precipitation events are associated with MFC at 700 mb in both Arizona and New Mexico. We calculated the MFC, the CT, and AT in equation (5), using the 6-hr data of NCEP/DOE Reanalysis 2 at 700 mb.

Water vapor

It is useful to adopt the concepts and terminology introduced and used by Emori and Brown (2005), O’Gorman and Schneider (2009), and Nie et al. (2018) as a framework for evaluating extreme precipitation (EP) scaling by precipitable water (PW) given other factors also affecting EP. This is given by:

$$EP \cong PW \Omega \Gamma \quad (6)$$

where:

Ω = metric of the vertical velocity (upward vertical velocity [VV] is equivalent to $-\omega$ when using units of hPa),

Γ = the vertical covariances of the standardized PW and Ω , i.e., the covarying vertical changes of Ω and PW

However, as pointed out by O’Gorman and Schneider (2009) and supported by Nie et al. (2018), when the thermal structure of the atmosphere is moist adiabatic on synoptic scales, then Γ is small relative to PW, Ω , and—given other sources of uncertainty, such as measured precipitation amounts—the spatial and temporal resolutions of the global climate models (GCMs), and so on, Γ is assumed to be 1. We use PW to represent the thermodynamic contribution, while the dynamic component ($-\omega$) is strongly affected by specific weather types producing upward VV. PW is the result of circulation from all weather types, only indirectly dependent on VV through evaporation. This enables us to develop direct relationships between EP and PW over various time frames, both concurrently and over various time rates of change.

To better understand the relationship between EP events and PW, two similar EP metrics were computed for each station that we used in the Global Historical Climatology Network-Daily (GHCND) dataset. First, the time series of the yearly maximum daily precipitation, or annual maximum series (AMS), was identified. This is the starting point for many IDF curves (Bonnin et al. 2004). Second, the amount of precipitation on those days exceeding the 1-yr 1-day recurrence threshold was identified. This is referred to as the partial duration series (PDS), and it simply consists of the highest 69 daily events for a station with a complete 69-year period of record in the GHCND dataset. We found considerable overlap between these two metrics; on average, more than two-thirds of the PDS and AMS values are the same events. The average PDS precipitation amount is greater than the AMS. The largest event in both series represents a return interval of more than 50 years. This highlights why the NCEP/NCAR reanalysis was given preference over MERRA-2.

Weather Systems

The analysis of the meteorological causes of historical extreme precipitation events used several sets of data. A master dataset was created from several individual datasets developed in this project and one standard dataset produced by NCEI. This includes the extreme events for each of the 3,104 stations for the 35 duration/recurrence level combinations, the locations of fronts, the tracks of extratropical cyclones (ETCs), and tropical cyclone (TC) tracks from the International Best Track Archive for Climate Stewardship (IBTrACS). The specifics of these datasets are:

- **Fronts:** The automated frontal detection algorithm was applied to the 1980–2017 period of MERRA-2 reanalysis data. This resulted in a 38-yr record of fronts for all of North America and adjacent ocean areas, including Hawai‘i and Alaska.
- **Extratropical Cyclones:** ETC tracks were generated for the period of 1980–2017 from the NCEP/NCAR reanalysis.
- **Tropical Cyclones:** TC tracks were obtained from the IBTrACS dataset (Knapp et al. 2010).

The nearest meteorological system was identified for each day in the observational record of each station. This was accomplished by first calculating the great-circle distance between each station event location and the location of any existing TC centers, ETC centers, and frontal boundaries during the 24-hr period ending at the time of observation. The minimum of these distances for each 24-hour period was recorded for each event.

Each day was assigned a predominant meteorological cause, regardless of precipitation amount. This was accomplished using the calculated meteorological event proximities and the following logic:

IF there existed a TC center within 500 km, the cause was assigned as “TC.”

ELSE IF there existed an ETC center within 500 km, the cause was assigned as “ETC.”

ELSE IF there existed a frontal boundary within 500 km, the cause was assigned as “FRONT.”

ELSE IF the month was within the range June to September and the observation fell within Arizona, New Mexico, Utah, Nevada, California, or Colorado, the cause was assigned as “MONSOON.”

ELSE the cause was assigned as “OTHER.”

Then, this information was used to assign a meteorological cause to each extreme precipitation event for each station. For extreme events longer than one day, a predominant cause was determined by weighting each daily cause during the event by the fractional contribution of that day’s precipitation to the event total.

The result of this analysis was a master dataset of causes for each extreme precipitation event.

A pairwise time series of extreme events and their attributed causes was calculated for each return period and duration for the period 1980–2017 in order to determine the average seasonal exposure to each cause. The occurrence of extreme events was then correlated with the incidence of both fronts and ETCs.

Task 4: Perform extensive analyses of CMIP5 model simulations, identifying the occurrence of weather systems causing heavy precipitation for historical and future simulations.

Precipitation

A comprehensive analysis of changes in CMIP5 extreme precipitation data was completed. Specifically, a statistically downscaled dataset from CMIP5 known as Localized Constructed Analogs (LOCA) was obtained (Pierce et al. 2014). The GEV method was used to estimate changes for various future periods using the R package “ismev” (<https://cran.r-project.org/web/packages/ismev/index.html>).

North American Monsoon

Moisture flux convergence was computed for future simulations from 13 CMIP5 models

Water Vapor

Kunkel et al. (2013) analyzed maximum precipitable water data from a set of CMIP5 models. This work was extended by including several additional CMIP5 models with the necessary upper air data to compute PW, bringing the total number of models with historical and future PW data to 13.

Future changes in precipitable water (PW) were estimated from 13 global climate models (GCMs) for which 4-dimensional data (3 spatial dimensions and time) were available. Precipitable water is not commonly stored in the CMIP5 model archive and thus it had to be calculated from vertical pressure level data. Because of its common availability across multiple models, we used daily specific humidity on pressure levels of 700, 500, and 250 hPa. Precipitable water (PW) is calculated as:

$$PW_{700-250} = \left\{ \frac{(q_{700} + q_{500})(P_{700} - P_{500})}{2\rho_w g} + \frac{(q_{500} + q_{250})(P_{500} - P_{250})}{2\rho_w g} \right\} \quad (7)$$

where:

P_L = the pressure at level L ,

q_L = the specific humidity at level L ,

ρ_w = the density of water,

g = the acceleration of gravity

$PW_{700-250}$ clearly represents only a portion of total PW. The choice of 700 hPa as the lowest level was driven by high terrain in the western United States. This is the lowest standard level that is above the grid box ground level over all of CONUS in all models. Although not representing all of PW, it is the change in PW, not absolute PW, that is used in calculating adjustment factors. The assumption is that the fractional change of PW over the pressure interval of 700–250 hPa is similar to the fractional change of PW over the entire atmosphere, i.e.,

$$\Delta \ln PW_{700-250} \cong \Delta \ln PW_{sfc-top} \quad (8)$$

where:

sfc and *top* = earth's surface and the top of the atmosphere, respectively

The GCMs for which the necessary data were available are listed in Table 2. For each GCM, daily $PW_{700-250}$ values were computed from equation (7) for each grid point for the period 1976–2099 for the RCP4.5 and RCP8.5 scenarios. Then, for each grid point, the 30-yr maximum value of $PW_{700-250}$ was determined (PW_{max}). Values of PW_{max} were calculated for the historical period 1976–2005 and 7 overlapping future periods (2011–2040, 2021–2050, 2031–2060, 2041–2070, 2051–2080, 2061–2090, 2070–2099). Once these calculations were completed on the model's native grid, the PW_{30max} values were re-gridded to a common 2.5° longitude by 2.0° latitude grid. The percentage change at each grid point was calculated as

$$\Delta PW_{30maxfut} = 100\% (PW_{30maxfut} - PW_{30maxhist}) / PW_{30maxhist} \quad (9)$$

A multi-model mean and standard deviation for each common grid point were then calculated from the values of the 13 models. Finally, these gridded values were interpolated to the 10°×10° CONUS boxes.

Fronts

The fronts-detection algorithm requires 3-hourly data for surface wind, pressure, temperature, and specific humidity. Data at this high temporal resolution were not commonly provided in the CMIP5 archive. Thus, we used two other sources of climate model data.

The CMIP6 archive provides a wider range of variables and temporal resolution. While this archive is still being populated by modeling groups, we found 4 models with the required variables and temporal resolution (see Table 2). Data at the 3-hourly time resolution was downloaded for the period of 1980–2100 for several emissions scenarios. In addition, the CAM5 HAPPI simulations were available for global warming levels of 1.5°C, 2.0°C, and 3.0°C with the required variables at 3-hr resolution. The simulations included multiple ensembles totaling 100 years of data for a historical period (1996–2015) and 50 years of data for a future period (2106–2115).

Extratropical Cyclones

Future changes in ETCs were calculated by using historical information on the fraction of extreme precipitation events arising from ETCs of different intensity and speed of movement. We found that the fraction of ETCs that were associated with extreme precipitation events differed from the total number of ETCs. Specifically, a higher fraction of extreme precipitation events occurred with weaker and slower-moving ETCs (see Task 3 in the Results and Discussion section). We used this information to develop a weighting scheme that was applied to the future CMIP5 simulations.

The matrix weighting scheme was developed by categorizing ETCs into 5 bins of intensity (I) measured by the minimum sea level pressure (SLP) during the life of the ETC and into 6 bins of speed of movement (V) measured over the life of the ETC. This level of granularity was established initially to ensure that important relationships were not missed. However, testing determined that coarser bin granularity was satisfactory (see step 9 below).

The total number of ETCs in each of the 30 combined categories was counted by season. Then, the extreme precipitation events identified as being caused by ETCs were extracted from the causes dataset developed under Task 3. For each of these extreme precipitation events, the intensity/speed of movement category of the ETC that caused the event was determined. These

were then counted in each of the same 30 combined categories by season. The counts were then analyzed to determine whether there was a disproportionately high or low number of extreme precipitation events relative to the total number of ETCs in each category, which was used to refine the application of future ETC changes to the adjustment factors. The following equations represent this weighting scheme.

Let $N_{ETC}(I, V, S)$ = the number of historical extreme precipitation events from ETCs by intensity category (I), speed of movement (V), and season (S)

$$N_S = \sum_{I=1}^{N_I} \sum_{V=1}^{N_V} N_{ETC}(I, V, S) \quad (10)$$

The fraction of EP events caused by ETCs in each of the 30 intensity/speed-of-movement categories by season, $W_{ETC}(I, V, S)$, is

$$W_{ETC}(I, V, S) = \frac{N_{ETC}(I, V, S)}{N_S} \quad (11)$$

These are used as weights representing the fraction of historical EP events caused by ETCs by category.

The procedure for application of these weights to the future CMIP simulations follows.

Let $H_{ETC}(I, V, S)$ = the number of ETCs by intensity category (I), speed of movement (V), and season (S) in the historical CMIP5 simulations

Let $F_{ETC}(I, V, S)$ = the number of ETCs by intensity category (I), speed of movement (V), and season (S) in the future CMIP5 simulations

$$A_S = \sum_{I=1}^{N_I} \sum_{V=1}^{N_V} W_{ETC}(F_{ETC} / H_{ETC}) \quad (12)$$

where:

A_S is the fractional adjustment factor

This form of the adjustment factor weights categories of future changes in ETCs in proportion to their contributions in the historical record to EP occurrence.

The specific computational procedures that were used were:

1. Calculate the number of ETCs as a function of intensity (I), speed of movement (V), and seasons (S) that are associated with the observed EP events.

The bins for intensity are i) SLP <980 mb, ii) SLP is between 980 mb and 990 mb, iii) SLP is between 990 mb and 1,000 mb, iv) SLP is between 1,000 mb and 1,010 mb, and v) SLP >1,010 mb.

The bins for speed of movement are i) less than 5 m/s, ii) between 5 m/s and 10 m/s, iii) between 10 m/s and 15 m/s, iv) between 15 m/s and 20 m/s, v) between 20 m/s and 25 m/s, and vi) and greater than 25 m/s.

2. Calculate the total number of ETCs as a function of intensity, speed of movement, and seasons. These ETCs are identified from NCEP Reanalysis 1.
3. Calculate the total number of ETCs as a function of intensity, speed of movement, and season in the CMIP5 historical runs (1981–2004) and RCP8.5 simulations of 2007–2012 (23 models).
4. Calculate the total number of ETCs as a function of intensity, speed of movement, and seasons from CMIP5 RCP8.5 simulations for the period 2021–2099.
5. Calculate $W_{ETC}(I, V, S)$ in equation (11) using observed extreme events and ETCs in the NCEP Reanalysis 1.
6. Compare ETCs between NCEP Reanalysis 1 and CMIP5 historical runs for the same period of 1981–2012 (excluding 2005–2006 as noted above), and perform a simple bias correction.
7. Apply the bias correction to the CMIP5 RCP8.5 simulations for the period 2021–2099.
8. Calculate the fractional adjustment factor.
9. We repeated steps 5–8 many times with different bin category thresholds to find out the optimum bin sizes for both intensity and speed of movement. We randomly removed 3 years from the 30-year period and calculated the adjustment factor for 30 times. We found that the results are robust using only two bins for intensity (SLP < 1,000 mb and SLP > 1,000 mb) and two bins for speed (< 15 m/s and > 15 m/s). Thus, our original 30-category framework was reduced to a 4-category framework, easing the computational and complexity burden.

Task 5: Determine the meteorological causes and trends of heavy precipitation events at global military installation sites identified by DoD.

Most of the same methodologies used in Tasks 2 and 3 were used in Task 5 for sites outside the contiguous United States (OCONUS). Results for this task focus on sites in Alaska, Hawai‘i, and Guam. This task leveraged work done in Tasks 1, 2, and 3 to extend the analysis to selected DoD OCONUS sites. Daily climate data for most DoD installations around the world are currently available at NCEI and were used in this project. Sites with period-of-record observations of at least 50 years were most suitable for study in order to minimize uncertainties in the design value estimates for larger average recurrence interval (ARI) levels. Precipitation

data for those sites were used to identify heavy events and to determine meteorological causes of those events using approaches developed in previous projects. These approaches are based on the use of model-based reanalyses, such as the NCEP/NCAR reanalysis (Kalnay et al. 1996), to determine the synoptic meteorological patterns (e.g., frontal activity, ETC, TC, etc.) associated with the heavy precipitation events.

Station Selection

The initial set of nine OCONUS stations did not all match one to one with stations in existing meteorological datasets. Furthermore, there were often large gaps of missing data. Therefore, it was necessary in some cases to choose a station adjacent to the proposed DoD site, and in some cases a hybrid station was created by combining different data for that station from different sources (e.g., Eielson Air Force Base [AFB]). The GHCND dataset (Menne et al. 2012) was used along with data obtained from the Air Force's 14th Weather Squadron based in Asheville, NC.

Seven locations, four in Alaska, two in Hawai'i, and one in Guam, were chosen for this task. Figure 7 shows the annual time series for four of the locations, one from each of the regions used in the meteorological causes analysis. In two instances (Schofield Barracks/Fort Shafter in Hawai'i and Andersen AFB and Naval Base Guam), locations were represented by only one observed precipitation time series due to their close proximity. In both cases, data were sourced from a nearby civilian observing site due to a lack of data at the military sites. Examination of Figure 7 shows that most of the analysis time series had complete or nearly complete time series, with little or no missing data. Although the data time series start at different years, each is long enough to provide a robust analysis.

Methods and Analysis

Heavy precipitation events were identified for each of the seven locations for the period of record for each site. The events corresponded to the 1-day duration 1-yr return period events, resulting in a total of 474 events.

Once the heavy events were identified, the three main analyses performed for this task were an identification of the meteorological causes of each of the 474 events, an analysis of water vapor changes in climate model simulations for the future, and an analysis of future climate model-based changes in the meteorological causes identified for the observed heavy events. Since many of the locations analyzed here are close in proximity, they were combined into a regional analysis to provide more robust results. This resulted in four regional definitions: central Alaska, southern Alaska, Guam, and Hawai'i.

Synoptic type classification was performed for 473 OCONUS events ranging from 1949 through 2018. Each event was classified according to one of the following meteorological synoptic classifications:

TC = Tropical Cyclone
ETC = Extratropical Cyclone
FRONT = Frontal Boundary
SLOW = Subtropical Low
AMC = Air Mass Convection (mainly thermodynamic forcing)

For each event, the following reanalysis fields (Kalnay et al. 1996), at 4-hr intervals per day, were examined via an animated GIF file (Figure 8):

- Sea level pressure (mb)
- 500 mb geopotential height
- Precipitation rate (mm/hr)
- Convective precipitation rate (mm/hr)
- Air temperature (°F)
- Precipitable water (mm)
- Omega 700 mb (Pa/s)

After analyzing the animated image and considering all of the synoptic features and characteristics, a final meteorological synoptic classification was assigned.

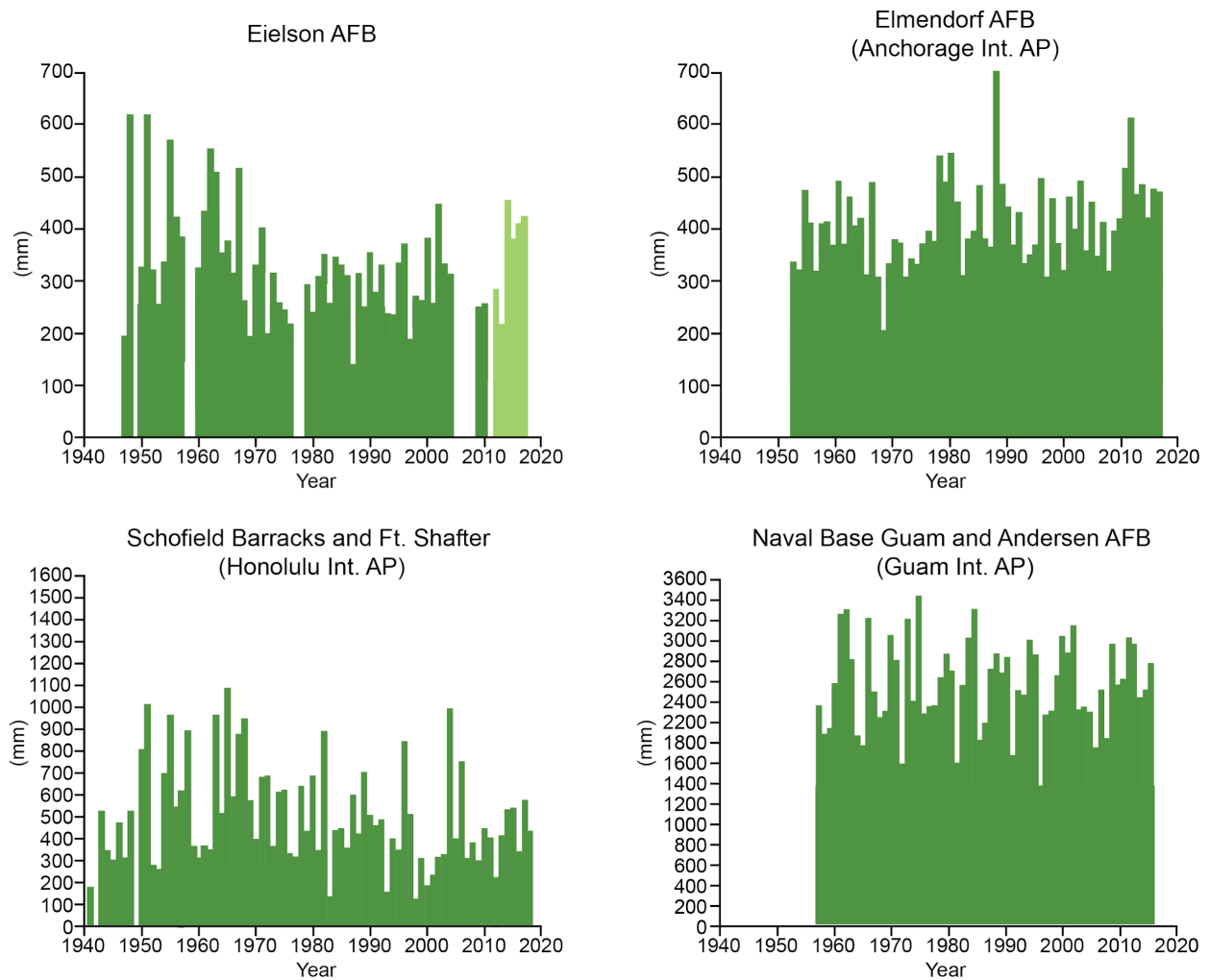


Figure 7. Time series of annual total precipitation for four locations, one for each region analyzed in the determination of meteorological causes of heavy precipitation events. The Eielson AFB case required the creation of a composite data series using nearby observations (light green) due to missing data at the end of the data series.

19851020.00Z.04.056

Ft. Shafter, Wahiawa, Hawaii

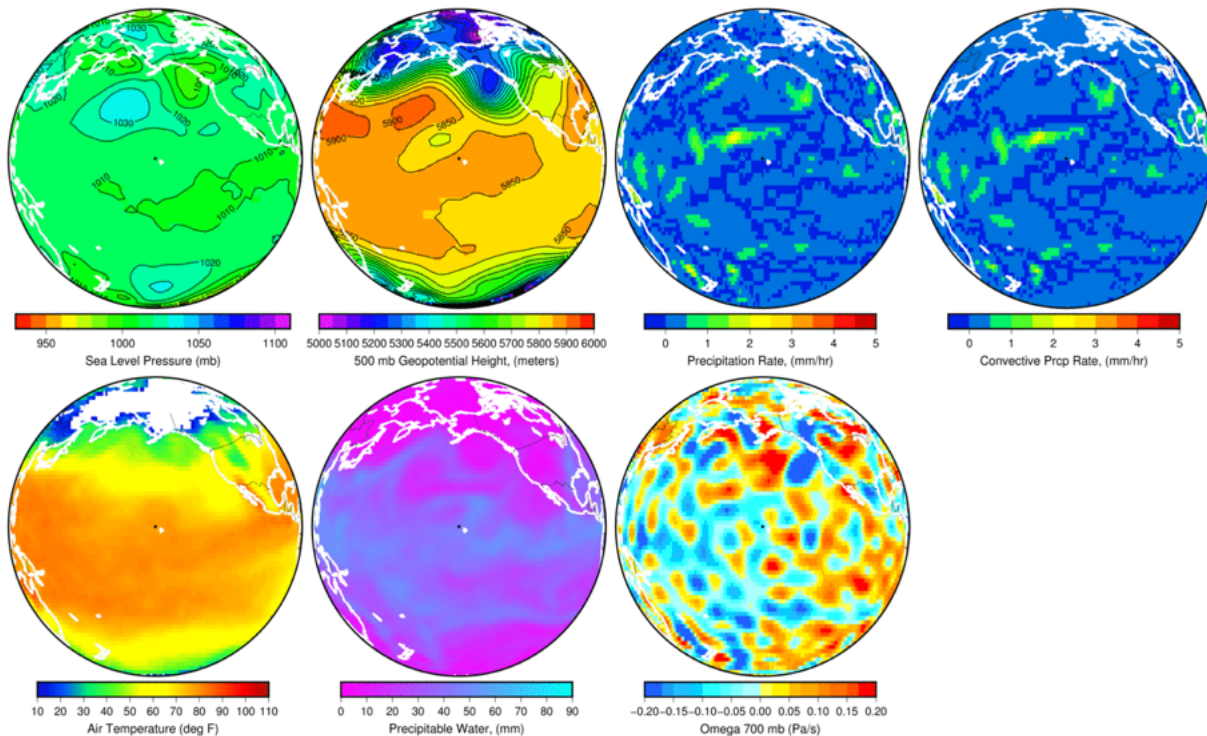


Figure 8. Sample image from animation loops of the various NCEP/NCAR reanalysis fields used to identify the meteorological causes of each heavy precipitation event.

Task 6: Develop applications, including adjustment factors for current IDF values, and incorporate them into the delivery mechanism for current IDF values to provide convenient and reliable access to appropriate values by the civil engineering community.

Future changes in water vapor and weather systems were quantified from our analysis of climate model simulation data. These analyses determined the coefficients in the ClimAtological effects Under Synoptic Extreme States (CAUSES) equation. The future Intensity-Duration-Frequency (IDF) values were calculated as the product of the current design value from NOAA Atlas 14, a factor representing the change in water vapor, and a second factor representing the change in weather systems.

Uncertainties were also incorporated into the future design values. Sources of uncertainty include 1) uncertainties in the future pathway of greenhouse gas emissions, 2) differences among GCMs, including the sensitivity in each model of the climate system to greenhouse gas concentration changes, 3) the structural differences related to the two methods, and 4) the statistical uncertainties arising from the estimates of various parameters in the NOAA Atlas 14 baseline estimates of extreme precipitation. These uncertainties were incorporated into the estimates through the following considerations.

The uncertainties in the future pathway of greenhouse gas emissions were incorporated by performing analyses for two future pathways, a lower emissions scenario (RCP4.5) and a higher emissions scenario (RCP8.5). These are the same scenarios used in the Fourth U.S. National Climate Assessment (<https://nca2018.globalchange.gov/>). Differences in GCMs were

addressed by examining the results of multiple models and incorporating various outcomes into the range of IDF values. Structural differences in methods were addressed by calculating future changes with two very different methods to calculate adjustment factors. The best estimate of future IDF values is given by an average of the adjustment factors from using all models listed in the GCM dataset table (Table 2). Finally, statistical uncertainties in NOAA Atlas 14 values are provided on their website as a 10th–90th percentile range around their mean values. We used those ranges as one component of our range of values and combined them with the uncertainties from the GCM analyses.

A website is used to provide access to the results of this project in the form of NOAA Atlas 14 precipitation design values adjusted for potential future climate change (<https://serdp.ncics.org/>). The website incorporates the following features:

1. Choice of location from a) a list of military installations; b) clicking on a map of the United States; or c) entering a latitude and longitude
2. Choice of moderate or high emissions scenarios
3. Choice of future period of 2025, 2035, 2045, 2055, 2065, 2075, 2085
4. Tabular output for a return period of 1 to 100 years and durations of 1 hr to 30 days

Results and Discussion

Task 1: Perform a historical analysis of U.S. and global trends in precipitation in the range of frequencies and durations of relevance to civil engineers (e.g., NOAA NWS 2020 covers ARIs of 1 through 1,000 years and durations of 5 min through 60 days).

United States

The climatology (average) and trends in annual and seasonal (warm–cold) total precipitation are shown in Figure 9. There is much spatial variability in both the climatology and the trends in total annual and seasonal precipitation across the contiguous United States (CONUS). Generally, precipitation totals increase from southwest to northeast in the country. The largest and most significant trends in total precipitation are found in the northern regions (excluding the NW) and are mainly due to trends in the warm season.

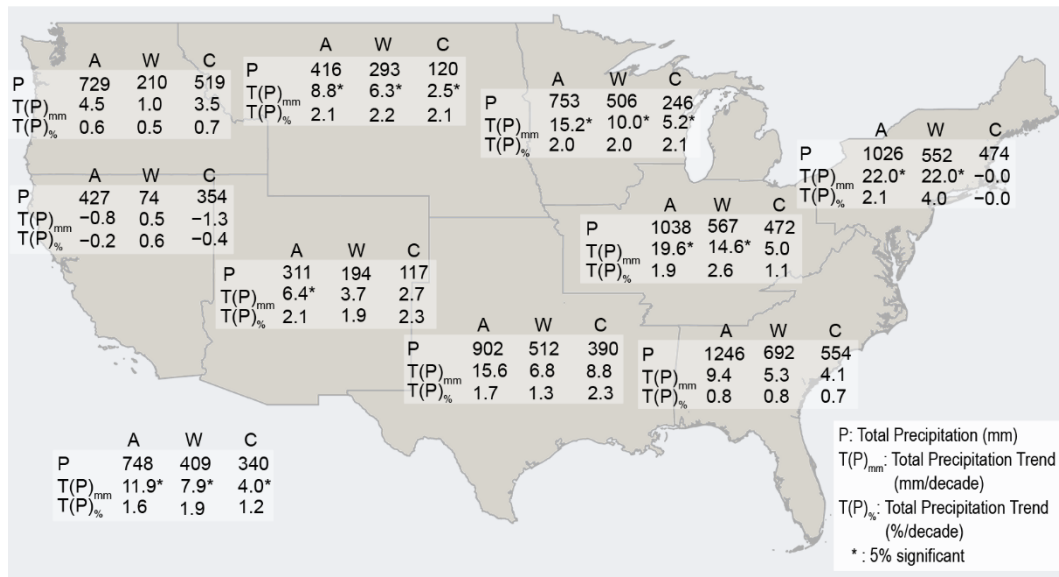


Figure 9. Precipitation climatology statistics for the nine NCEI climate regions and the United States as a whole. *P* is the total average precipitation without regard to season (label *A* for annual) and for the warm (*W*) and cold (*C*) seasons, $T(P)_{mm}$ is the linear trend (1949–2016; mm per decade), and $T(P)\%$ is the trend in percent per decade of the total $[T(P)_{mm}/P] \times 100\%$. Statistically significant trends (two-tailed test) are noted by *.

Figure 10 shows the annual trends (in percent per decade) for the 35 average recurrence interval (ARI)–duration combinations described earlier for both the 1949–2016 and 1979–2016 periods. There is a distinct gradient from west to east in the sign and magnitude of the trends. Large positive trends occur in the NE, SE, S, C, ENC, and WNC NCEI regions. It is notable that the magnitude and significance of the trends get larger as the ARI gets longer (e.g., 1-yr vs 20-yr recurrence interval), and this is true not just in the eastern part of CONUS but also across the entire country. Furthermore, the trends for both analysis periods (1949–2016, 1979–2016) show similar results.

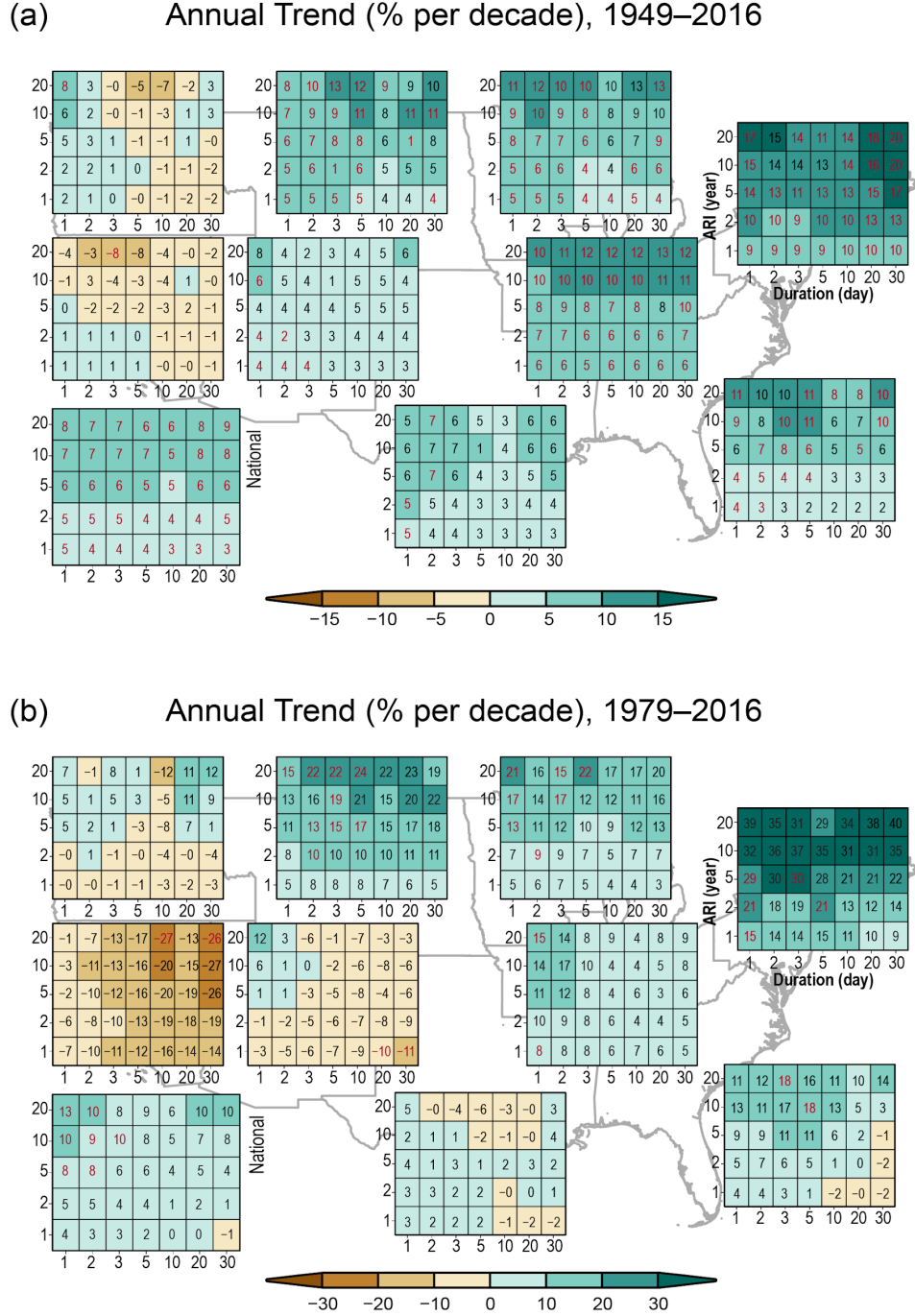


Figure 10. Trends (percent per decade) in the frequency of occurrences for each region during the (a) 1949–2016 and (b) 1979–2016 periods for the 35 ARI–duration combinations. Decreasing trends are displayed in shades of brown, and increasing trends are displayed in shades of green. Statistically significant trends are shown in red-colored numbers (0.05 significance level for a two-tailed test).

Seasonal results (not shown; see Figures 6 and 7 in Kunkel et al. 2020b) indicate that, with the exception of the NW, W, and S regions, the other six have much larger trends in the warm season compared to the cold season. For the NW and W regions, cold season trends are

generally larger, although trend results tend to be mixed. The S region shows trends of similar magnitude for both the warm and cold seasons. The relative magnitude and sign of the extreme precipitation (EP) trends tend to be similar to trends in total precipitation for each region, indicating a common factor, such as total column water vapor (PW), may be impacting the distribution of precipitation intensities.

It is also useful to compare trends in EP to trends in total annual and seasonal precipitation. The percent contribution of a given trend in an extreme precipitation metric to the trend in total precipitation is given by δ where:

$$\delta_{ARI,d,s} = [T(EP_{ARI,d,s})/T(P_s)] \times 100\% \quad (13)$$

where:

$T(EP_{ARI,d,s})$ = the trend of the EP for a given ARI, duration (d), and season (s),

$T(P_s)$ = the trend in total seasonal or annual precipitation

Figure 11 shows the annual values for δ for each ARI–duration combination.

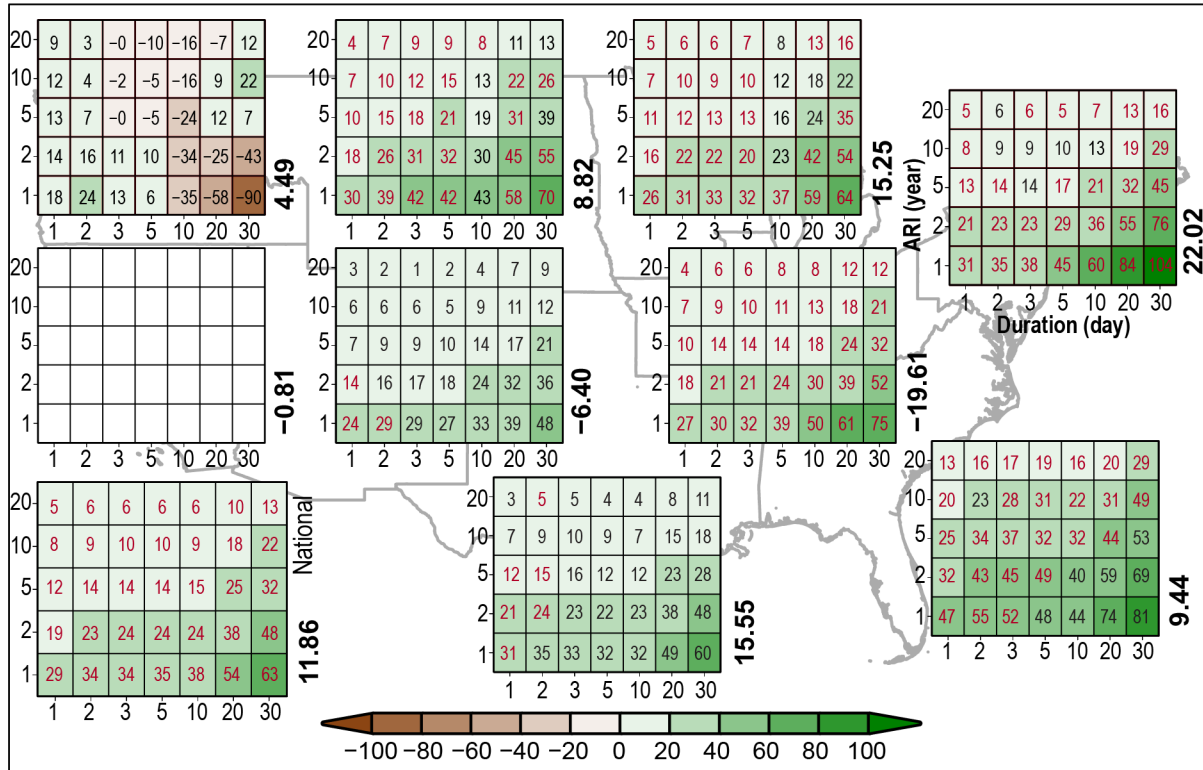


Figure 11. Values of $\delta_{ARI,d,annual}$ with red denoting statistical significance of $T(EP)$ at the 0.05 level. The rotated numbers to the right of each table are annual values of $T(P)$ (mm/decade). The W region is blank since $T(P_{annual})$ is near zero.

All regions except the NW and W show relatively high values of δ , meaning that the trend in extreme precipitation is responsible for a significant portion of the trend in total precipitation. In particular, the shorter recurrence interval events (e.g., 1-yr recurrence) show

much larger values for δ than the longer recurrence interval (e.g., 20-yr recurrence), indicating that even though the shorter recurrence interval events are smaller in magnitude (since, by definition, they are less rare), they contribute more to the trend in total precipitation. Additionally, the longer-duration, shorter recurrence interval events (e.g., 1-yr recurrence, 30-day duration) generally show larger values for δ , indicating that trends in these kinds of events contribute a large proportion to the trend in total precipitation. A warm/cold season breakdown of δ (not shown; see Figures 9 and 10 in Kunkel et al. 2020b) shows the warm season contributing much more to the trend in total precipitation across most of the country.

Water Vapor Trends

Increases in atmospheric water vapor are a potential driver of changes in future precipitation rates, and water vapor is expected to increase as the climate continues to warm. Trends in PW and their relationship to trends in the various duration–frequency combinations were examined. Figure 12 shows the linear trends in PW for annual, cold, and warm seasons from both the NCEP/NCAR and MERRA2 reanalyses. The periods analyzed are slightly different, owing to the different periods for the two reanalyses. Results from the two reanalyses show large agreement between the two, with the MERRA2 showing more spatial detail due to its finer grid resolution. Both show upward trends in PW for most of the country, although MERRA2 shows more spatial uniformity and stronger trends, particularly during the warm season. The seasonal breakdown also shows decreasing trends in PW in the SW region during the cold season, and the NCEP/NCAR reanalysis shows small decreasing trends in PW during the warm season in parts of the western U.S. and stronger decreases in the cold season along the East Coast.

Regionally, trends in PW and trends in EP are positively correlated over all the ARI–duration definitions, reinforcing the notion that increases in PW are a key factor in increases in heavy precipitation events. Further, correlations are generally higher across all ARIs for the shorter-duration events and lower for longer-duration events. Since this is opposite to what was expected, it is postulated that other factors, such as synoptic weather patterns and possibly persistence of large-scale circulation patterns, have an important influence as durations increase.

Summary

1. Nationally, trends are upward for all 35 combinations of durations and return intervals.
2. Regionally, there is much spatial and temporal variability in the EP trends, and they vary with the different combinations of return interval and duration.
3. Seasonally, the warm season has larger and more significant trends in EP events than the cold season.
4. Results shown here indicate that trends of PW are an important seasonal and regional factor contributing to the observed changes in EP events.

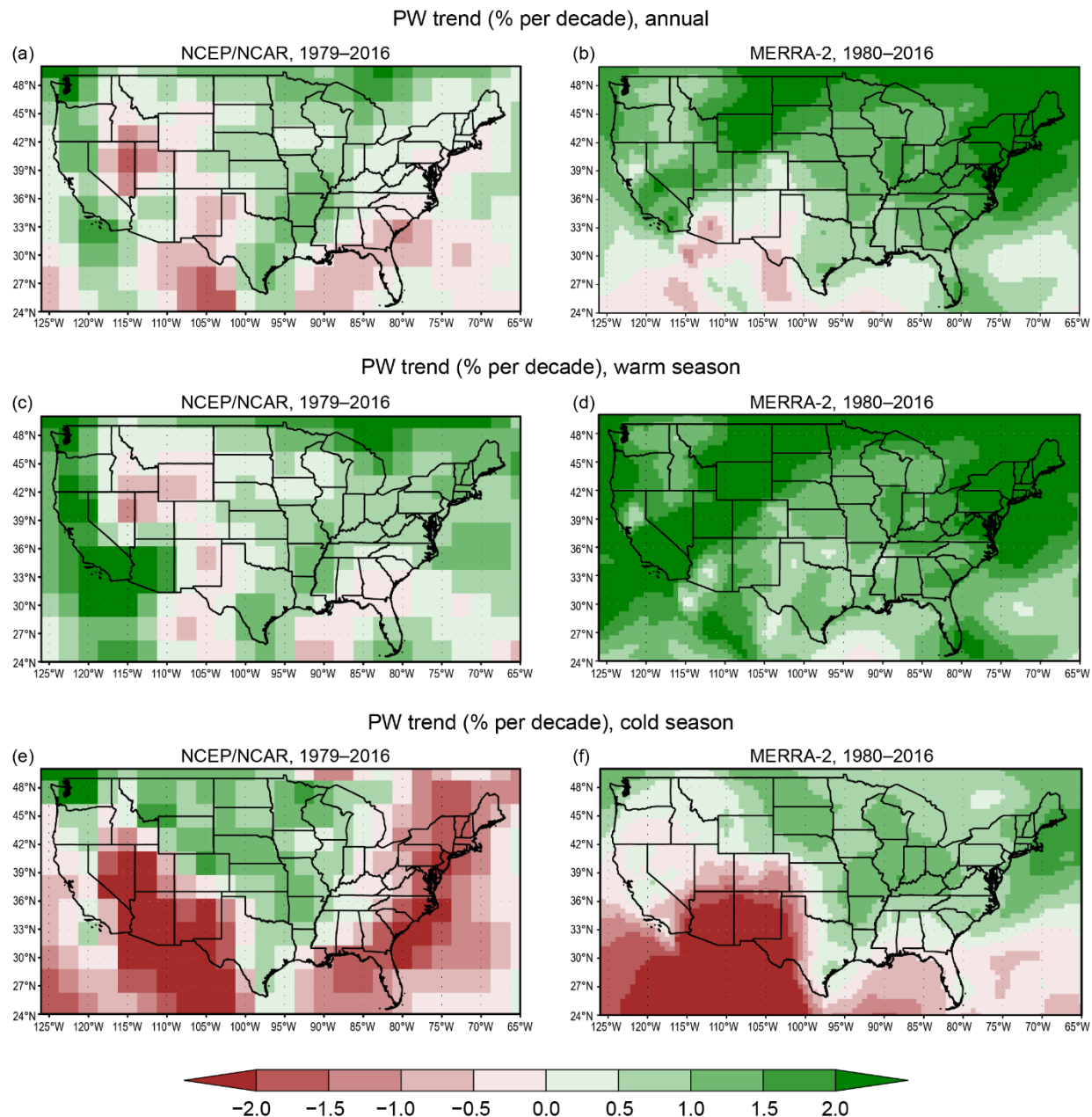


Figure 12. Least-squares trends in water vapor (% per decade) from the (left column) NCEP/NCAR reanalysis and (right column) MERRA2 reanalysis for (a and b) annual, (c and d) warm season, and (e and f) cold season.

Global Analysis

Results for 5-day-duration, 10-yr-return-period events are shown in Figure 13, with blue showing increases and red decreases. Generally, more areas are blue, particularly in North America and much of Europe, Russia, China, and Australia. Given our need for more detailed analysis in the United States and its territories, additional global-scale analysis was not performed.

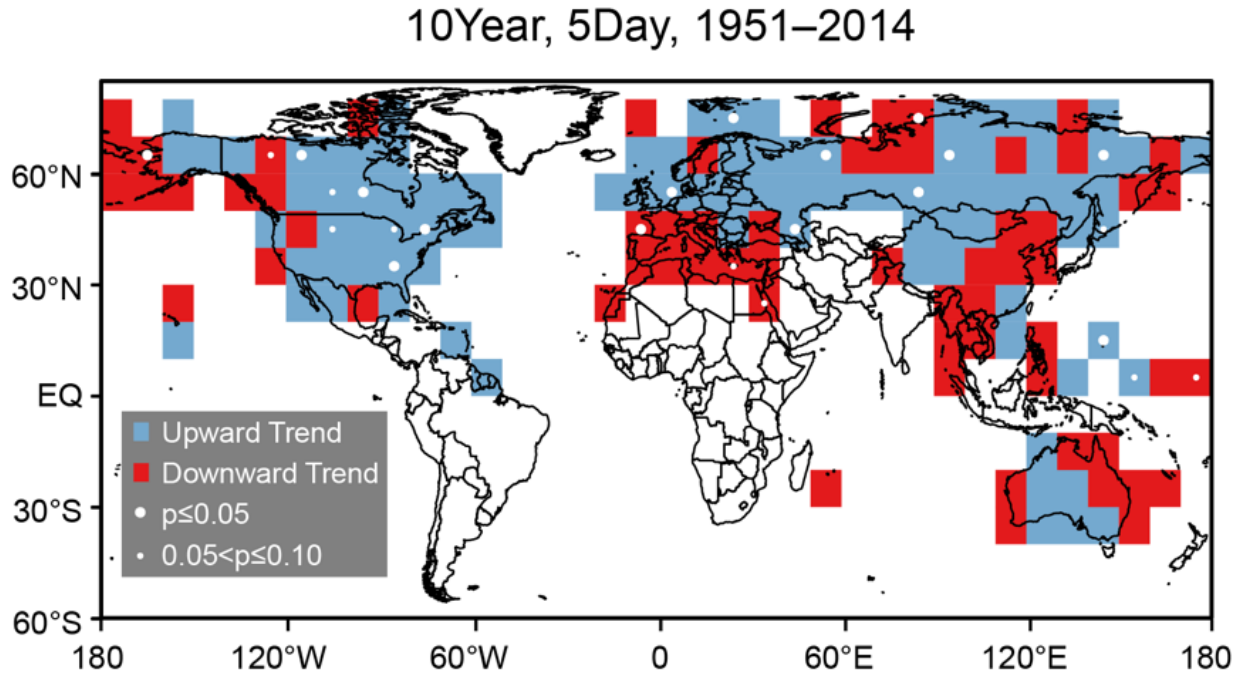


Figure 13. The 1951–2014 trend of the number of 5-day total precipitation events exceeding the station-specific threshold for an average 10-yr recurrence interval. White dots indicate that the trend is significant at the $0.05 < p \leq 0.10$ (small dots) or $p \leq 0.05$ (large dots) level.

Task 2: Modify existing software and develop new software to automatically identify key weather systems that cause heavy precipitation in historical reanalyses and climate model simulations.

Fronts

Figure 14 shows maps of the Coded Surface Bulletin (CSB) and DL-FRONT MERRA-2 seasonal front/no-front rate climatologies for a rectangular region of interest (ROI) centered over CONUS. The use of this region minimizes edge effects produced by the uneven spatial coverage of the CSB dataset. The maps show a large degree of similarity between the seasonal front-crossing rates calculated using the human-created and Deep Learning Neural Network (DLNN)-generated fronts.

Seasonal Front Climatology, 2003–2015

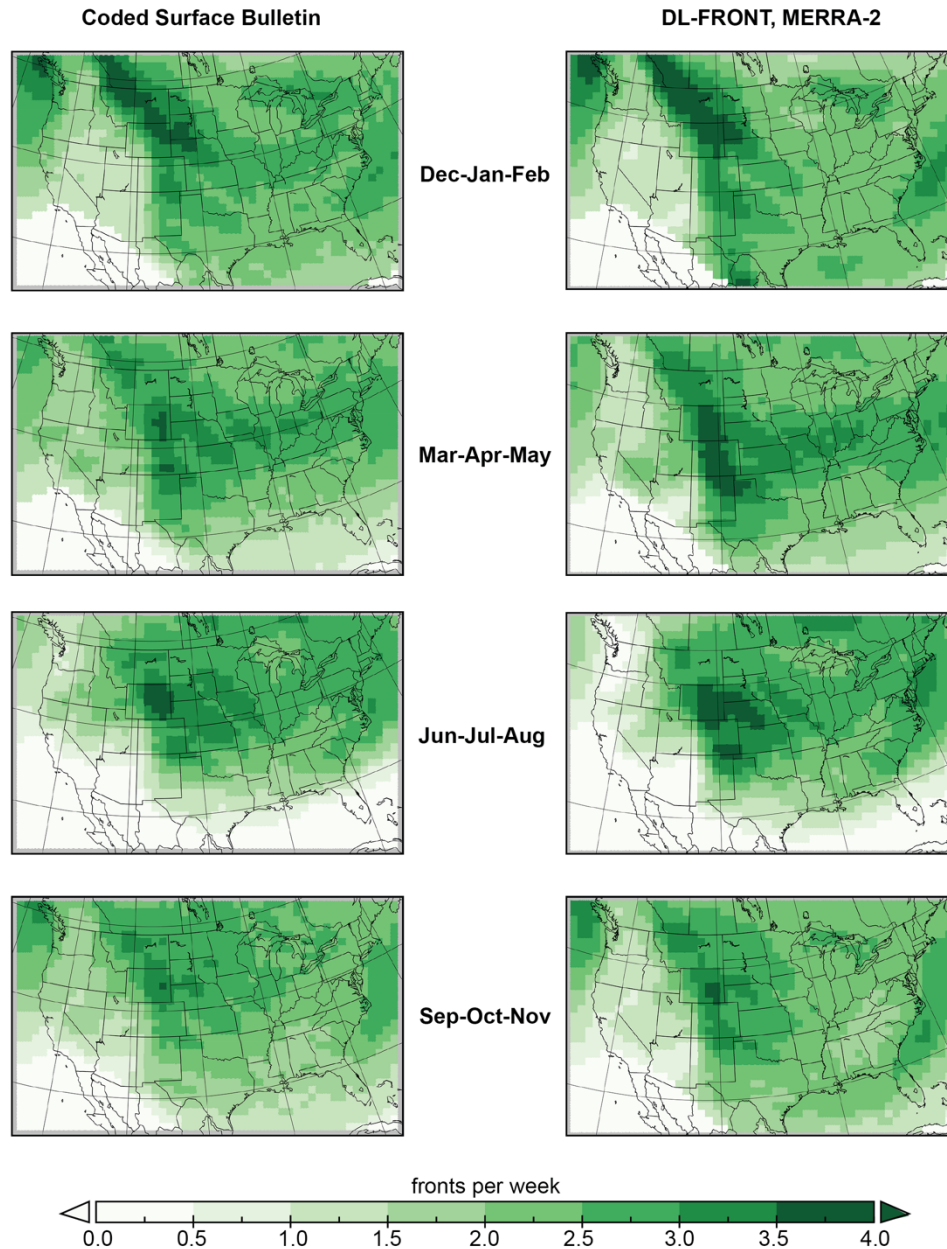


Figure 14. Maps of seasonal front-crossing rate climatologies (2003–2015) for the CSB and DL-FRONT datasets.

Figure 15 shows scatterplots comparing the values shown in each pair of maps in Figure 14. Each scatterplot displays the one-to-one correlation line, a line displaying the mean of the differences between the paired DL-FRONT and CSB front-crossing rate values, and a pair of lines that delineate ± 2 standard deviations of the differences. The Pearson's correlation coefficient for each distribution is greater than 0.94 in every case, indicating a high degree of correlation. While most paired grid point values are within 10% of each other, some pairs differ by considerably more. The ± 2 standard deviation limits, which encompass 98% of DL-FRONT

MERRA-2 grid point climatology values, are ~ 0.5 front crossings every week, compared to CSB climatology values centered around 2–3 fronts every week, indicating that some grid point pairs differ by about 20% or more.

Figure 16 compares the results of taking spatial averages of the CSB and DL-FRONT MERRA-2 monthly front/no-front rate climatologies over the CONUS ROI of Figure 14. The spatial averages track each other quite closely, with the values always falling within ± 1 standard deviation of each other.

Temporal variability was assessed by averaging the monthly front/no-front crossing rates over the entire CONUS ROI. Monthly crossing rates were expressed as anomalies from the monthly climatology values. A comparison of the time series of monthly crossing rates (Figure 17) indicates good agreement, with an r value of 0.70 ($p < 0.01$). Both time series have relatively low values during 2008–2010, with higher values on either side of that time period. However, the CSB time series has a statistically significant ($p < 0.01$) upward trend, while the MERRA-2 trend is essentially zero. Since 2012, the CSB has been higher than MERRA-2 in most months. The reasons for this are not known and beyond the scope of this study.

MERRA-2 vs CSB Seasonal Front Crossing Rates, 2003-2015

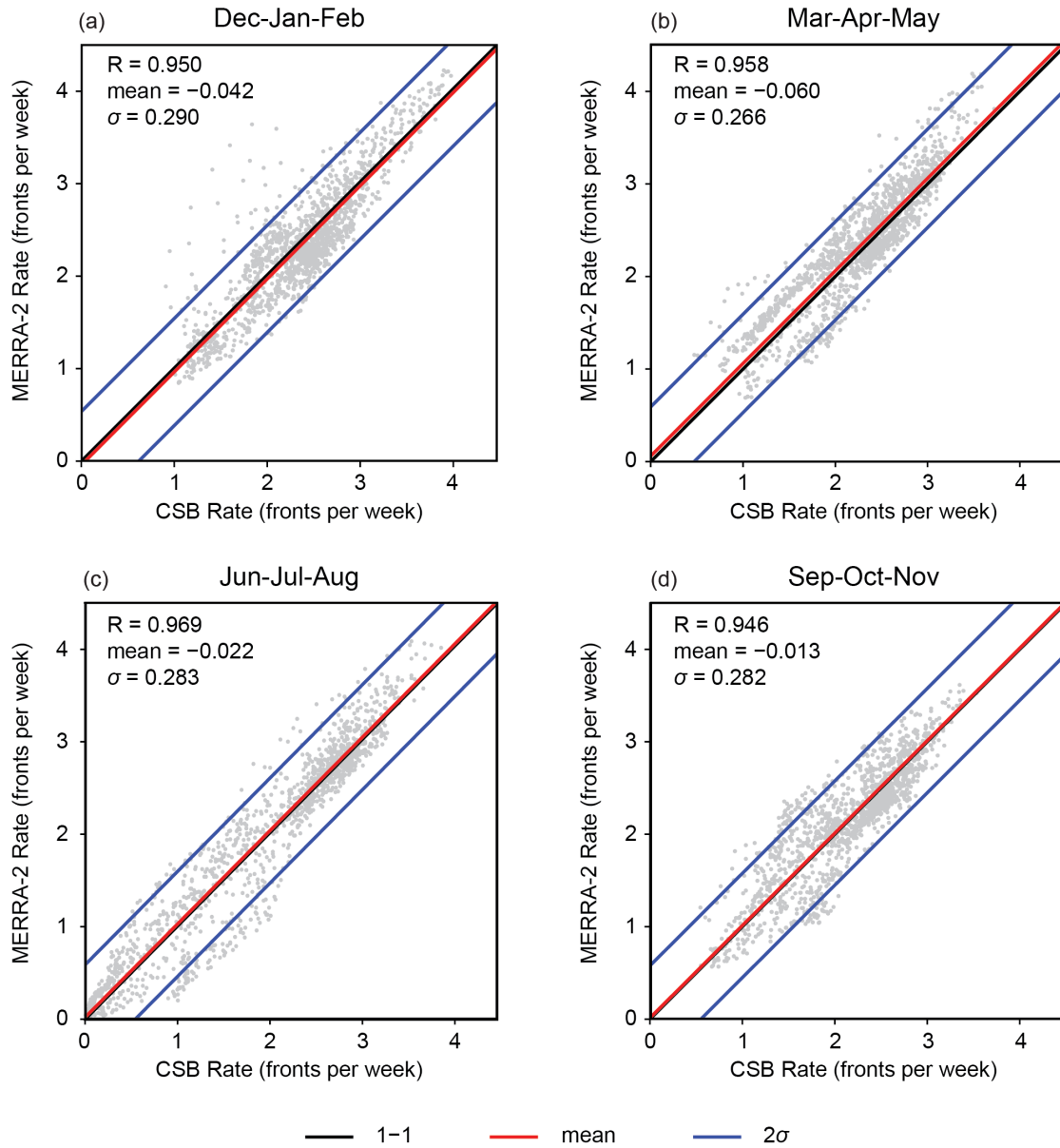


Figure 15. Scatterplots comparing the DL-FRONT and CSB seasonal front-crossing rate climatologies over the CONUS-centered ROI.

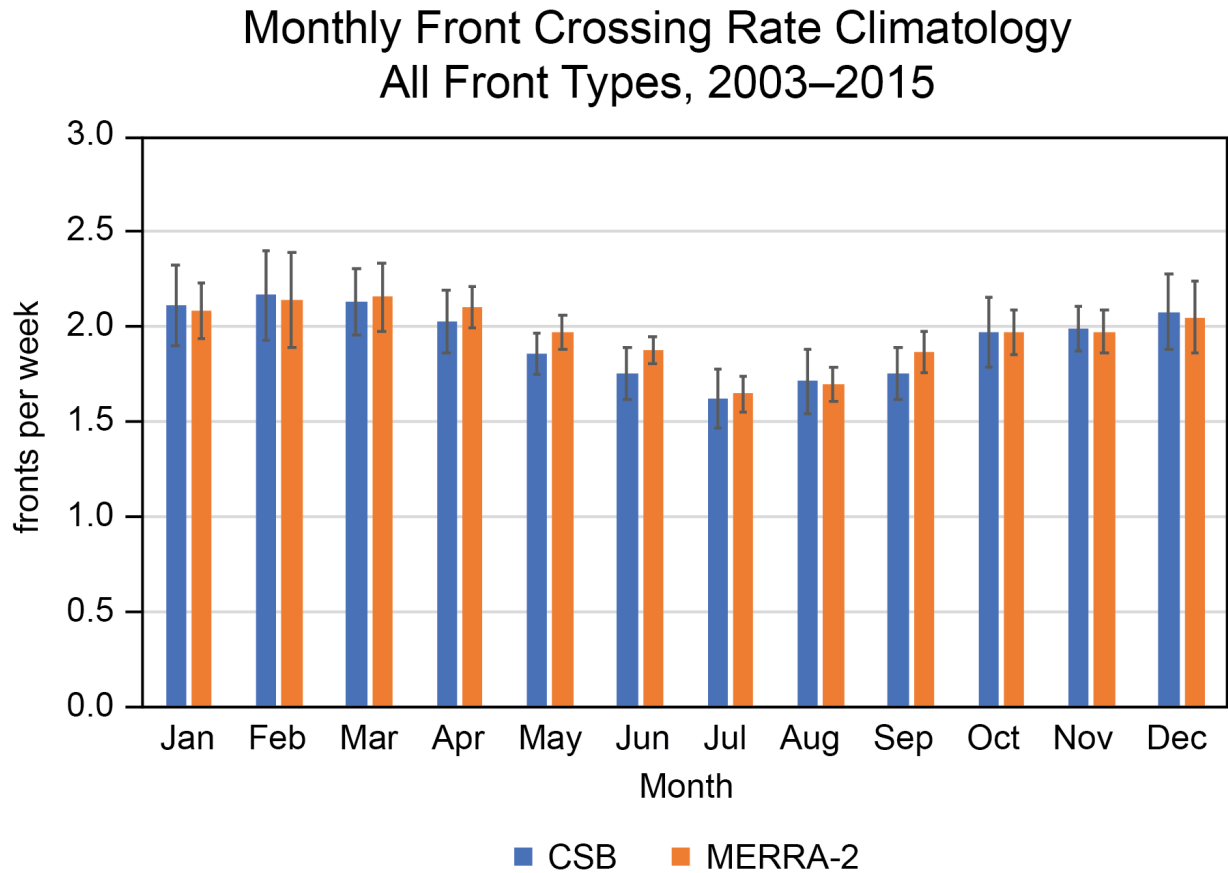


Figure 16. Comparison of the front/no-front CSB and DL-FRONT MERRA2 monthly front-crossing rate climatologies spatially averaged across the entire CONUS ROI.

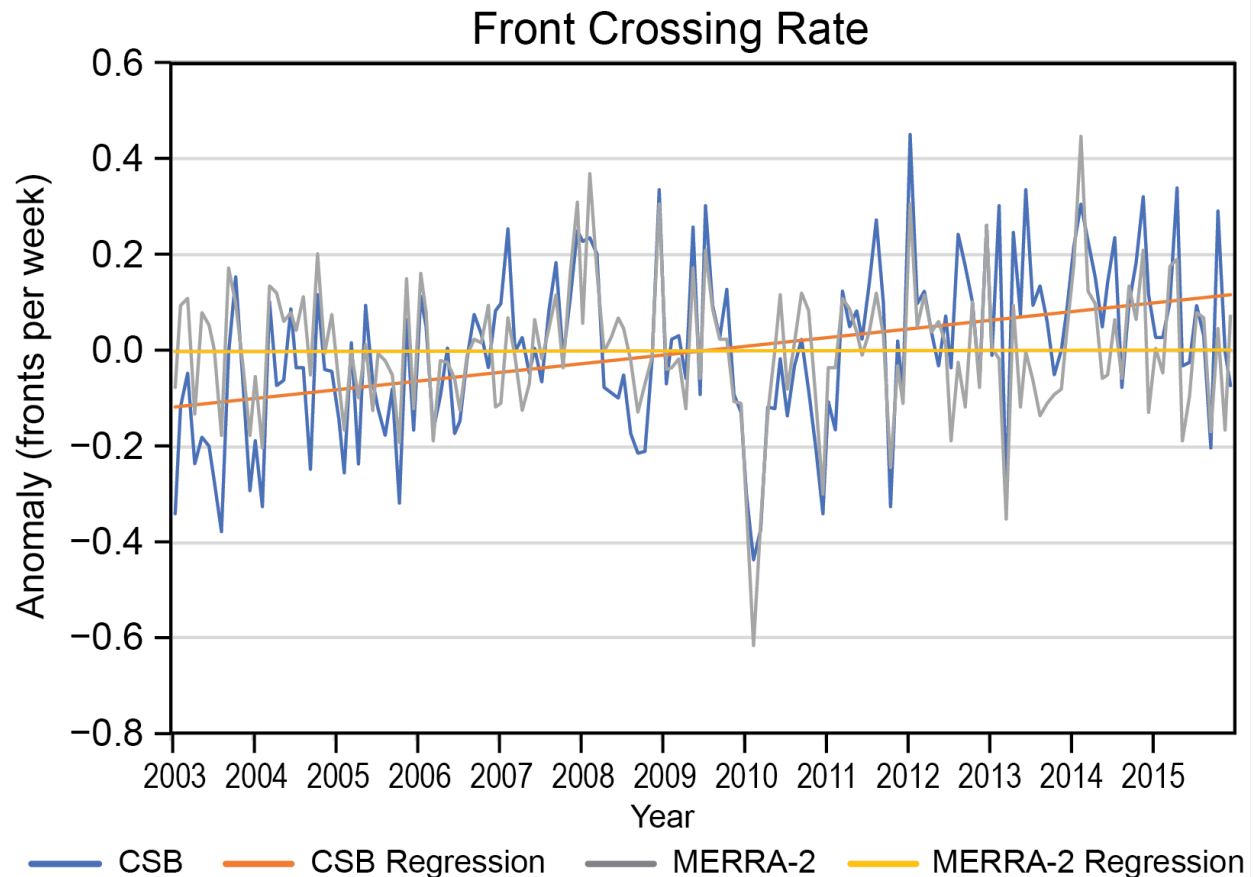


Figure 17. Monthly time series of the domain-averaged frontal-crossing rate anomalies for CSB and for MERRA-2 analyzed by DL-FRONT.

Task 3: Perform a thorough analysis of the meteorological causes of heavy precipitation increases over the last few decades, building on previous work.

Water Vapor

A variety of analyses were completed to better understand the relationship between PW and daily EP events of various intensities. This included empirical probability distribution partitioning, time-rate-of-change analyses, and simple correlation analyses. Empirical probability distributions were calculated in Kunkel et al. (2020a). They clearly show that the PW probability distribution is shifted toward higher values during days with EP events. The degree to which this occurs varies by region, as depicted in Figure 18. Moisture-limited regions of the western U.S. have less separation compared to eastern areas. This points to the importance of PW as related to the amount of precipitation from EP events, as EP events generally have more precipitation in the eastern half of the United States. Additionally, it also points to the importance of geography and related weather and climate regimes.

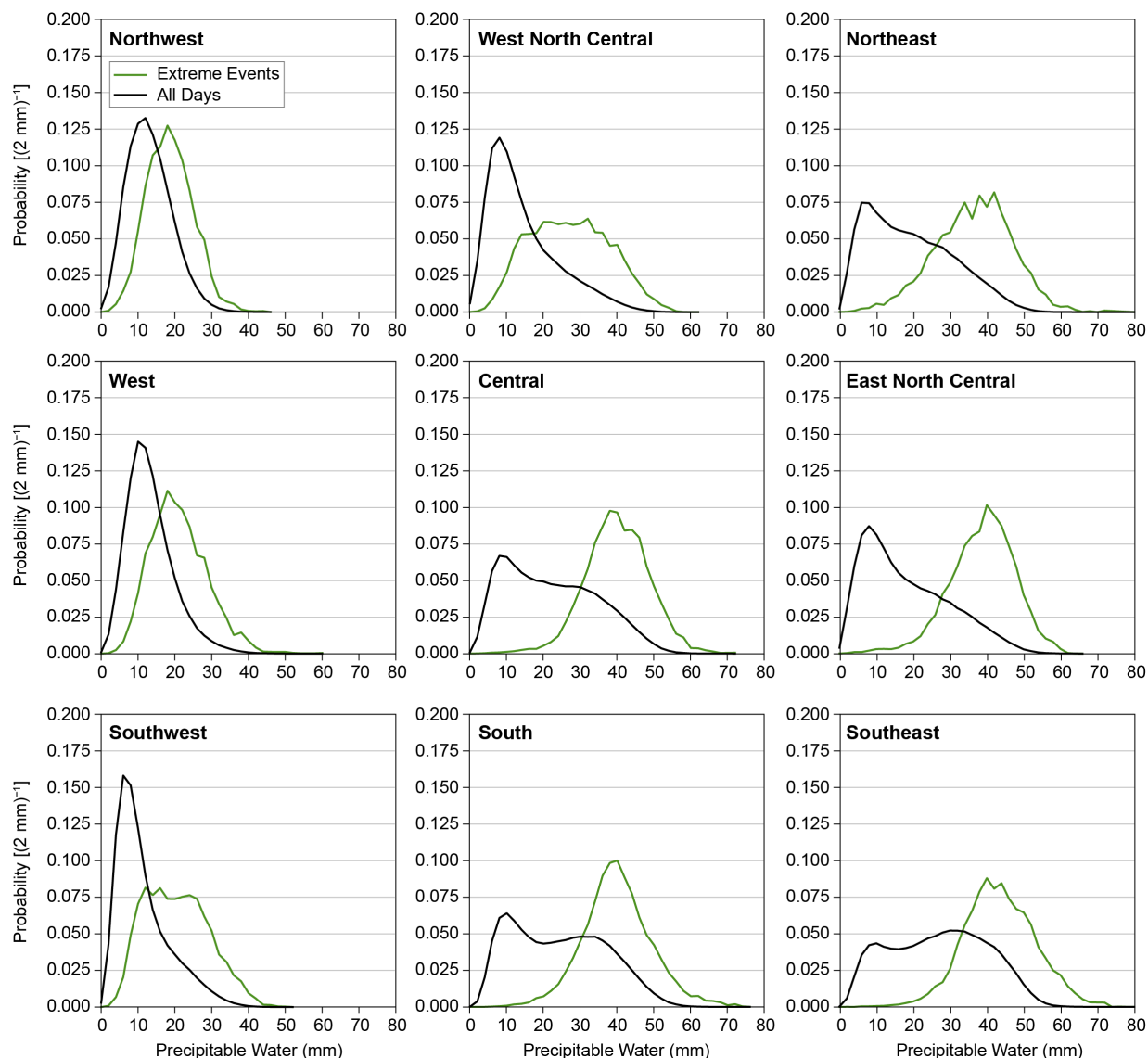


Figure 18. Annual fractional probability distribution of all days (black line) and days with an extreme (1-yr, 1-day recurrence) precipitation event (green line) vs. precipitable water (the 3-hr maximum during the day of the event) in 2 mm increments by NCEI climate region (from Kunkel et al. 2020a).

Of particular interest for eventual calibration of the CAUSES equation is whether there is strong evidence of temporal changes in PW across the U.S. as EP has increased. Indeed, the results depicted in Table 4 show the PW values associated with extreme events have increased in the eastern half of the U.S., where changes in EP have been most evident. Kunkel et al. (2020a) also show that this is robust regardless of the reanalysis used and that there are significant correlations between the trends of PW and EP during the 1949–2016 period of analysis.

Table 4. *Change in event-averaged maximum PW [(1992–2013) minus (1971–1991)] for four U.S. quadrants (center divisions 100°W and 38°N) and three recurrence levels for daily precipitation.*

	1-in-1-year events	1-in-5-year events	1-in-20-year events
Northeast	+2%	+2%	+5%
Southeast	+7%	+10%	+12%
Northwest	–2%	–1%	0%
Southwest	–3%	–6%	–7%

Concurrent positive relationships between EP and PW are well-reflected across the United States. The average PW is above average when EP events are also above average, using the annual maximum series (AMS; Table 5). Likewise, the average PW is below average when EP events are in the lower third of EP values.

Table 5. *Regional average PW values (expressed as standardized anomalies) for three tiers of years: the top third, middle third, and bottom third of the magnitude of daily maximum precipitation. The regions follow the NCEI definitions (see Figure 2), except that Central is an aggregate of the Northern Rockies and Plains, Upper Midwest, and Ohio Valley and South/Southeast is an aggregate of the South and Southeast.*

Region	Upper Tercile	Middle Tercile	Lower Tercile
Northwest	0.15	–0.02	–0.13
West	0.17	0.05	–0.22
Southwest	0.15	0.02	–0.17
Central	0.06	0.02	–0.08
South/Southeast	0.10	0.05	–0.15
Northeast	0.26	–0.05	–0.21

The regional variability of the relationship between EP events and the associated magnitudes of PW have also been explored by Kunkel et al. (2020a) using correlation analysis. They show that PW is strongly correlated with EP (Figure 19) across most of the United States. Over one-third of the stations across the U.S. have statistically significant correlations between the AMS value and the magnitude of PW. There are some notable exceptions in the intermontane area of the western third of the United States. This is apparent regardless of the reanalysis used.

Correlation: Annual Max Precip vs Precipitable Water

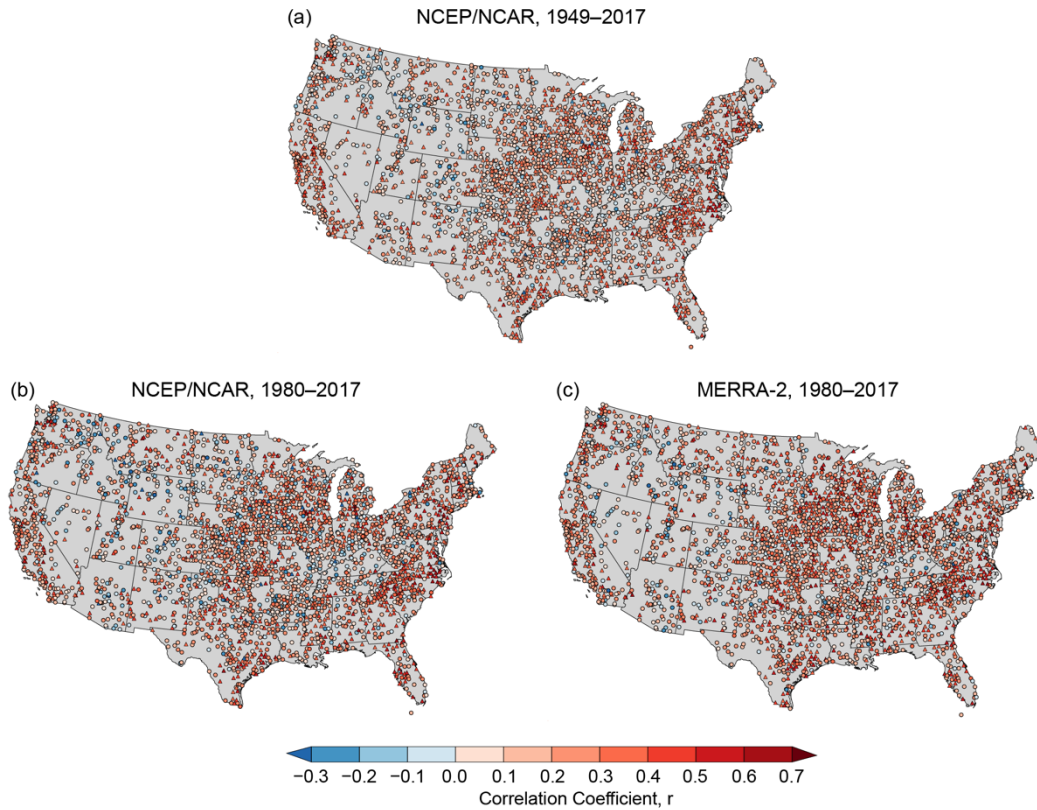


Figure 19. Correlation coefficients of AMS EP event magnitude vs PW for (a) NCEP/NCAR reanalysis for 1949–2017, (b) NCEP/NCAR reanalysis for 1980–2017, and (c) MERRA-2 reanalysis for 1980–2017.

As previously shown, there is a significant correlation between the trends of PW and EP across the U.S. (Kunkel et al. 2020b). Concurrent relationships are further explored (Kunkel et al. 2020a), and they reveal a strong positive relationship between PW and EP (Figure 20a). An important consideration in our work was to establish whether the relationship between PW and EP scaled differently with EP events at high versus low values of PW. At first approximation, this relationship scales linearly, but closer examination shows that is not the case. The ratio of EP/PW when plotted against PW (Figure 20b) shows that for a given amount of increase in PW, the increase in EP is greater at higher values of PW compared to lower values. Kunkel et al. (2020a) show that these differences are unlikely to be caused by chance. This non-linear scaling is an important consideration in the application of the CAUSES equation, because α then becomes dependent on the value of PW.

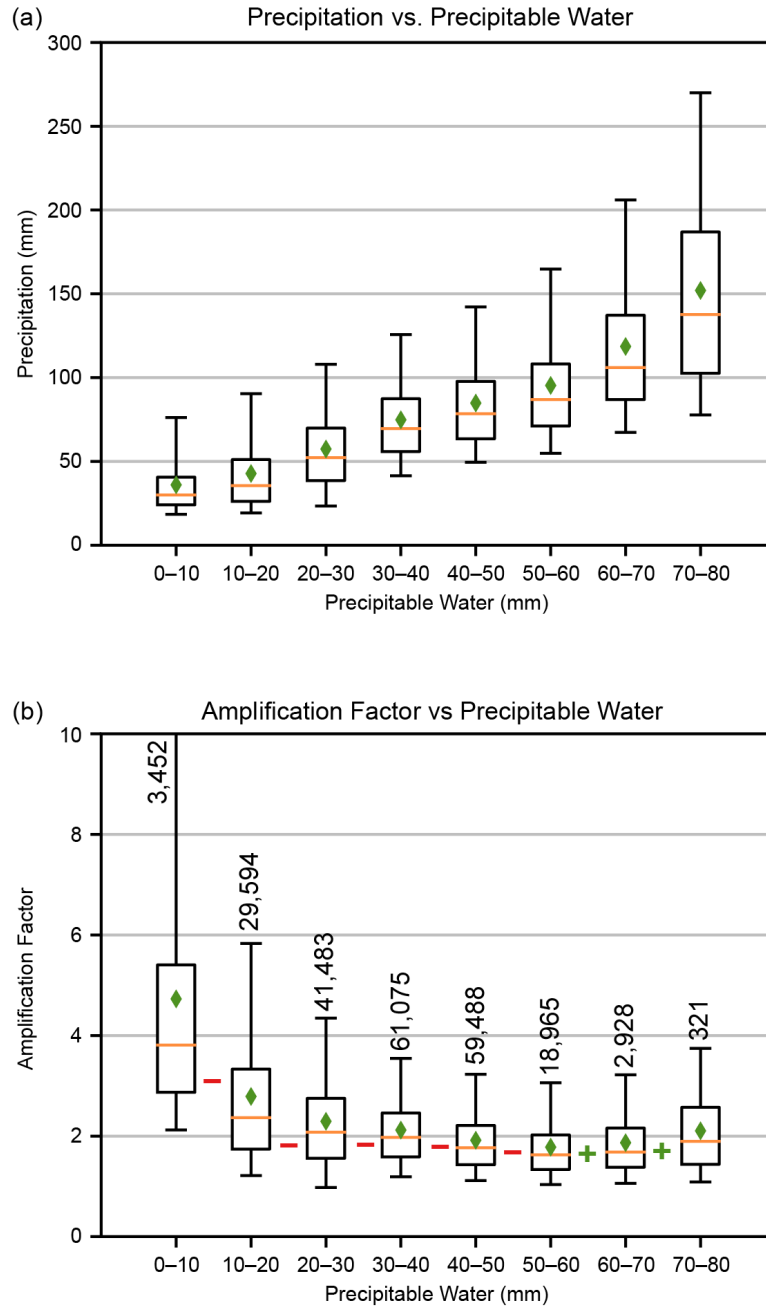


Figure 20. Boxplot distributions for the 1-yr, 1-day partial duration series of (a) precipitation event amount vs the same-day 3-hour maximum PW sorted into 10mm interval bins and (b) as in panel (a) but for the amplification factor A (EP/PW). Boxplot parameters include mean (green diamonds), median (orange horizontal lines), 25th and 75th percentiles (box limits), and 5th and 95th percentiles (whiskers). Statistical significance (0.05 level) of the difference between A across adjacent intervals of PW is denoted where “-” and “+” denote a significant decrease and increase, respectively (the value of A in the higher PW bin minus lower PW bin). The observation count in panel (b) used in the statistical tests is depicted above the top whisker, and the 95th percentile value for bin 0–10 is 10.75.

The data in Figure 20a form the basis for determining an appropriate function to represent the non-linear scaling of the coefficient α with PW. More than 3,000 stations across CONUS (Kunkel et al. 2020a) enable rather robust statistics. Using an interweaving method (to ensure stability), differentials of the observational averages from Figure 20a were calculated based on the change in EP with PW. The functional fit of the observations is shown in Figure 21 and, although it captures the non-linear behavior of α , end-point issues arise. This is reflected in equation (14), where the polynomial fit is bookended by fixed values of α . The polynomial fit between PW and α is given by:

$$\alpha(PW) = \begin{cases} 0.47 & PW < 25 \text{ mm} \\ 0.000577 PW^2 - 0.0272 PW + 0.794 & 25 \text{ mm} \geq PW \leq 65 \text{ mm} \\ 0.04781 (PW - 65) + 1.464 & 65 \text{ mm} > PW > 76 \text{ mm} \end{cases} \quad (14)$$

For $PW > 76$ mm, α is capped at 2.0

The ratio of EP amounts to coincident PW is defined as the amplification factor as displayed in Figure 20b. Note that it shows an amplification factor of about 2 over a sizable range of PW. Also note in the CAUSES equation that design values scale as a multiplicative factor. The parameter α indicates the rate of change of the amplification factor with PW. A value of 1 indicates that the amplification factor is constant. Since the amplification factor is about 2 over a sizable range of PW, this means that a value of $\alpha = 1$ implies that the change in precipitation design values is about two times as much as the increase in PW. For example, if $PW = 50$ mm, the average value of $EP = 100$ mm, and for future projections, if PW increases from 50 to 75, that is a 50% increase, or 1.5 adjustment factor from equation (3). Applying the 1.5 factor to the value of EP, we get a new EP of 150 mm. So, EP has increased by 50 mm in response to a PW increase of 25 mm. Note that α is capped at a value of 2 because we have few observations at such high values of PW. So instead, we base the values of α at those high levels on other work. For example, Nie et al. (2018) provide evidence for non-linear scaling of close to 2 at the highest values of PW in the set of modeling experiments they performed using a multi-day EP event in the southern United States.

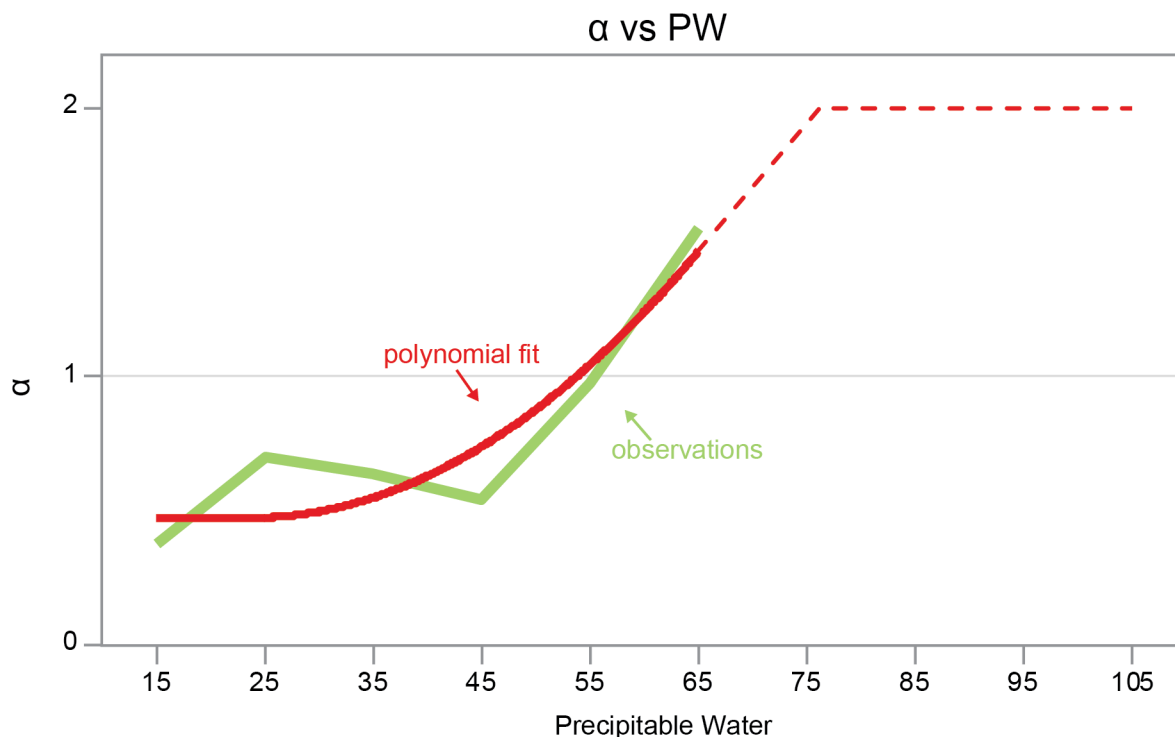


Figure 21. Observed and fitted relationship between PW and α . These are the values of α that are used in the CAUSES equation (3).

In addition to PW, we know synoptic weather types including fronts and extratropical cyclones (ETCs) play a role in EP intensity and frequency. Since these factors are also included in the CAUSES equation (3), it is useful to understand the extent to which any synergy with PW occurs during EP events. Since the vertical velocity $-\omega$ can represent both the rising motion of fronts and ETCs, it was used to better understand the interplay among EP, PW, and synoptic weather types. Simple correlation coefficients were used to quantify these interrelationships. Similar to the correlation coefficients calculated in Figure 19, the AMS from the 69 highest events for the set of stations derived from the Global Historical Climatology Network-Daily (GHCND) dataset were used to assess the correlation with $-\omega$ and PW. It is useful to understand the behavior at these high values, because we seek to discriminate between extreme Intensity-Duration-Frequency (IDF) values. These correlations can be different than what would be expected if the full set of precipitation measurements were used, because all these values are extreme. Because the subset focused on here are the highest EP events, this already implies that substantial PW and/or $-\omega$ must have occurred.

Results shown in Figure 22a reveal large areas with negative correlations between EP and $-\omega$ and relatively few (less than 10%) statistically significant positive correlations. It is noteworthy that there are many stations with inverse relationships between PW and $-\omega$ (Figure 22b); much of the U.S. east of the Cascades and Sierra Nevada has negative correlations. As a result, only 3% of the stations have simultaneous statistically significant positive correlations between both EP and PW and EP and $-\omega$ (Table 6). The large areas with negative correlations of PW vs. $-\omega$ in southeastern regions, where PW is largest, suggest that thermodynamic, rather than dynamic, effects are driving the non-linear behavior at the highest values of EP and PW. Extreme values of PW and $-\omega$ are often not in synchrony when considering the most extreme EP

events. This is further supported by the mixed set of positive and negative correlations when the ratio of EP/PW (**A**) is correlated with $-\omega$ (Figure 22c). Taken together, these results provide strong evidence that PW is often the dominant factor related to EP intensity, given at least modest values of vertical velocity.

Table 6. Percent of all stations with statistically significant (0.05 two-tailed t-test) correlations between the specified variables.

	EP vs PW Significant	EP vs PW Not Significant	Total
EP vs $-\omega$ Significant	3.4	5.6	9.1
EP vs $-\omega$ Not Significant	31.3	59.6	90.9
Total	34.7	65.2	100.0

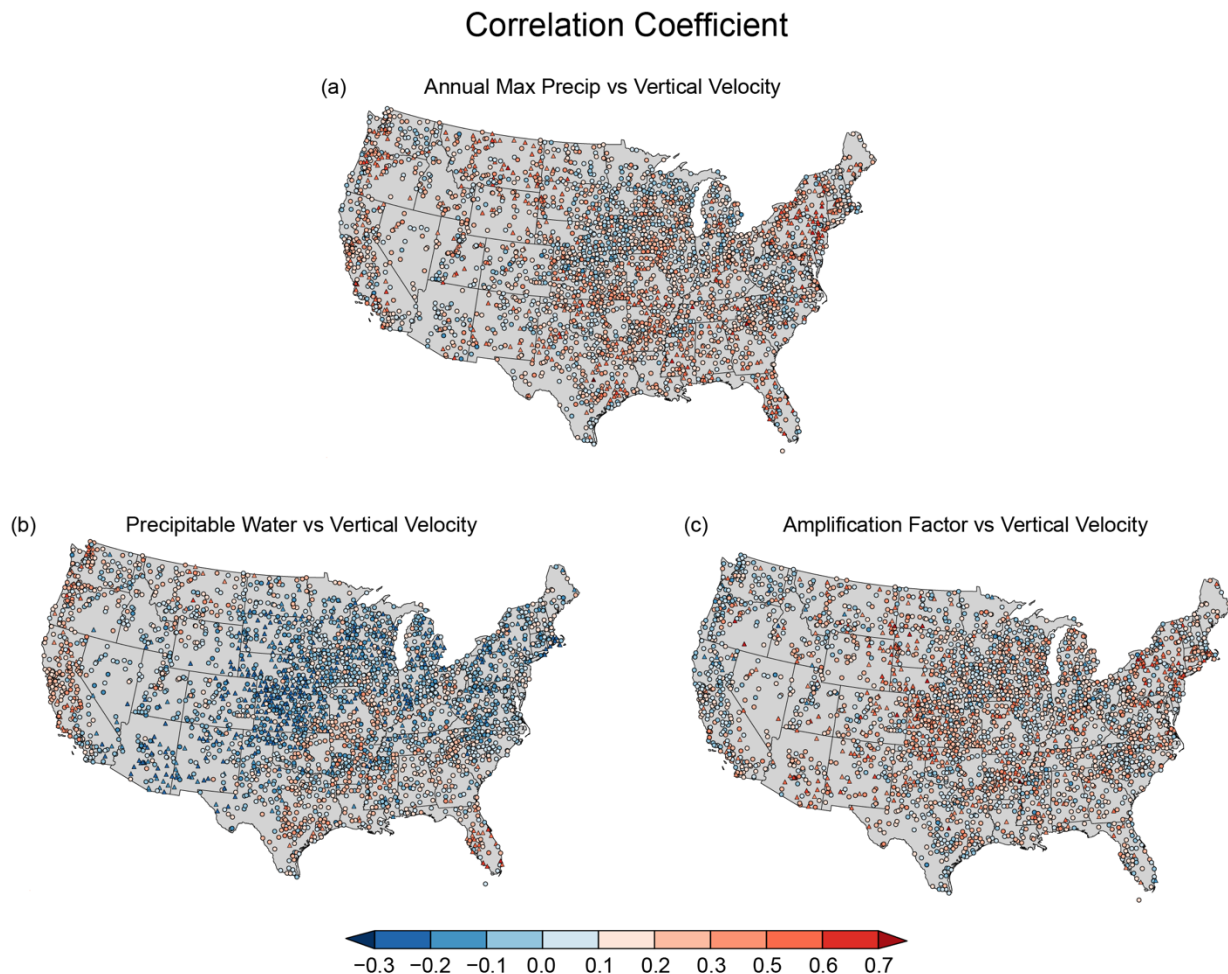


Figure 22. Correlation coefficients for the annual maximum series of (a) EP event magnitude with $-\omega$, (b) PW with $-\omega$, and (c) A with $-\omega$. PW and $-\omega$ are the simultaneous day's 3-hr maximum precipitable water and 3-hr maximum vertical velocity, respectively. Triangles indicate statistically significant (0.05 level) correlations.

It is also useful to discern any differences in seasonality of the PW and EP relationships needed for the precipitation CAUSES equation. Figure 23 depicts strong seasonality of these trends for the warmer months of the year in the eastern half of the U.S., especially during autumn in the Southeast. PW is at its highest values during these warmer months (Kunkel et al. 2020a). This is consistent with the larger increases in EP in these regions during autumn in the Southeast and during the warmer months of the year in the Northeast.

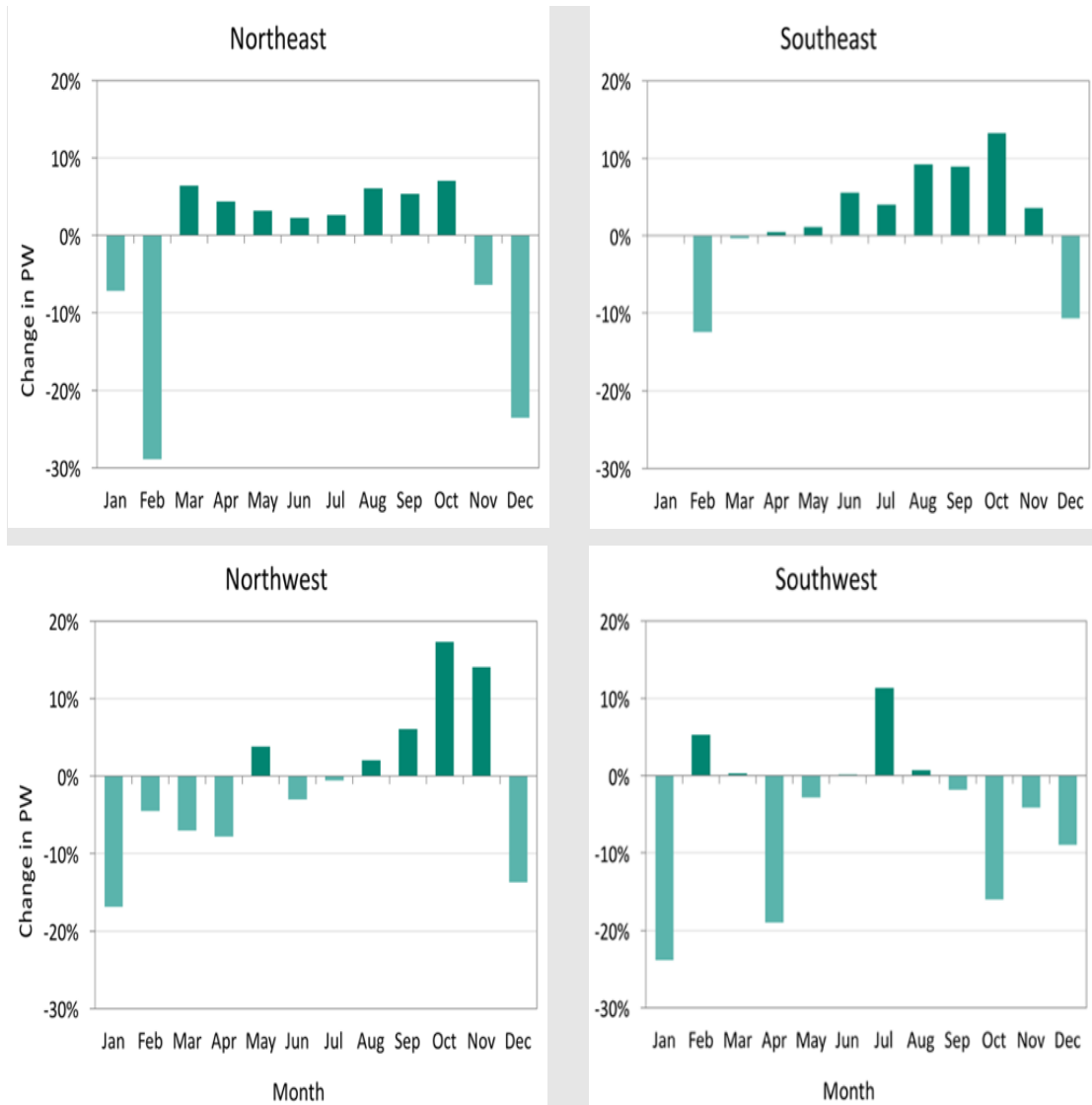


Figure 23. *Percentage changes in precipitable water by month for daily extreme precipitation events with a 1-in-5-year recurrence for four quadrants of the United States.*

The seasonality of PW and EP is also evident in the values of **A**. The value of **A** is higher in the cold season (Nov. through Apr.) compared to the warm season (May through Oct.) almost everywhere (Figure 24), pointing to the importance of organized dynamical weather systems ($-\omega$) helping to produce EP events when PW is comparatively low (e.g., in colder conditions; Kunkel et al. 2020a). This is also indirect evidence that atmospheric overturning is important, as the organized dynamical systems can enhance long-range and sustained transport of water vapor over longer times. The high relative values of **A** in the Sierra Nevadas, Cascades, and extreme Southern Appalachian Mountains during both cold and warm seasons (Figure 24a,b) are consistent with the notion that the dynamics of generally weaker warm-season synoptic-scale systems can also be strongly enhanced by abrupt orographic changes.

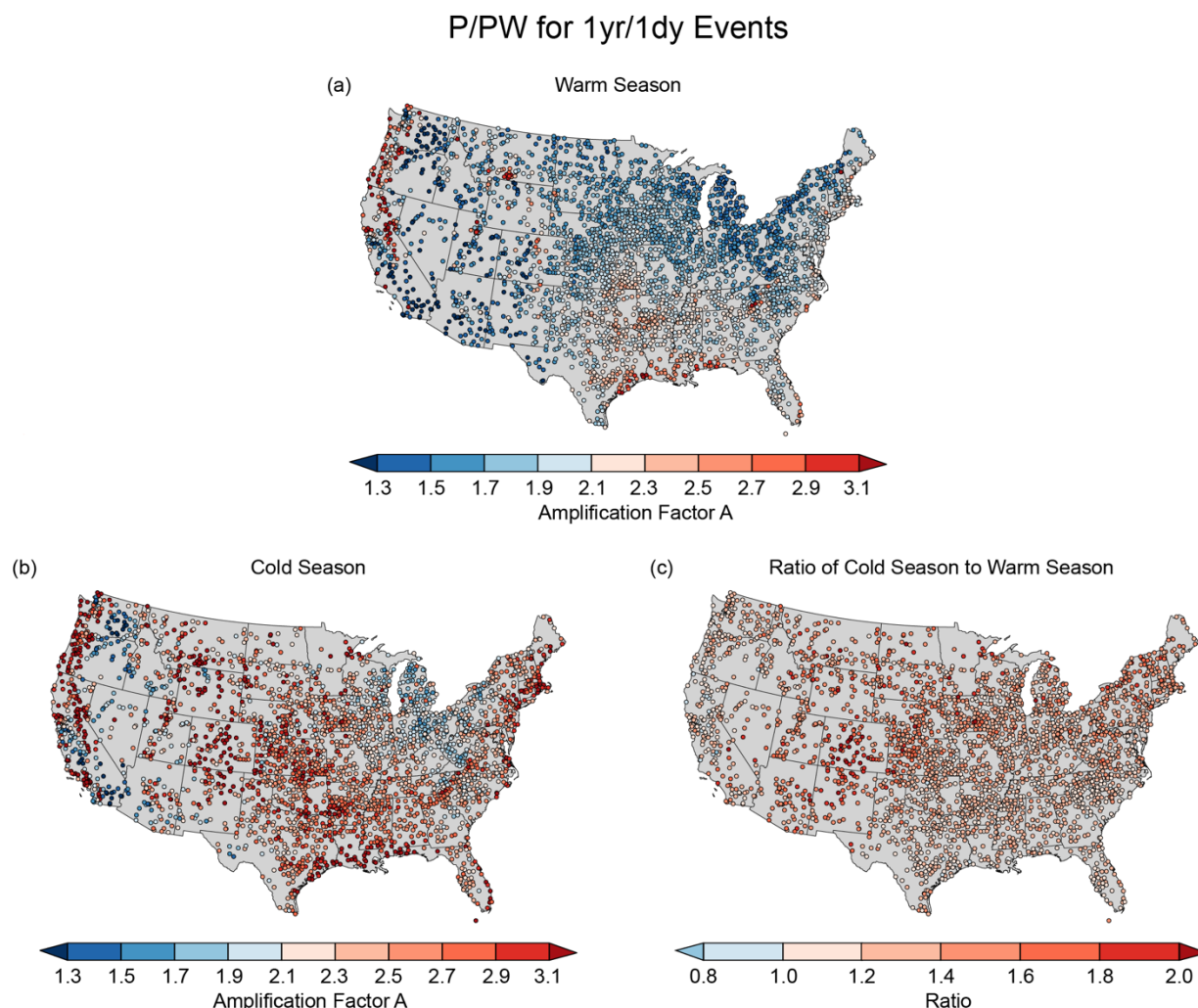


Figure 24. Average amplification factor (A) for each station for precipitation events exceeding the 1-yr, 1-day threshold for (a) warm season, (b) cold season, and (c) cold-to-warm season ratio of A .

The relatively large warm-season values of A along and near the Gulf and Atlantic coastlines (Figure 24a), where tropical cyclones can be strong, suggest that those dynamical systems might also play an important role in enhancing A , despite the uncertainty in future frequency of these weather events. The large number of cold-to-warm season ratios of A exceeding 1 (Figure 24c) clearly shows that the dynamics in the cold season contribute significantly more to EP events compared to warm-season dynamics when PW is high. This points to the importance of seasonality in the CAUSES equation.

Summer Fronts

Past work (Kunkel et al. 2012) has shown that EP events are closely tied to fronts of all types. Using the dataset produced by Kunkel et al. (2012), we performed a number of climatological analyses on frontal occurrences. This dataset includes causes for daily, 1-in-5-yr events occurring during 1908–2013. The largest single seasonal cause of extreme precipitation

events is summer fronts. For this reason, an in-depth analysis of this sub-category of events was undertaken.

The 5 largest daily precipitation events for each station were extracted from this dataset. This approximately represents events that exceed the threshold for a 1-in-20-yr recurrence interval. The percentage of these largest events caused by fronts was calculated for each station. These percentages are displayed in Figure 25. At many stations in the eastern half of the U.S., all such events are caused by fronts. These results emphasize the importance of fronts for this study.

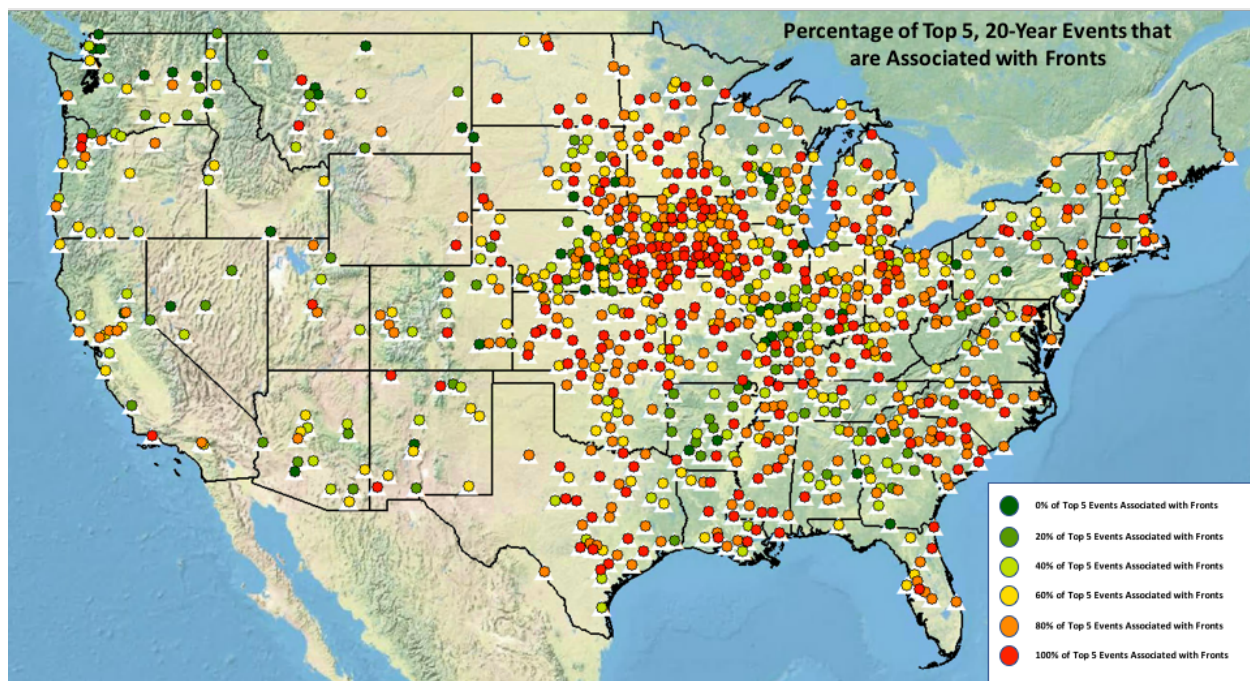


Figure 25. Percentage of the five largest daily precipitation events that are caused by fronts. The period of analysis is 1908–2013.

Weather Systems

The master dataset of EP events and associated meteorological causes was analyzed to determine the distribution by meteorological cause for each $10^{\circ} \times 10^{\circ}$ grid box. The results for 1-day duration events exceeding the 1-yr recurrence level threshold are shown in Figure 26. Fronts are the dominant cause in every box except for the north-central box, where ETC events occur slightly more often than frontal events. Extratropical cyclones are the 2nd most common cause in every other box except for the Florida peninsula, where tropical cyclones (TCs) are the 2nd most common cause. In addition to the Florida peninsula, TCs cause more than 10% of events in south Texas, the south Atlantic coastal area, and the Northeast. The monsoon is responsible for more than 10% of events in the desert Southwest grid box.

These results are qualitatively similar to those of Kunkel et al. (2012). The percentage of frontal events found here is somewhat higher. However, Kunkel et al. (2012) analyzed rarer events, those exceeding the 5-yr recurrence level threshold. Also, the automated methodology used herein differs from the manual effort in Kunkel et al. (2012).

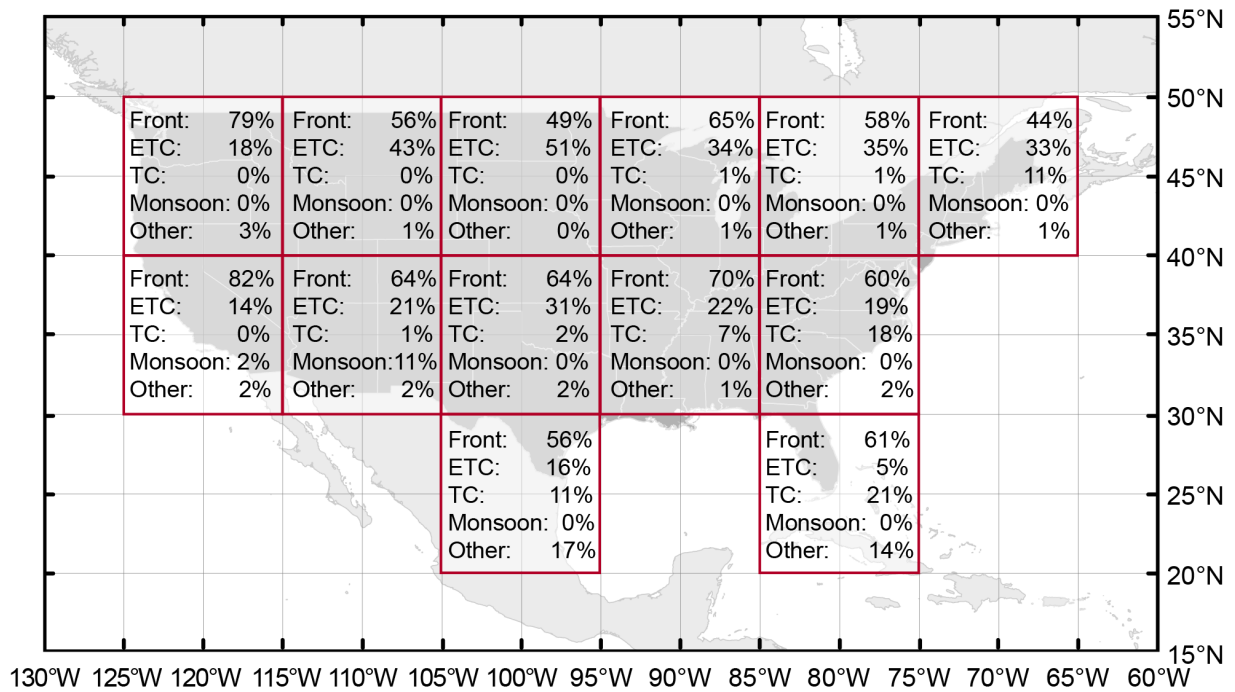


Figure 26. Percentages of meteorological causes for 1-day duration extreme precipitation events for each 10°×10° grid box for 1980–2017.

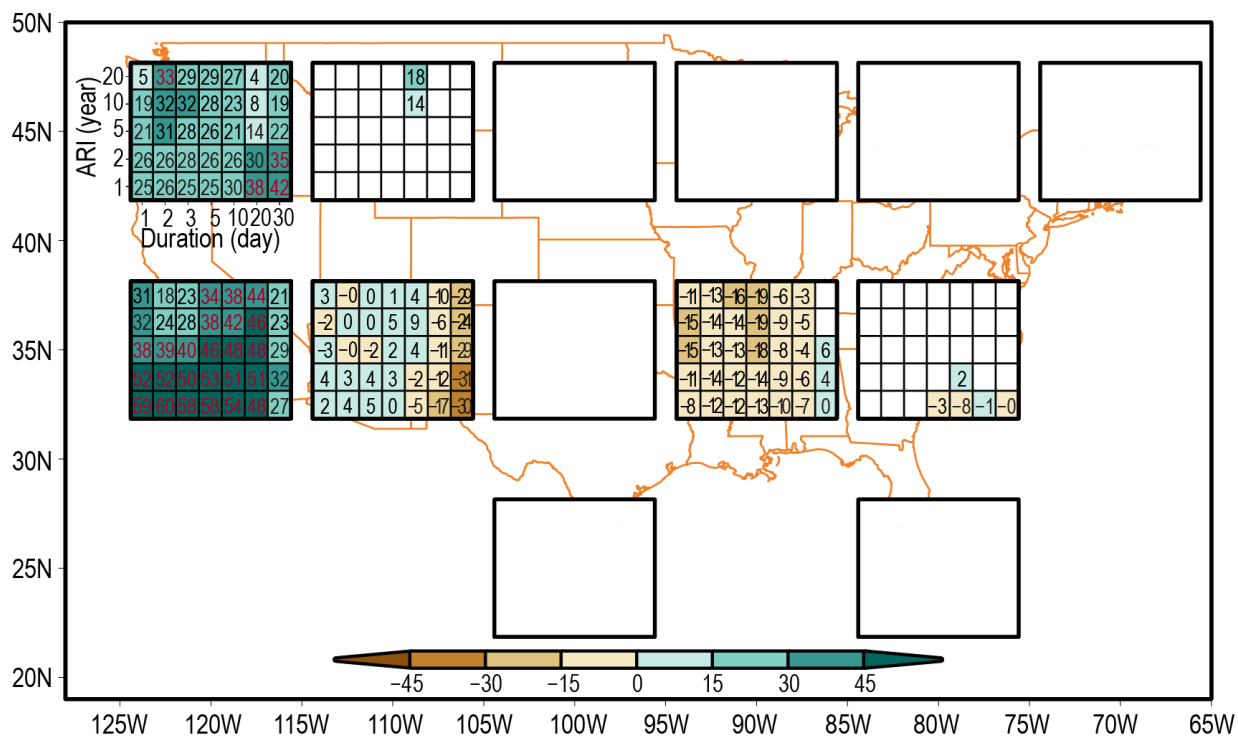
Time series of fronts and ETCs from the master dataset were also used to determine the average seasonal exposure to each cause within a grid box. The number of exposures within each grid box was paired with the average seasonal number of extreme events over the same grid box. This resulted in two pairwise time series—one of extreme events and frontal passages, and one of extreme events and ETC counts—over the entire 38-year period. A linear correlation was then calculated from these time series in each season for both meteorological cause types. Results were then broken down by return period and duration (Figures 27 and 28).

The relationship between frontal passages and extreme event occurrence (Figure 27) varies both geographically and by season. Numerous statistically significant positive correlations are found in the westernmost regions (regions 1 and 7; refer to Figure 3 for region numbers) for winter; the far Southwest, southern Ohio Valley, and Southeast (regions 7, 10, and 11) for spring; the Midwest and portions of the South (regions 4, 5, and 10) for summer; and the Midwest, Southwest, and Texas (regions 5, 8, 10, and 12) for fall. In most cases, stronger relationships are seen for shorter return periods, with less variation over the range of durations. Consistent statistically significant negative correlations were found only for portions of the Northwest and south-central U.S. (regions 2 and 9) in spring. For ETCs (Figure 28), the strongest relationships in spring are found in the northwestern plains (region 2) across all return periods and durations and for longer return periods in the southern Ohio Valley/Southeast (region 10). Statistically significant positive correlations are also found in the Northern Plains (regions 2 and 3) in summer and the Northeast (region 6) in fall. No statistically significant negative correlations are seen for ETCs.

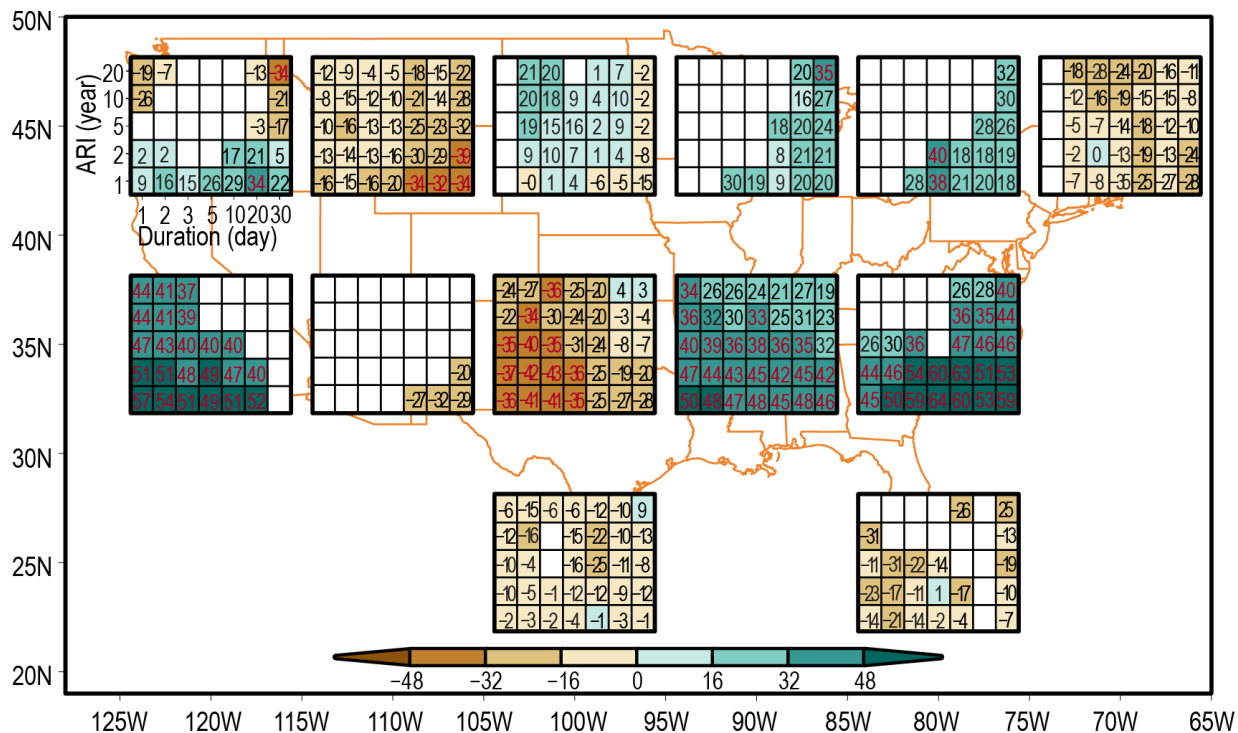
The lack of strong correlations for either fronts or ETCs in some regions and seasons most likely relates to the features of this analysis and the role of water vapor. In this project (Kunkel et al. 2020a), we found that water vapor is the most important factor modulating the

intensity of EP events. We also found (in unpublished work) that most of the EP events defined herein occur in a small fraction of weather systems, and likely those where high moisture content is coincident with weather system occurrence. The co-varying relationship between weather systems and water vapor is likely to be primary in explaining variability on the short inter-seasonal timescales investigated here, and much of the variability is likely to be statistical noise because most systems do not cause extreme events. However, the research of Kunkel et al. (2012), which is supported in the present work (see Figure 26), indicates that the dynamical forcing of organized weather systems, specifically fronts, ETCs, and TCs, is an essential component causing extreme precipitation events. On the multi-decadal timescales that underlie IDF value estimation, the frequency of such systems will determine the opportunities for extreme events.

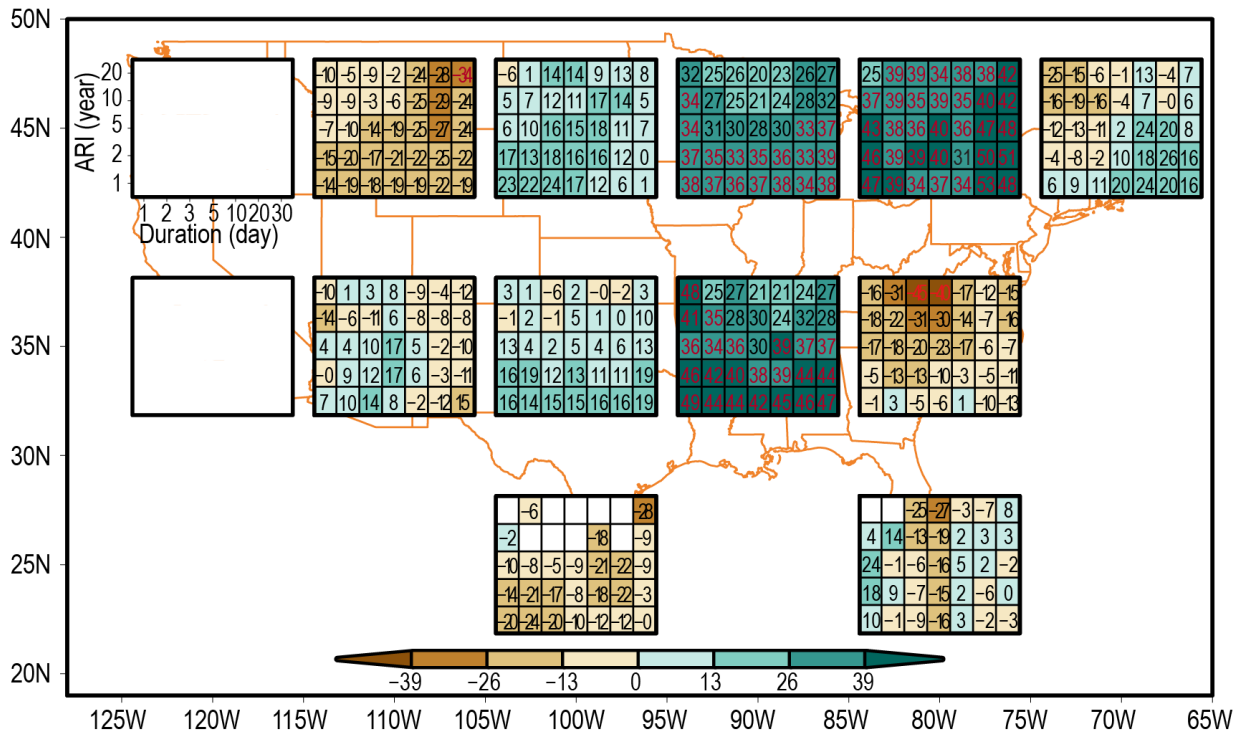
a) Front Correlations, Winter



b) Front Correlations, Spring



c) Front Correlations, Summer



d) Front Correlations, Fall

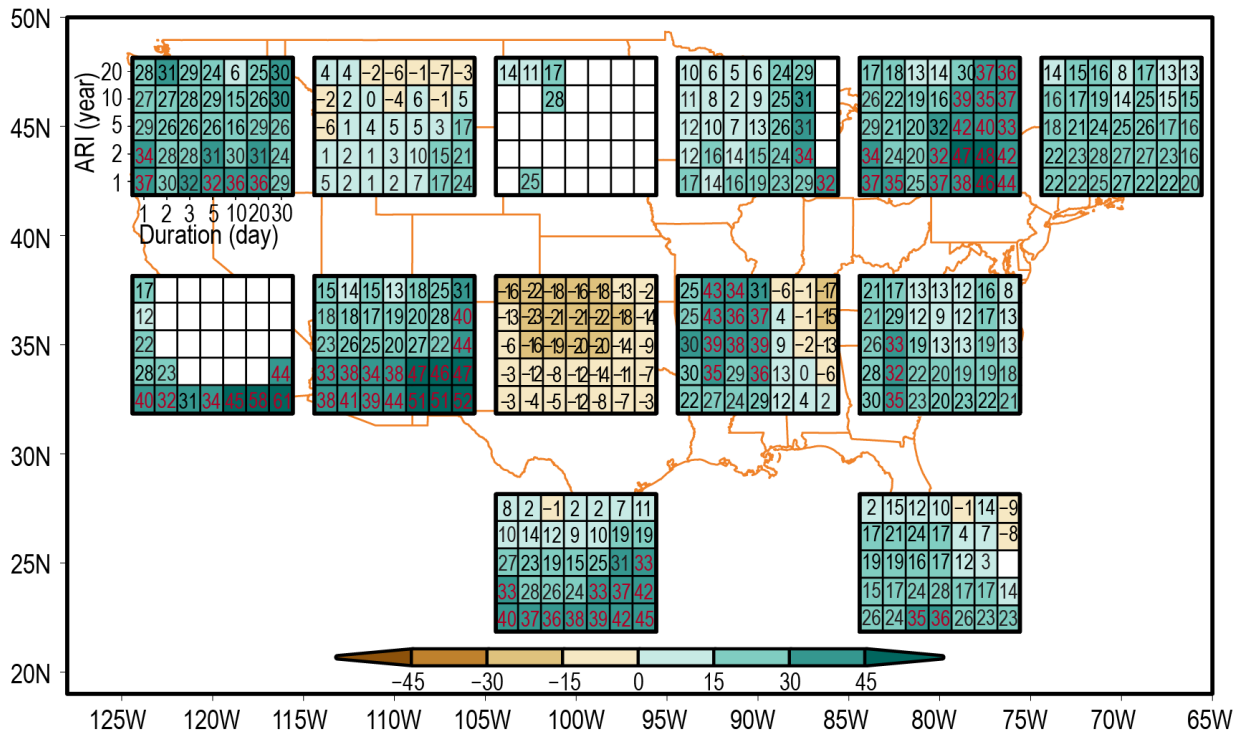
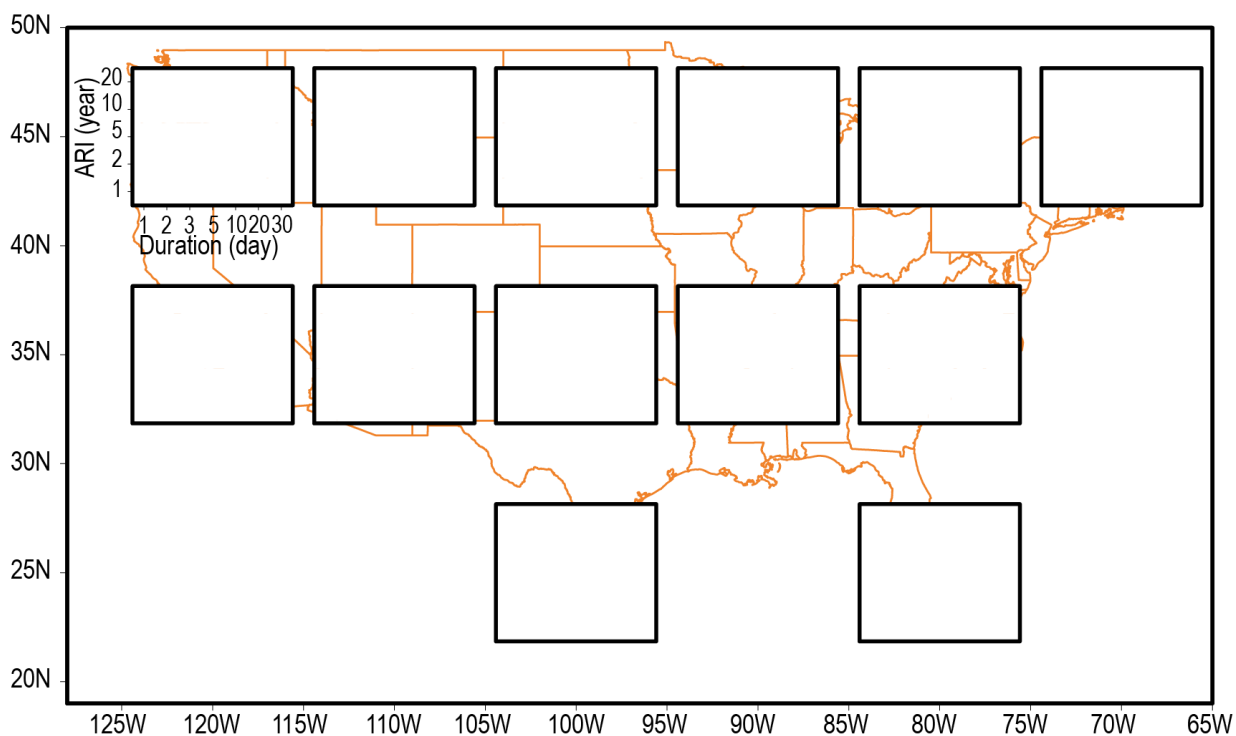


Figure 27. Seasonal correlations between the occurrence of extreme events and the incidence of frontal passages for a) winter (DJF), b) spring (MAM), c) summer (JJA), and d) fall (SON). Data

tables containing correlation coefficients for each return interval/duration pair are shown for each $10^{\circ} \times 10^{\circ}$ degree grid box. Values are multiplied by 100 (e.g., a correlation coefficient of 0.23 is represented as 23). Rows indicate values for a return period of (from bottom to top) 1, 2, 5, 10, and 20 years. Columns indicate values for durations of (from left to right) 1, 2, 3, 5, 10, 20, and 30 days. Brown shades depict negative correlations, and teal shades depict positive correlations. Correlation coefficients displayed in red indicate a statistically significant correlation ($p < 0.05$). Values are masked out if the number of events in that grid cell and season are less than 10% of the total number of events for all seasons. If all return period/duration pairs are masked out, the entire data table is blank.

a) Extratropical Cyclone Correlations, Winter



b) Extratropical Cyclone Correlations, Spring

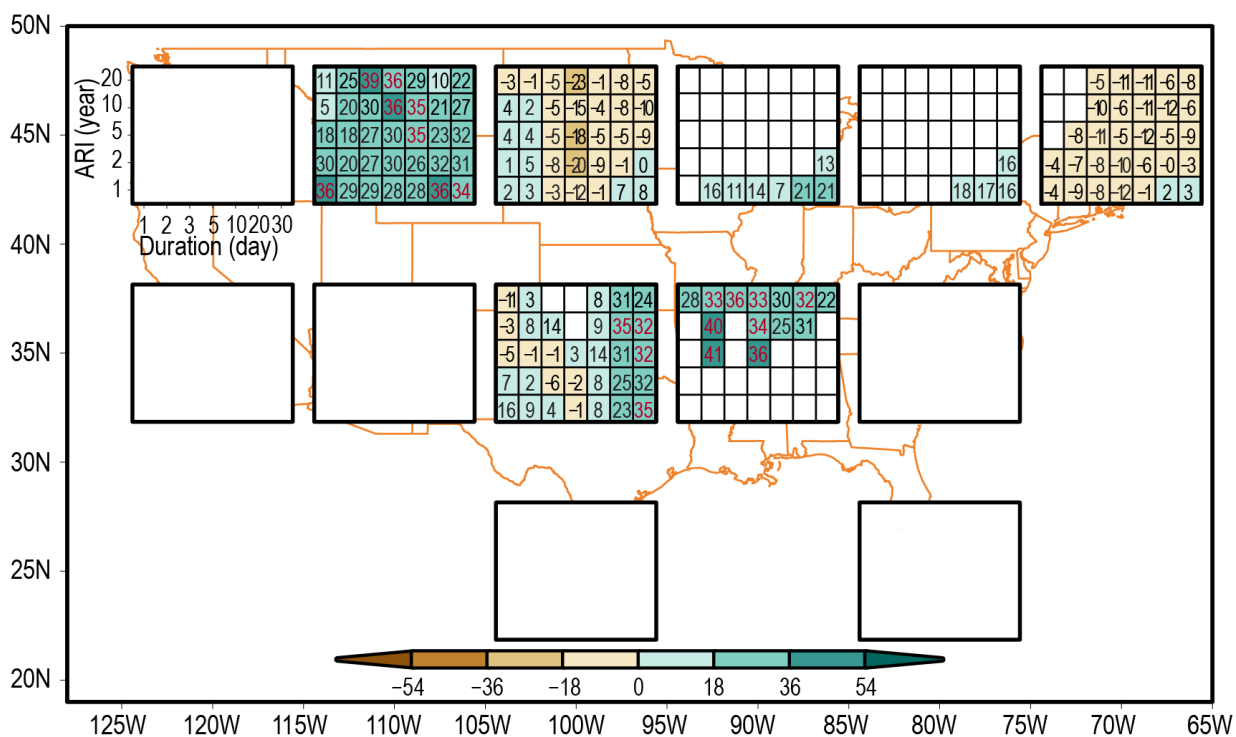


Figure 1 is a map of the North Pacific region, showing the spatial distribution of ARI (ARI) and its duration. The map covers latitudes from 20N to 50N and longitudes from 125W to 65W. A color bar at the bottom indicates ARI values from -42 to 42. The map is divided into several rectangular regions, some of which contain numerical data. The data is organized into a grid where the vertical axis represents ARI (year) and the horizontal axis represents Duration (day).

The ARI (year) values are shown in the following grid:

ARI (year)	1	2	3	5	10	20	30
20	27	32	36	29			
15	28	36	35	33			
10	26	35	36	30	33		
5	19	26	30	33	30		
2	25	21	24	27	28		
1							

The Duration (day) values are shown in the following grid:

Duration (day)	1	2	3	5	10	20	30
20	30	29	27	30	28	10	15
15	34	32	29	25	28	14	16
10	32	40	27	24	30	15	15
5	29	31	27	24	25	14	17
2	28	29	27	22	25	18	24
1							

Figure 1 is a map of the North Pacific region, showing the spatial distribution of ARI (ARI1) for different durations (1, 2, 3, 5, 10, 20, 30 days). The map covers latitudes from 20N to 50N and longitudes from 125W to 65W. A color bar at the bottom indicates ARI values from -39 to 39. The map shows various rectangular regions, some of which are filled with a grid of colored squares representing ARI values for different durations. The color scale ranges from -39 (dark blue) to 39 (dark red), with 0 being white.

64

fall (SON). Data tables containing correlation coefficients for each return interval/duration pair are shown for each $10^\circ \times 10^\circ$ degree grid box. Values are multiplied by 100 (e.g., a correlation coefficient of 0.23 is represented as 23). Rows indicate values for a return period of (from bottom to top) 1, 2, 5, 10, and 20 years. Columns indicate values for durations of (from left to right) 1, 2, 3, 5, 10, 20, and 30 days. Brown shades depict negative correlations, and teal shades depict positive correlations. Correlation coefficients displayed in red indicate a statistically significant correlation ($p \leq 0.05$). Values are masked out if the number of events in that grid cell and season are less than 10% of the total number of events for all seasons.

Extratropical Cyclones

We examined the ETC characteristics associated with daily EP events exceeding a 1-yr ARI, specifically the minimum central pressure and the average speed of movement. This was compared to the distribution of all ETCs. For all ETCs (Figure 29), the frequency is concentrated in the range of $5\text{--}20\text{ m s}^{-1}$ and $985\text{--}1005\text{ mb}$, with a peak frequency around 992 mb and 10 m s^{-1} . For those ETCs associated with EP events (Figure 30), the distribution is shifted toward higher pressures and slower speeds, with the peak frequency around 1002 mb and 5 m s^{-1} . Slower-moving systems favor greater precipitation accumulations. There is a seasonal dependence, where higher summer water vapor concentrations favor the occurrence of extreme precipitation ETC events even though summer ETCs are on average weaker than those during other seasons.

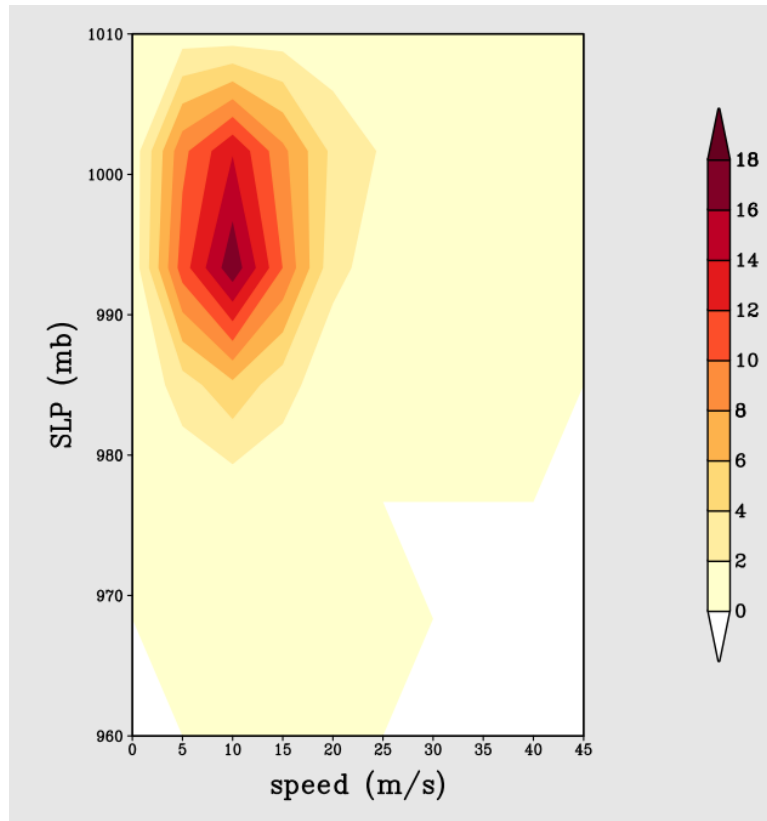


Figure 29. Percentage of ETCs over CONUS by minimum sea level pressure and average speed of movement during 1980–2016 (from NCEP/NCAR reanalysis).

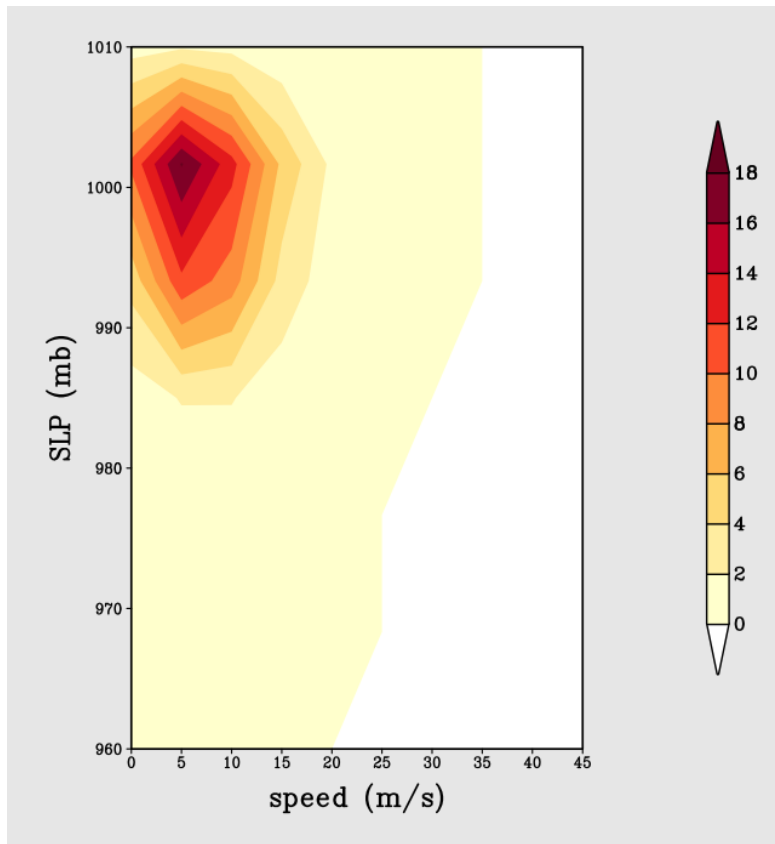


Figure 30. Percentage of ETCs that caused a daily 1-yr recurrence event somewhere over CONUS by minimum sea level pressure and average speed of movement during 1980–2016 (from NCEP/NCAR reanalysis).

North American Monsoon

The results of the moisture flux convergence (MFC) analysis (Table 7) indicate that the mean value of the convergence term (CT) is comparable to that of MFC, and the value of the advection term (ADV) is much smaller. Among the 50 extreme precipitation events, 28 and 25 events are associated with positive values of the ADV over Arizona and New Mexico, respectively. There was only one extreme event where ADV is stronger than the CT for both Arizona and New Mexico. Thus, extreme precipitation in the monsoon season is associated with flow convergence.

Table 7. Moisture flux convergence terms ($10^{-5} g K g^{-1} s^{-1}$) for 50 extreme summer precipitation events in Arizona and New Mexico.

	MFC	CT	ADV
Arizona	−6.544	−6.796	0.252
New Mexico	−6.871	−6.528	−0.343

The probability density function (PDF) of MFC for extreme precipitation events exhibits a distinct shift toward the larger values of convergence compared with the PDF for non-extreme precipitation events. This result is similar for both station precipitation extremes and state-level precipitation extremes. An analysis of moisture flux associated with extreme events in Arizona and New Mexico associated with the summer monsoon found good correspondence between the timing of extreme precipitation events and large values of MFC. Figure 31 shows the distribution of moisture divergence at 700 hPa for all monsoon season days and days representing the highest 51 precipitation events in New Mexico and the highest 51 events in Arizona (averaged over the states). Nearly all of the biggest events have positive values of low-level moisture convergence (negative values of divergence). By comparison, the climatological distribution is centered around zero, with the distribution skewed toward positive values of divergence. This indicates that low-level convergence is a suitable metric for identifying extreme event conditions in climate models.

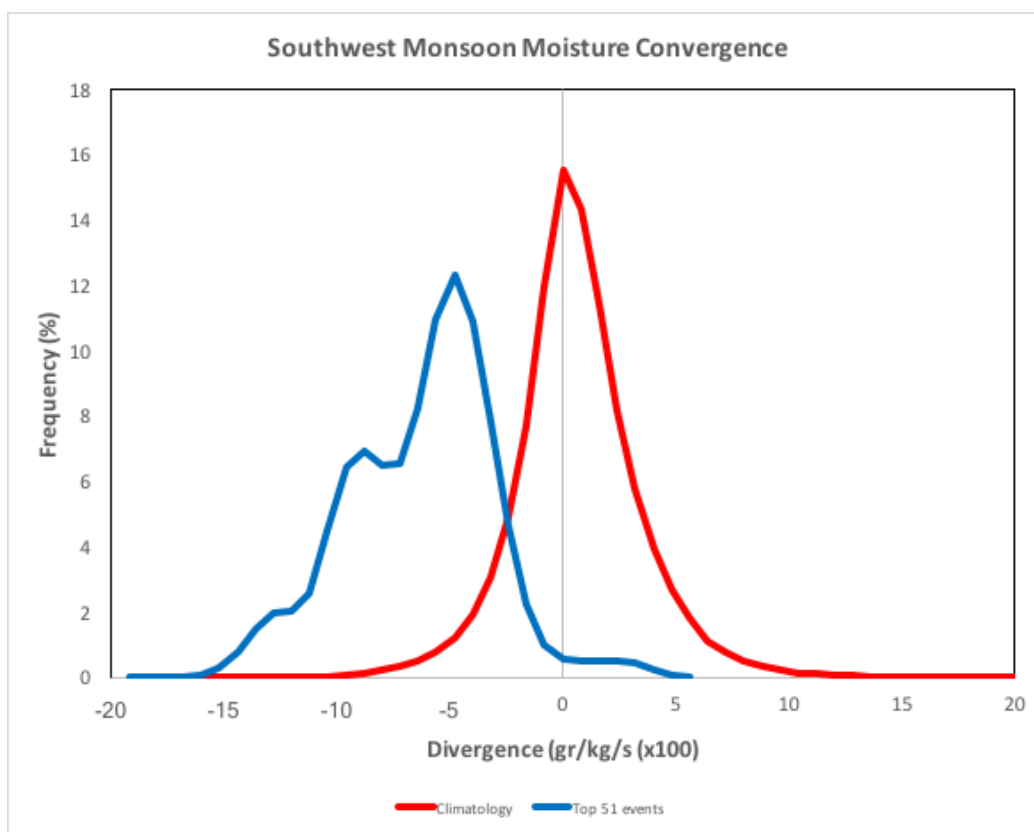


Figure 31. Frequency distribution functions for moisture divergence at the vertical pressure level of 700 hPa for the months of June, July, August, and September for the states of Arizona and New Mexico for the period 1979–2013. The red line is the climatological distribution, including all days. The blue line is the distribution for the days with the highest state-wide average precipitation. This includes the top 51 events for Arizona and the top 51 events for New Mexico.

Task 4: Perform extensive analyses of CMIP5 model simulations, identifying the occurrence of weather systems causing heavy precipitation for historical and future simulations.

Precipitation

The Localized Constructed Analogs (LOCA) dataset is a new statistically downscaled dataset for CONUS. This dataset includes daily precipitation data for 31 CMIP5 models covering the period 1950–2100. Spatial resolution is 1/16th degree. We performed generalized extreme value (GEV) analysis on the annual maximum series of 1-day, 5-day, 10-day, 20-day, and 30-day precipitation totals for four 30-yr periods (1976–2005, 2006–2035, 2036–2065, and 2070–2099) to estimate future changes in various return-period amounts. A representative selection of results of the projected changes is illustrated in Figure 32. This figure shows changes for 2070–2099 relative to 1976–2005 under the RCP8.5 (high) emissions scenario averaged over the 10°×10° grid boxes. Values are provided for the 5-yr and 100-yr return levels and the 24-hr and 30-day durations. Generally, the percentage changes are higher for the 100-yr return level than the 5-yr return level. Also, changes are higher for the 24-hr duration than the 30-day duration. Changes are also generally larger in near-coastal areas, with the exception of the Florida peninsula.

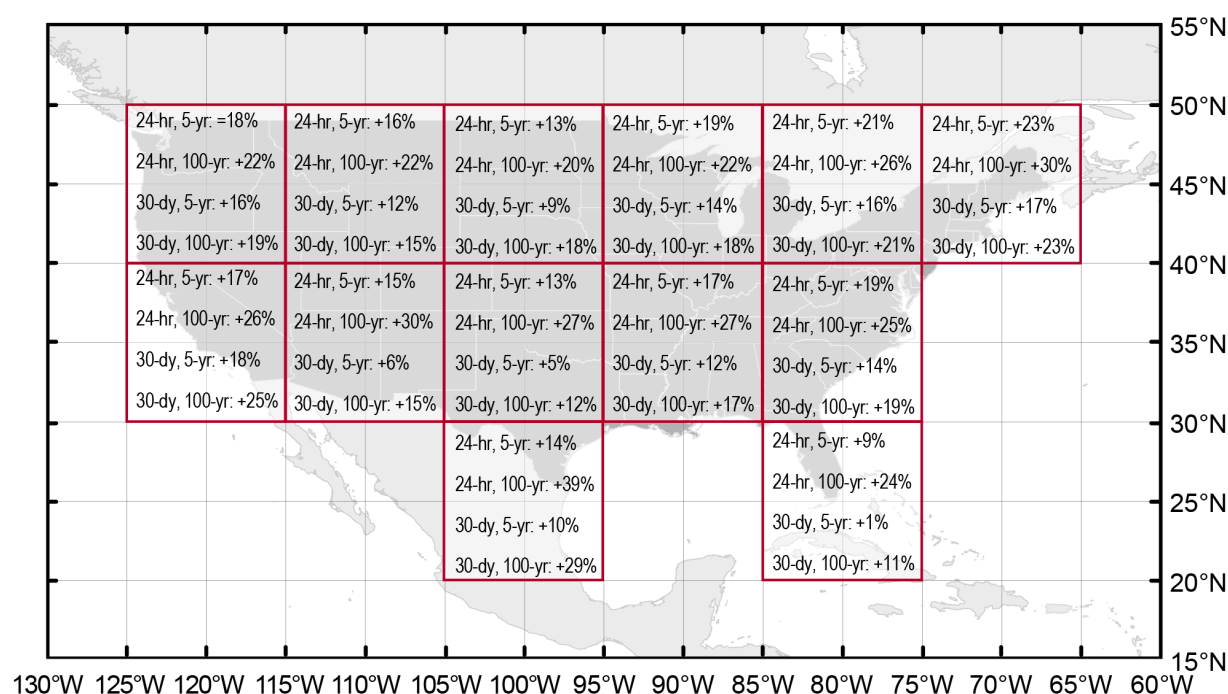


Figure 32. Projected change in the 5-yr and 100-yr return period amounts for 24-hr and 30-day precipitation for 2070–2099 relative to 1976–2005 under the RCP8.5 emissions scenarios using the LOCA downscaled data.

Results for other durations and return levels follow similar patterns. Figure 33 shows the changes in the daily 100-yr return level for each grid point. There is considerable point-to-point variability in the values, but this is simply sampling noise associated with the small number of extreme values used for the GEV fit. At larger scales, the changes are very uniform across the U.S., with values steadily increasing through the 21st century.

The following conclusions are derived from this GEV analysis:

- The future changes in return-period threshold values increase with return period, 100-yr changes being greater than 5-yr changes.
- The future changes increase substantially with increased greenhouse gas forcing.
- The future changes are very large by the end of the century under the RCP8.5 scenario.
- The large-scale (averages over $10^{\circ} \times 10^{\circ}$ grid boxes) spatial variability is relatively small compared to the magnitude of the changes by the mid- to late 21st century.
- Future changes generally decrease slightly with increasing duration.

Projected change (%) in daily, 100-year Precipitation Design Value

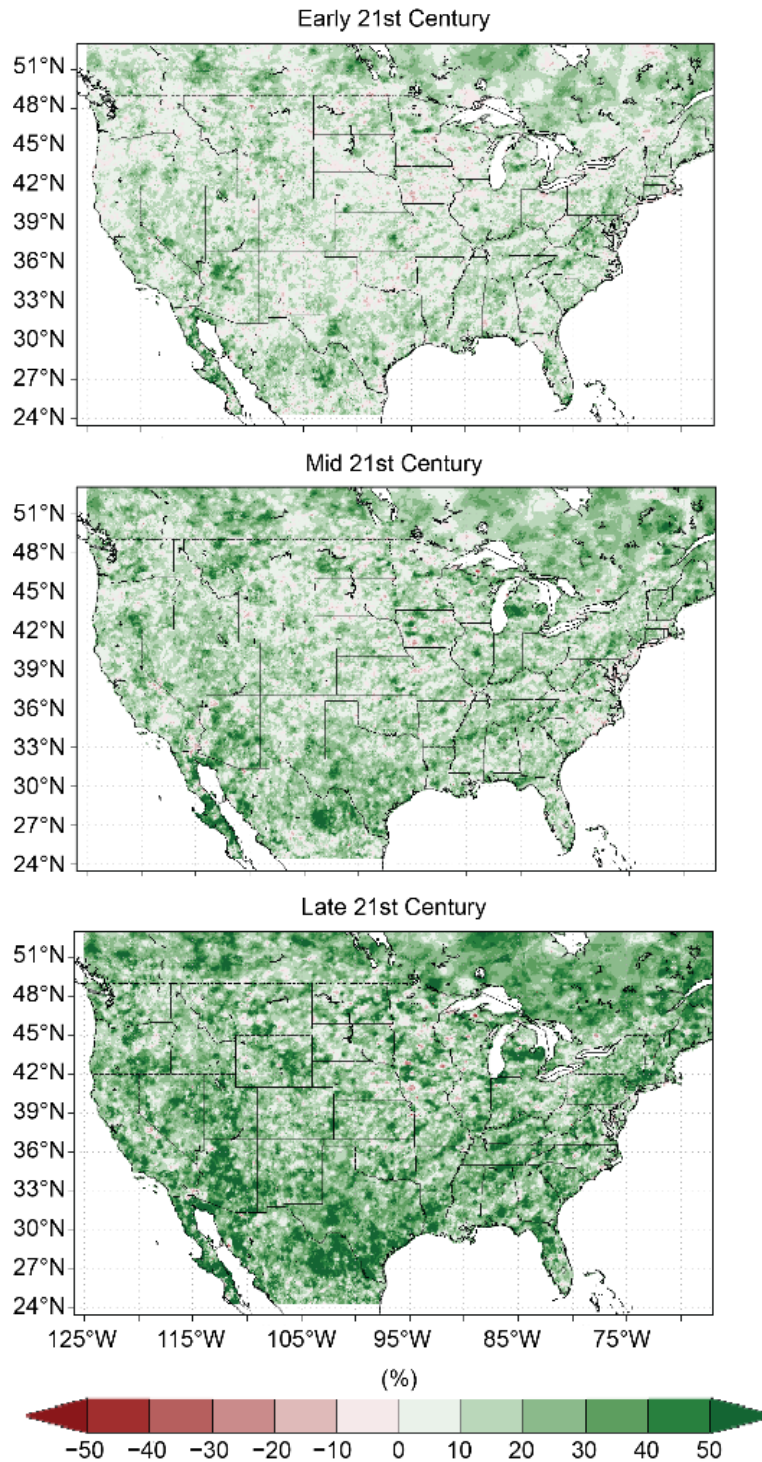


Figure 33. RCP8.5 5-day extreme precipitation totals for the 100-year return interval for the early 21st century, mid-21st century, and late 21st century.

North American Monsoon

We found that the high MFC conditions associated with EP occurrence are usually triggered by larger-scale weather patterns. This was investigated using the NCEP/NCAR reanalysis dataset for the New Mexico EP events. Our analysis found that summer extreme daily precipitation events in New Mexico were attributed to ETCs (62%), westward expansion of the North Atlantic Subtropical High (NASH; 28%), and TCs (10%). The same analysis was applied to the CMIP5 (historical simulation) data for the same period and indicates that the ETCs, NASH, and TCs account for 53%, 37%, and 10%, respectively, in rather good agreement with observations. This suggests that large-scale patterns in the CMIP5 models can be used to indicate favorable conditions for monsoon extreme precipitation events.

An analysis of CMIP5 models indicates that MFC occurs with increased frequency in the future under increasing greenhouse gas concentrations (Figure 34). The biggest increases in frequency are with the largest values of moisture convergence. A further analysis found that the increases in MFC are due primarily to increases in the amount of water vapor in these situations, rather than increases in total mass convergence.

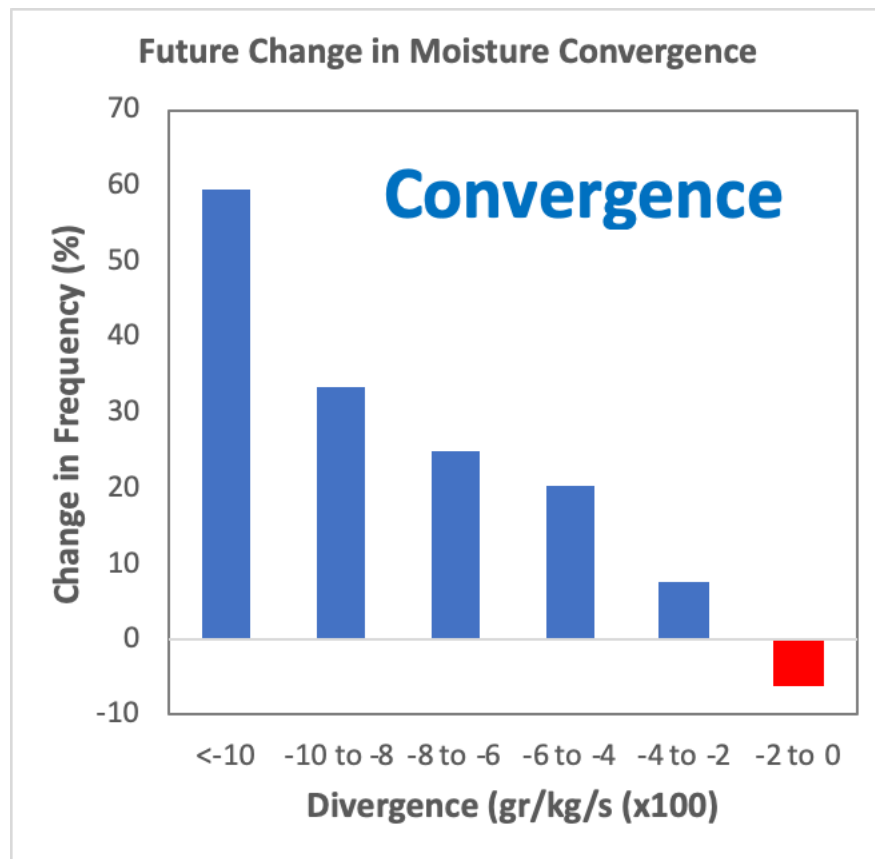


Figure 34. Future changes (%) in the frequency of moisture flux convergence. These are averages for 13 CMIP5 models.

Water Vapor

A set of maps displaying future changes in global water vapor were created. The maps represent water vapor changes for each decade of the 21st century from the 2020s to the 2080s

for two emissions scenarios, RCP4.5 and RCP8.5. An example is shown in Figure 35. Some key characteristics of these maps:

- The changes in water vapor are upward for all locations globally.
- By the end of the 21st century under a high emissions scenario, the changes are very large, exceeding 20% everywhere and exceeding 30% over most of the mid- and high latitudes.
- The spatial variability is relatively small in comparison to the changes by the mid- and late 21st century. For example, the changes over CONUS for the end of the 21st century under the RCP8.5 scenario vary by only 5–10%.

The standard deviation among models (not shown) is a sizable fraction of the mean change, although all models show substantial increases in water vapor. This variation among models is due to the differing sensitivity of the models (i.e., how much global warming is simulated for a given amount of greenhouse gas increase).

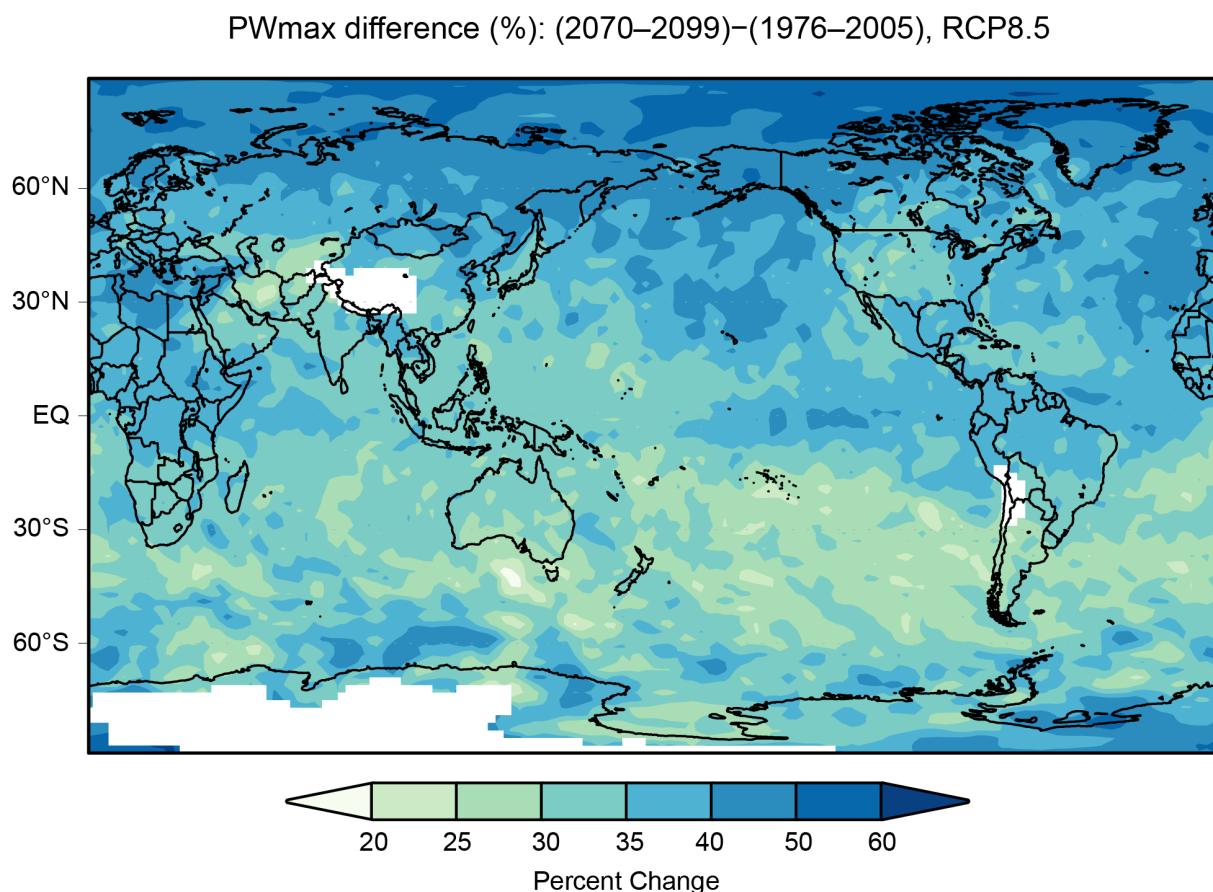


Figure 35. Projected change (%) in maximum daily precipitable water (PW_{max}) by late 21st century relative to late 20th century under the high (RCP8.5) emissions scenario. This is an average of 13 CMIP5 models.

Fronts

Analysis of future changes in the frequency of fronts was completed for 4 CMIP6 models and the CAM5 simulations. For the CMIP6 model results, the future changes were averaged over the rolling 30-yr periods centered on 2025, 2035, 2045, 2055, 2635, 2075, and 2085. Since the CAM5 simulations are for fixed global warming levels, they do not naturally fit within this 21st century chronology. To incorporate these results with the other model results, the CMIP5 models were used to determine the multi-model mean temperature changes under the RCP4.5 and RCP8.5 emissions scenarios for 2025, 2035, 2045, 2055, 2065, 2075, and 2085, relative to the year 2000 (the center point of our base period for the CMIP6 model analysis). This temperature change was compared to the CAM5 simulation warming levels of 1.5°C, 2.0°C, and 3.0°C. This determined which CAM5 simulation to use for each 30-yr future period. Furthermore, the amount of warming was used to determine a scaling factor to adjust the CAM5 results. This scaling factor is based on the assumption that the local changes in frontal frequency are linearly dependent on the amount of warming. As an example, assume that the CAM5 HAPPI15 simulation shows a change in frontal frequency of –10% in grid box #10. For the year 2045, the multi-model mean global warming is 1.0°C, compared to the HAPPI15 warming of 1.5°C, or a ratio of 0.67. Thus, the actual frontal frequency change assigned to grid box #10 for year 2045 is –6.7%.

Table 8 shows the CAM5 simulations used for each future period along with the scaling factor used.

Table 8. The CAM5 simulation assigned to each future period. The scaling factor is also shown.

Time (Center of 30-yr period)	RCP4.5	RCP8.5
2025	HAPPI15 (0.6°C; scaling factor = 0.4)	HAPPI15 (0.7°C; SF = 0.47)
2035	HAPPI15 (0.8°C; SF = 0.53)	HAPPI15 (1.0°C; SF=0.67)
2045	HAPPI15 (1.0°C; SF = 0.67)	HAPPI15 (1.4°C; SF = 0.93)
2055	HAPPI15 (1.3°C; SF = 0.87)	HAPPI20 (1.9°C; SF = 0.95)
2065	HAPPI15 (1.4°C; SF = 0.93)	HAPPI20 (2.4°C; SF = 1.20)
2075	HAPPI15 (1.6°C; SF = 1.07)	UnHAPPI30 (2.8°C; SF = 0.93)
2085	HAPPI15 (1.6°C; SF = 1.07)	UnHAPPI30 (3.4°C; SF = 1.13)

Figure 36 shows multi-model mean summer season results for the RCP8.5 scenario by the end of the 21st century for the 10°×10° grid boxes. Decreases in frontal frequency are projected for western and southern regions. Little change is projected for much of the north. This behavior is consistent with a northward shift of the mid-latitude jet stream during the summer.

Future Change in Fronts Frequency, multi-model average,
high emissions scenario, 2070-2099, Summer

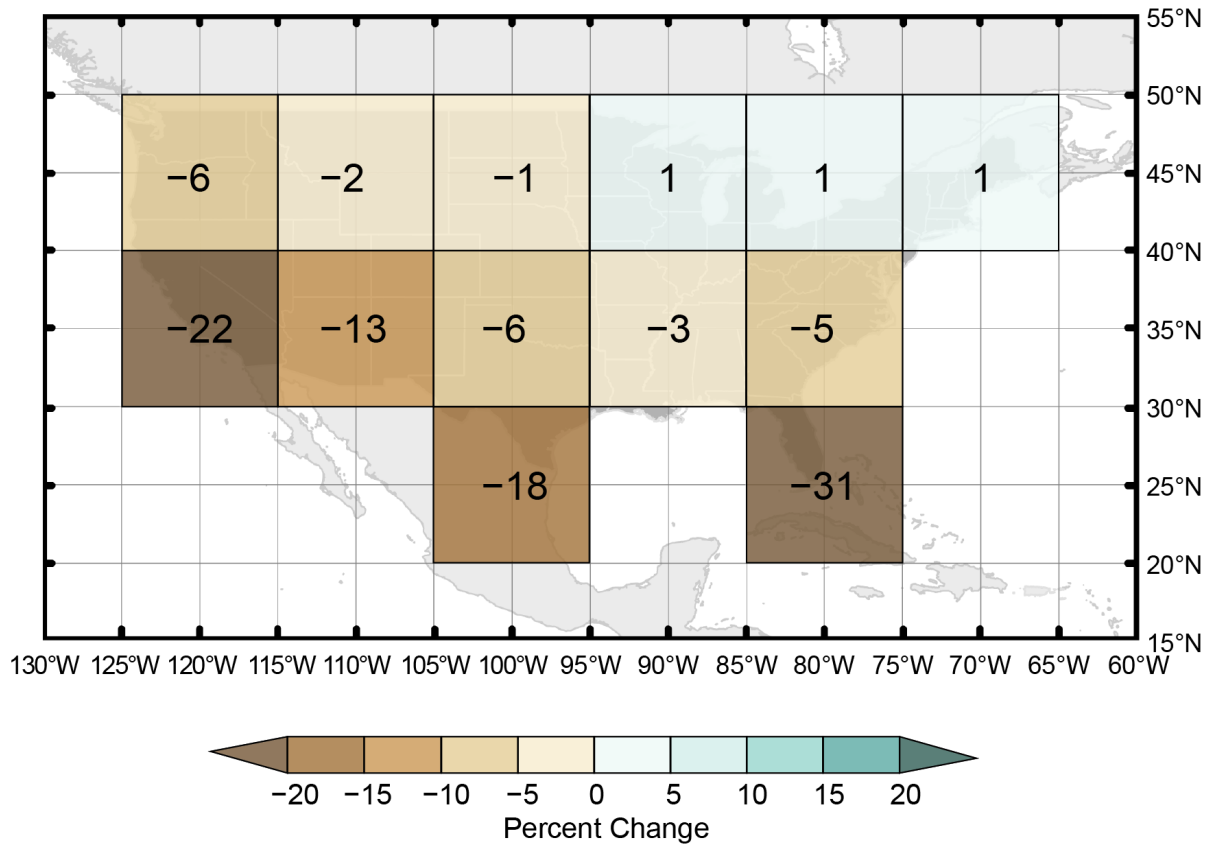


Figure 36. Change (%) in the frequency of fronts during 2070–2099 (relative to 1985–2015) under the high emissions scenario (RCP8.5) from an ensemble of 5 global climate models. Decreases are projected across the southern and western United States. The changes are small for the northern United States.

Extratropical Cyclones

Analysis of future changes in the frequency of ETCs was completed for 23 CMIP5 models. Results for 2070–2099 under the high emissions scenario (RCP8.5) are shown in Figure 37. In all seasons, there are decreases in a majority of the grid boxes. The decreases are most widespread in the summer and fall, especially in the northern United States.

Future Change in Extratropical Cyclone Frequency, high emissions scenario, 2070–2099

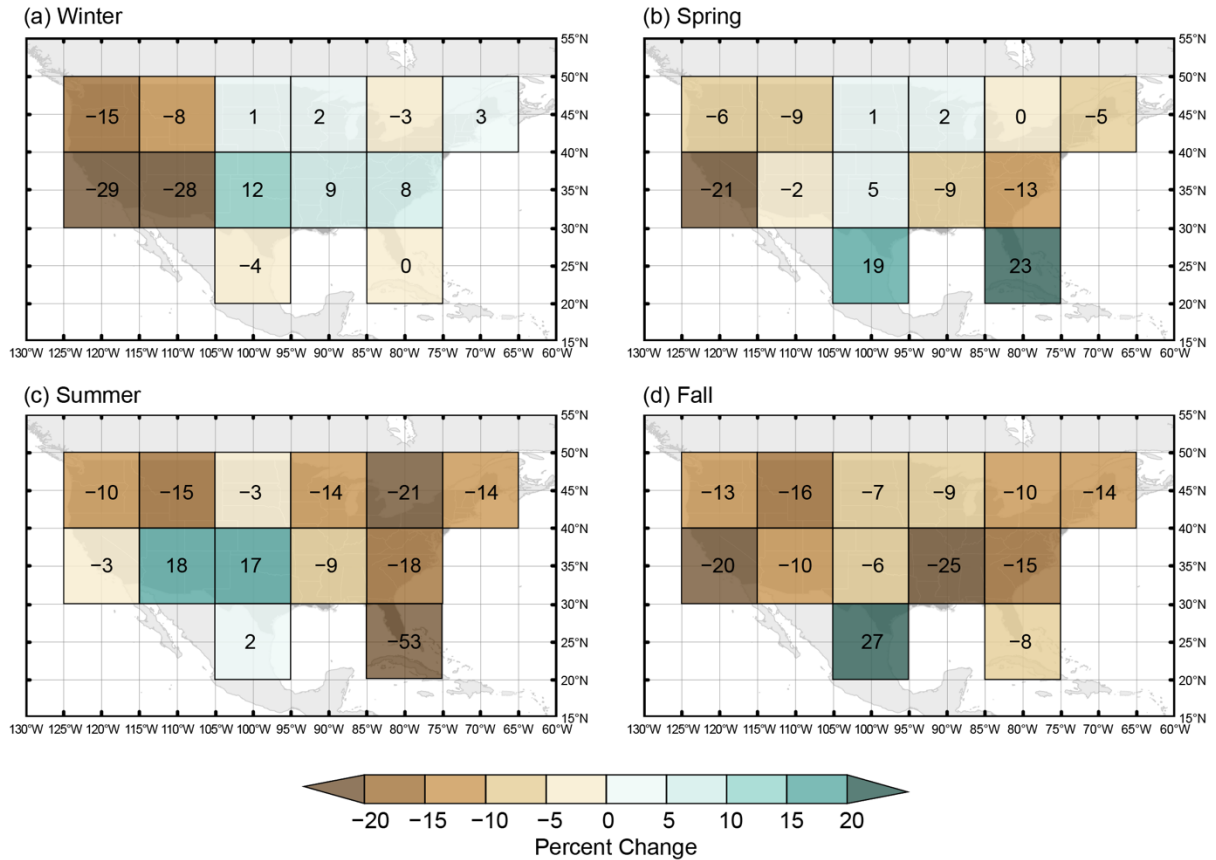


Figure 37. Future change (%) in the number of ETCs for 2070–2099 under the high emissions scenario (RCP8.5). These are averages of 23 CMIP5 models.

Task 5: Determine the meteorological causes and trends of heavy precipitation events at global military installation sites identified by DoD.

Figure 38 shows the results for the historical meteorological analysis identifying the meteorological causes of extreme precipitation events for each region. Examination of Figure 38 reveals some interesting patterns. In Central Alaska, most events occur in the summer (JJA), with fronts and ETCs being the main meteorological cause. In Southern Alaska there is a similar pattern in the summer; however, the activity carries into the fall, with nearly as many heavy events in the fall as in summer. Hawai‘i shows a winter peak in the number of heavy events mainly caused by fronts and ETCs. A secondary peak in the number of events occurs in the fall, again with fronts and ETCs being the main two causes. This is interesting given Hawai‘i’s location in the subtropics. Hawai‘i is impacted in the cold season by fronts and ETCs called “Kona Lows,” which are cold-core cyclones more typical of higher latitudes (Otkin and Martin 2004). Lastly, Guam has a nearly identical maximum in heavy events in the summer and fall, with TCs accounting for the most number of heavy events followed by air mass convection.

The last analysis was to use climate model simulations to calculate the change in the 30-yr maximum daily precipitable water vapor (PW) for future periods and the future changes in the meteorological causes for each of the regions. Climate model simulations from the CMIP5

archive were used to produce multi-model average 30-yr maximum daily values of PW and the multi-model standard deviations for each season at each location for seven overlapping 30-year blocks (e.g., 2011–2040, 2021–2050, etc.) in the future using both the RCP8.5 and RCP4.5 emissions scenarios. An example for one season (DJF) for Hawai‘i using the RCP8.5 emissions scenario is shown in Table 9. Results for all seasons for both emissions scenarios show a steady increase in PW in each of the 30-year blocks for all locations. In some cases, very large increases are seen. Lastly, the results of the future changes in meteorological causes and changes in PW were used in the adjustment scheme to the NOAA Atlas 14 tables for each of the OCONUS locations.

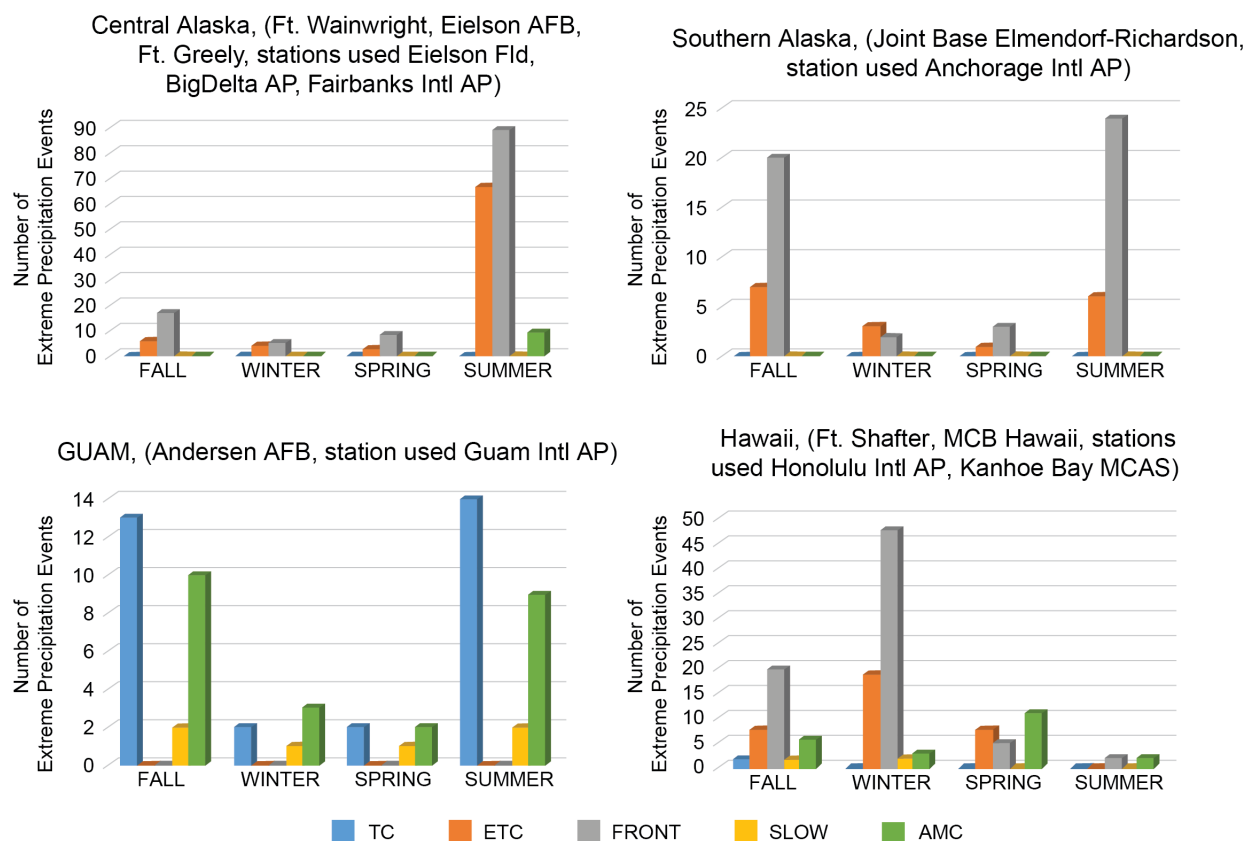


Figure 38. Meteorological causes of heavy precipitation events, by season, for four regions: Central Alaska, Southern Alaska, Hawai‘i, and Guam. Five different causes were included: tropical cyclone (blue), extratropical cyclone (orange), fronts (gray), subtropical low (yellow), and air mass convection (green).

Table 9. Future change (%) in the winter 30-yr maximum daily PW for Honolulu, Hawai‘i for seven 30-year overlapping blocks to the end of the 21st century using climate models forced with the RCP8.5 emissions scenario. Reference period is 1976–2005.

<i>Model Year</i>	<i>2011– 2040</i>	<i>2021– 2050</i>	<i>2031– 2060</i>	<i>2041– 2070</i>	<i>2051– 2080</i>	<i>2061– 2090</i>	<i>2070– 2099</i>
<i>30-yr Max PW change (%)</i>	5	8	10	13	18	24	29
<i>Mean +1.66 Std. Dev.</i>	17	21	24	26	36	47	57
<i>Mean –1.66 Std. Dev.</i>	–6	–4	–3	–0	0	1	1

Task 6: Develop applications, including adjustment factors for current IDF values, and incorporate them into the delivery mechanism for current IDF values to provide convenient and reliable access to appropriate values by the civil engineering community.

The Intensity-Duration-Frequency (IDF) values adjusted for future climate change were produced using the results of the project’s research as implemented through the CAUSES equation. The central values were produced through adjustment factors applied to NOAA Atlas 14 values. Uncertainty ranges were also calculated. These incorporated uncertainties from NOAA Atlas 14 along with uncertainties associated with the adjustment factors. The calculation of the water vapor and weather system adjustment factors and the uncertainty ranges is described below.

Water Vapor Adjustment Component

From the CAUSES equation, the water vapor adjustment term is $(1 + \alpha \Delta PW)$, where ΔPW is the fractional change in precipitable water. The α term is estimated from the water vapor analysis (see Figure 20) and the associated polynomial fit to those data (equation [14] and Figure 21).

The results of the water vapor analysis were further analyzed to generate a relationship between average PW and return level for the $10^\circ \times 10^\circ$ CONUS grid boxes. In all grid boxes, PW is weakly dependent on return level, but the strongest dependence is on region. Figure 39 shows this dependence for the 25-yr return level. Note that the average PW values are higher in the eastern U.S., with the highest values over Florida and south Texas. Values are lower in the western U.S. because of moisture blocking in the interior and because most events are winter events, when PW values are generally lower.

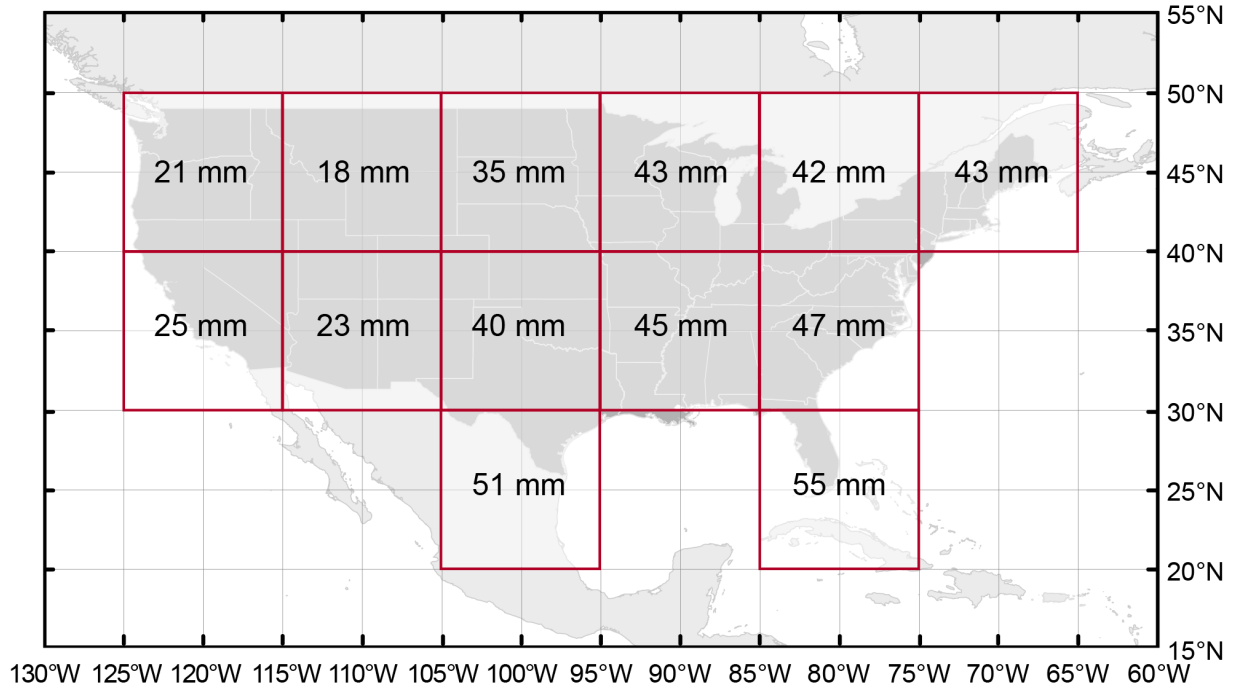


Figure 39. Average PW by region for events of an approximate 25-yr return level.

For a given value of ΔPW , the water vapor adjustment factor was determined in the following manner for a specific region. The current mean value of PW ($PW_{curr,reg}$) was extracted from the calculated tables, as shown in Figure 39 for the 25-yr return level. The PW value used in equation (14) is the midpoint between the current and future values (PW_{mid}),

$$PW_{mid} = PW_{curr,reg} (1 + 0.5\Delta PW) \quad (15)$$

Thus, the water vapor adjustment factor is

$$\text{Water Vapor Adjustment Factor} = [1 + \alpha (PW_{mid}) \Delta PW] \quad (16)$$

Weather System Adjustment Component

As noted in previous sections, climate model simulations were analyzed to determine potential future changes in the occurrences of the weather systems responsible for extreme precipitation events. The analyzed results were expressed in terms of fractional change in the number of systems by season and by $10^\circ \times 10^\circ$ CONUS regions.

The quantitative relationship between the number of systems and the change in return value precipitation amounts was developed with the assumption that additional or fewer weather systems in the future will add or subtract equally from the entire distribution of extreme precipitation events. To illustrate with a simple thought experiment, assume that the number of weather systems doubles. Then, the partial duration series will have double the number of values above a fixed threshold. So, a value that previously had an estimated return period of 20 years will now have a return period of 10 years. Likewise, assume that the number of weather systems is reduced by half. Then the number of events above the fixed threshold will be reduced by half,

and a precipitation magnitude with a return period of 20 years in the current climate will have a return period of 40 years in the future.

The historical (1976–2005) IDF values generated in the generalized extreme value analysis were used to estimate the quantitative relationship between precipitation magnitude and return value. Specifically, IDF values at 1-yr, 2-yr, 5-yr, 10-yr, 25-yr, 50-yr, and 100-yr return levels were averaged over each grid box for 1-day, 5-day, 10-day, 20-day, and 30-day durations. Figure 40 shows an example for grid box #10 for 1-day duration precipitation amounts for selected return levels at an approximate factor of two differences. On average, a doubling of the return level results in an increase in IDF values of about 15%.

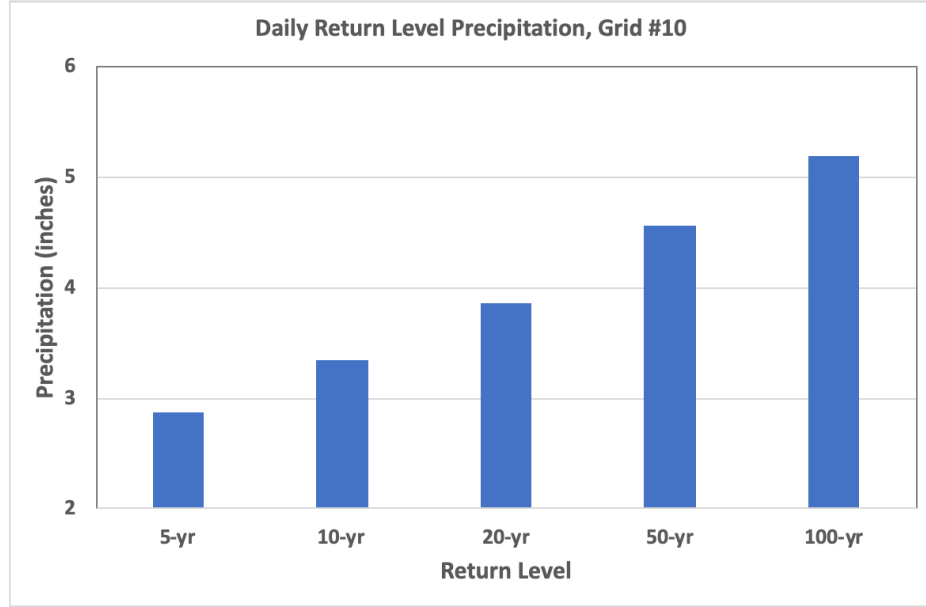


Figure 40. Precipitation amounts for selected return levels for 1-day duration events for grid box #10. These are averages for LOCA grid points within that box.

The results are very similar across duration and region. A doubling of return level increases the IDF values by about 15%, and a halving of return level decreases IDF values by about 15%. The logarithmic function can be used to capture this relationship. Specifically, the following simplified form of the weather adjustment component of the CAUSES equation is applied:

$$\{1 + [0.15 / \ln(2)] [\ln(1 + \Delta WS)]\} \quad (17)$$

where:

ΔWS = fractional change in weather systems weighted by their historical frequency of occurrence, specifically this portion of the CAUSES equation,

$$\Delta WS = \left\{ \sum_{s=1}^4 (\beta(FRT(x, y, s) \Delta FRT(x, y, s, t) + \gamma ETC(x, y, s) \Delta ETC(x, y, s, t))) \right\} \quad (18)$$

Equation (17) has the proper behavior. If there is doubling of weather systems, $\Delta WS = +1$ (100%) and the adjustment factor is 1.15. If there is a halving of weather systems, $\Delta WS = -0.5$ (-50%) and the adjustment factor is 0.85.

Uncertainty Range

NOAA Atlas 14 provides 10th and 90th percentile ranges for all of their design values. The climate change adjustment factors were applied to these range values and to the central (50th percentile) value to preserve the statistical uncertainties in the historical IDF values. The uncertainties in the adjustment factors were calculated as the standard deviations of the multi-model ensemble, thus representing the inter-model variability. These two components (historical statistical uncertainty and climate model uncertainty) of variability were combined as the square root of the sum of squares of the two components. The NOAA Atlas 14 ranges are not always symmetric with respect to the 50th percentile. The procedure took this into account, as follows:

Let

EP^{50} = present midpoint IDF value from NOAA Atlas 14

EP^{10}, EP^{90} = 10th and 90th percentile values of IDF values from NOAA Atlas 14

A = climate change adjustment factor (expressed as fraction) for a given GCM and simulation with respect to the Downscaling or CAUSES methods.

S = standard deviation of A (expressed as fraction) calculated across GCM, simulation, and method

$EP^{50f}, EP^{10f}, EP^{90f}$ = future IDF values and ranges

The calculation of uncertainty ranges used the following set of equations

$$EP^{50f} = A \times EP^{50} \quad (19)$$

$$\Delta EP^{10} = 1.64 \sqrt{(S \times EP^{50})^2 + (EP^{50} - EP^{10})^2} \quad (20)$$

$$\Delta EP^{90} = 1.64 \sqrt{(S \times EP^{50})^2 + (EP^{90} - EP^{50})^2} \quad (21)$$

$$EP^{10f} = EP^{50f} - \Delta EP^{10} \quad (22)$$

$$EP^{90f} = EP^{50f} + \Delta EP^{90} \quad (23)$$

where the factor of 1.64 represents the standard normal deviate of the 10th and 90th percentiles for the cumulative probability of the normal distribution.

The two methods to determine climate change adjustments represent the structural dimension of uncertainty. The adjustment factors from these two methods are considered equally probable and averaged. The standard deviations of the adjustment factors represent the model uncertainty. These are considered to be two samples of this dimension of uncertainty. Thus, they are also averaged. In equation form,

Let

A_{PD} = adjustment factor from the precipitation downscaling method

A_{PC} = adjustment factor from the precipitation causes method

S_{PD} = standard deviation of the adjustment factor from the precipitation downscaling method

S_{PC} = standard deviation of the adjustment factor from the precipitation causes method

Then the average can be written as:

$$A = (A_{PD} + A_{PC})/2 \quad (24)$$

$$S = (S_{PD} + S_{PC})/2 \quad (25)$$

The following example uses Camp Lejeune 24-hr, 25-yr IDF values from NOAA Atlas 14. The values of A and S are simply for purposes of illustration.

$$EP^{50} = 8.56$$

$$EP^{10} = 7.72$$

$$EP^{90} = 9.39$$

$$A_{PC} = 1.534$$

$$A_{PD} = 1.371$$

$$S_{PC} = 26.8\% = 0.268$$

$$S_{PD} = 14.5\% = 0.145$$

$$A = (1.534 + 1.371)/2 = 1.453 \quad (26)$$

$$S = (0.268 + 0.145)/2 = 0.207 \quad (27)$$

$$EP^{50f} = A \times EP^{50} = 1.453 \times 8.56 = 12.43 \quad (28)$$

$$\Delta EP^{10} = 1.64\sqrt{(0.207 \times 8.56)^2 + (8.56 - 7.72)^2} = 3.21 \quad (29)$$

$$\Delta EP^{90} = 1.64\sqrt{(0.207 \times 8.56)^2 + (9.39 - 8.56)^2} = 3.20 \quad (30)$$

$$EP^{10f} = EP^{50f} - \Delta EP^{10} = 12.43 - 3.21 = 9.22 \quad (31)$$

$$EP^{90f} = EP^{50f} + \Delta EP^{90} = 12.43 + 3.20 = 15.64 \quad (32)$$

The range of model projections is relatively large, and this leads to a substantially larger range in the future compared to the NOAA Atlas 14 ranges.

This method for calculating the uncertainty ranges assumes that the multi-model distribution of adjustments follows a normal distribution and that this is an additive component

to the NOAA Atlas 14 uncertainty ranges. There is the potential that this could lead to unrealistically large ranges, particularly on the low end (the 10th percentile limit). However, there is high confidence that atmospheric water vapor content will increase and that the water vapor adjustment factor will be dominant. Therefore, we consider that it is unrealistic for EP^{10f} to be substantially lower than EP^{10} . To avoid this outcome, we impose the following criterion on EP^{10f} ,

$$EP^{10f} \geq 0.8 EP^{10} \quad (33)$$

If the calculation (equations [19]–[25]) result in a value of EP^{10f} that is less than $0.8 \times EP^{10}$, then EP^{10f} is set equal to $0.8 \times EP^{10}$.

Sub-Daily Duration Adjustments

The relationships used for adjustments were based on analyses of daily and multi-day precipitation accumulations. We did not perform similar analyses on sub-daily precipitation for two reasons. First, there are far fewer stations with long records of hourly precipitation data. Second, early in the project the available hourly data were analyzed, but quality issues were found. These two factors together stymied a robust investigation with sufficient confidence and spatial detail.

We applied the adjustment factors for 24-hr (daily) durations to sub-daily (1-hr, 2-hr, 3-hr, 6-hr, and 12-hr) durations. The suitability of this approximation rests primarily on whether the EP–PW relationships we found for daily events extend to sub-daily extremes, since the water vapor adjustment is much larger than the weather system adjustment. Within the context of the water vapor adjustment framework developed here, this question can be narrowed to whether the α term in equation (14) is dependent on EP duration. In our water vapor investigations, we examined the EP–PW for 5-day duration events. We found that the relationship displayed in Figure 20 and quantified in equation (14) was very similar between 1-day and 5-day duration events. In other words, α was found to be nearly constant for durations from 1 to 5 days. To a first approximation then, it is reasonable to assume that equation (14) can be applied to somewhat shorter durations, such as 6 and 12 hrs.

Larger uncertainties about this assumption apply to the very short 1–3 hr durations, where the extreme precipitation may arise from individual convective cells. In this situation, the super-Clausius–Clapeyron (CC) effect may be most likely to occur. The super-CC effect, at its core, is an enhancement of convective upward vertical motion due to release of latent heat and will manifest itself primarily in individual convective cells. The effect on IDF values then will be most apparent at very short durations. Our estimated adjustment factors may then be conservative.

Website

A website was developed to display adjusted IDF values for a user-selected location. The user also selects the future time period and the emissions scenario. There are seven options for future time period: 2025, 2035, 2045, 2055, 2065, 2075, 2085. Each of these actually represents a 30-yr period centered around that date (e.g., 2055 equates to the period 2041–2070). There are two options for scenarios: RCP4.5 (moderate emissions) and RCP8.5 (high emissions).

The baseline IDF values [$EP_{d,f}^{NA14}(x, y)$ in the CAUSES equation] are obtained from NOAA Atlas 14. The adjustment values determined in this project are applied to the NOAA Atlas 14 values as a multiplicative factor and displayed on the website.

Figure 41 is a screenshot of the website showing an example of the military installation selection option. A list is given as a popup menu for the state of Texas, and Fort Hood is selected. Figure 42 displays adjusted IDF values for Fort Hood for 2055 under the high emissions (RCP8.5) scenario. Values are displayed for a range of durations from 1 hr to 30 days and a range of recurrence intervals from 1 yr to 100 yrs.

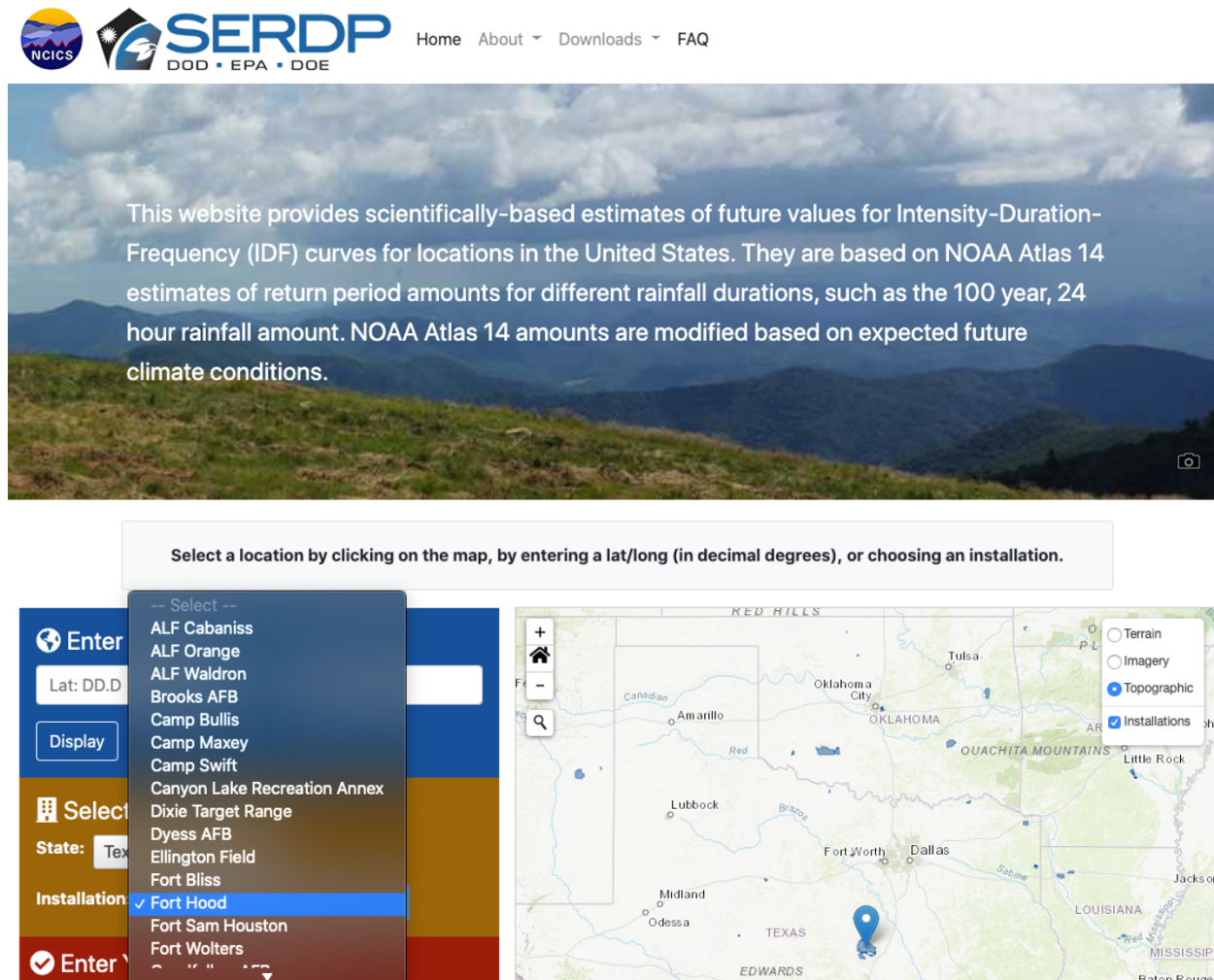


Figure 41. Display of website showing installation selection dropdown menu.

This website provides scientifically-based estimates of future values for Intensity-Duration-Frequency (IDF) curves for locations in the United States. They are based on NOAA Atlas 14 estimates of return period amounts for different rainfall durations, such as the 100 year, 24 hour rainfall amount. NOAA Atlas 14 amounts are modified based on expected future climate conditions.

Select a location by clicking on the map, by entering a lat/long (in decimal degrees), or choosing an installation.

Enter Lat/Lon

Lat: Lon:

Select an Installation

State:

Installation:

Enter Year and Scenario

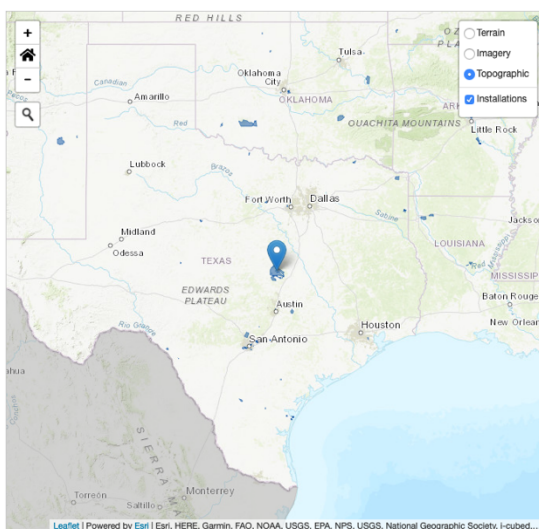
Year: Scenario:

LOCATION

Lat: 31.2 Lon: -97.7

City: Fort Hood State: Texas

County: Coryell County Zip Code: 76544



PRECIPITATION FREQUENCY ESTIMATES (in inches), Year: 2055, Scenario: RCP85							
Location: Fort Hood, Fort Hood, Texas							
DURATION	AVERAGE RECURRENCE INTERVAL						
	1 year	2 years	5 years	10 years	25 years	50 years	100 years
60-min	1.87	2.22	2.77	3.24	3.90	4.41	4.95
2-hr	2.27	2.73	3.45	4.07	4.97	5.68	6.44
3-hr	2.50	3.04	3.86	4.59	5.64	6.49	7.42
6-hr	2.91	3.57	4.57	5.46	6.78	7.87	9.07
12-hr	3.31	4.09	5.25	6.31	7.87	9.15	10.58
24-hr	3.75	4.64	5.99	7.20	8.97	10.44	12.06
2-day	4.28	5.28	6.81	8.17	10.13	11.71	13.46
3-day	4.66	5.72	7.37	8.82	10.89	12.54	14.35
4-day	4.96	6.07	7.81	9.32	11.49	13.20	15.06
7-day	5.67	6.89	8.79	10.44	12.78	14.63	16.61
10-day	6.27	7.56	9.59	11.33	13.80	15.74	17.79
20-day	8.10	9.53	11.88	13.83	16.51	18.55	20.63
30-day	9.60	11.15	13.74	15.84	18.67	20.77	22.85

Figure 42. Display of website showing adjusted IDF values for 2055 under the RCP8.5 emissions scenario.

Conclusions and Implications for Future Research/Implementation

The overriding objective of this project was to develop a framework for incorporating future climate change into the Intensity-Duration-Frequency (IDF) values of extreme precipitation used for engineering design. This objective was successfully accomplished. The scientific findings were used to develop adjustment factors that were applied to existing IDF values from NOAA Atlas 14. The adjustment factors incorporate future changes in atmospheric water vapor and in the meteorological systems responsible for extreme precipitation. A website was developed to deliver these adjusted IDF values, which incorporate potential future changes in extreme precipitation from anthropogenic climate change under a moderate and high emissions scenario (RCP4.5 and RCP8.5). Design values are available for seven future target periods: 30-yr periods centered on 2025, 2035, 2045, 2055, 2635, 2075, and 2085.

The major scientific finding is that atmospheric water vapor concentration is the major determining factor for the magnitude of extreme precipitation events. An analysis of historical events showed that extreme precipitation amounts scale closely with precipitable water (vertically integrated water vapor) and that the scaling factor increases with increasing precipitable water. Analysis of global climate model simulations indicates that global warming leads to increases in atmospheric water vapor concentrations at approximately the Clausius–Clapeyron rate ($\sim 7\% \text{ }^{\circ}\text{C}^{-1}$). Water vapor is the dominant component in the adjustment factors. This is a consequence of the strong relationship in the observational record between extreme precipitation amounts and water vapor combined with the highly confident projections of large increases of future water vapor. This leads to large ($>20\%$) increases in IDF values by the end of the century under the high emissions scenario (RCP8.5).

Analyses of future changes in weather systems investigated fronts, extratropical cyclones (ETCs), tropical cyclones (TCs), and North American Monsoon moisture surges. Among these weather systems, fronts are the dominant cause of extreme precipitation events in most areas of the U.S., followed by ETCs. When broken down by season, summer fronts are the single most dominant trigger for extreme precipitation events over much of the eastern two-thirds of CONUS. Unlike atmospheric water vapor concentration, with large projected increases everywhere, future changes in the frequency of these systems are regionally and seasonally variable. However, climate model simulations indicate future decreases in fronts and ETCs in many areas. For extreme precipitation events triggered by weather systems, the most important future projection is a decrease in summer fronts almost everywhere. This is in conjunction with the fact that fronts, overall, are the dominant trigger of extreme precipitation events. Review of recent published research and our own analysis indicate that climate model simulations of TCs and monsoon moisture surges are too uncertain to rely on for incorporation into the adjustment factors. Furthermore, atmospheric water vapor appears to be the primary factor for increases in rainfall associated with these systems, and this factor is already incorporated into the adjustment factors. The overall outcome of the weather systems research is that the future changes in fronts and ETCs tend to decrease IDF values, but the magnitudes of their effects are much smaller than the increase projected as a result of the changes in the water vapor component.

The major technical challenge of the project was the identification of fronts in climate model simulation data. Our previous work had used manual methods, but this was not practical for analyzing large amounts of climate model data. Addressing this challenge led to the major technical advancement of the project: the development of an automated frontal detection algorithm. This algorithm was developed using a deep learning convolutional neural network

that was trained with a dataset of manually drawn fronts produced by NOAA's National Weather Service. The algorithm was crucial to the success of this project. With it, we were able to readily analyze several hundred years of climate model simulation data from many climate models. It has garnered interest from the National Center for Atmospheric Research and the Department of Energy national labs (personal communication).

Analysis of extreme precipitation confirmed the occurrence of widespread upward historical trends in the number and intensity of events over the U.S. There are important regional variations in this general behavior. The largest upward trends are observed over the eastern half of the U.S. Lesser upward trends are observed over the western U.S., with slight downward trends over parts of the far west and Southwest. The largest trend magnitudes are observed for the most extreme events. These analyses detail the extent and magnitude of non-stationarity of extreme precipitation in the U.S. for a range of relevant duration and recurrence intervals over the 20th and early 21st centuries.

A complementary method was developed based on generalized extreme value (GEV) methodology. This analysis used the Localized Constructed Analogs dataset, which is a relatively new statistically downscaled dataset for the continental U.S. This dataset includes daily precipitation data for 32 CMIP5 models covering the period 1950–2100. Spatial resolution is 1/16th degree. We performed GEV analysis on the annual maximum series of 1-day, 5-day, 10-day, 20-day, and 30-day precipitation totals for four 30-yr periods (1976–2005, 2006–2035, 2036–2065, and 2070–2099) to estimate future changes in various return period amounts. The following conclusions are derived from this GEV analysis:

- The future changes in return period threshold values increase with return period, 100-yr changes being greater than 5-yr changes.
- The future changes increase substantially with increased greenhouse gas forcing.
- The future changes are very large by the end of the century under the RCP8.5 scenario.
- The spatial variability is relatively small compared to the magnitude of the changes by the mid- to late 21st century.
- Future changes generally decrease slightly with increasing duration.

This separate GEV-derived set of adjustment factors was combined with the adjustment factors derived from the water vapor and weather systems approach, which added to our uncertainty estimates.

Our work provides support for the three proposed hypotheses:

Hypothesis 1: *Historically observed and anthropogenically forced future changes in IDF values used in the engineering community arise primarily from two principal meteorological sources: 1) changes in atmospheric water vapor concentration (potential) and 2) changes in the frequency and intensity of the weather systems that cause heavy precipitation (triggers).*

Analyses also showed that when the atmosphere is moisture-rich, extreme precipitation events are readily triggered; but when the atmosphere is moisture-limited, only strong weather systems can trigger extreme precipitation events.

Hypothesis 2: *As the time horizon increases, IDF values will increase primarily because GCMs project increasing temperature and related water vapor altered by concomitant changes in the frequency and intensity of fronts and storm tracks and other changes in circulation.*

Somewhat surprisingly, fronts are especially important during the warm season, when many extreme precipitation events occur, and knowing their change in frequency is more important compared to extratropical storm tracks.

Hypothesis 3: *Regional variations in the changes of IDF values arise primarily from regional differences in water vapor, weather/climate systems, and regional aspects of terrain and ocean influence.*

The differences in IDF values from region to region were found to favor a preferred combination of the factors in hypothesis 3 that were seasonally dependent.

There are several areas of additional investigation that could help improve estimates of future IDF values. First, a thorough analysis of the new CMIP6 simulations, involving an analysis of the three key meteorological factors used—water vapor, fronts, and ETCs—should be undertaken. A small set of CMIP6 simulations were analyzed late in this project for the frontal analysis, which required 3-hourly time resolution climate model data unavailable in CMIP5. While it is unlikely that major features found in the current study would change, there would likely be some increased regional confidence.

Second, an investigation of sub-daily resolution precipitation data could improve the quality of the sub-daily IDF adjustments. This would require a development of a spatially dense, high-quality hourly precipitation dataset spanning an adequate number of years. Additionally, models with very high spatial resolution (cloud-resolving) would be extremely useful. Model simulations at these resolutions are becoming increasingly available and are the best tool to investigate super-Clausius–Clapeyron scaling at high time resolutions. In the current work, it was necessary to apply our daily-time-resolution water vapor scaling to sub-daily IDF resolutions. High-resolution observations and model simulations can provide information on whether this scaling holds.

Third, an investigation similar to what we performed would be useful in other areas outside the contiguous U.S., Alaska, Hawai‘i, and Guam.

Fourth, a further look at tropical and extratropical cyclone intensities would be useful. There is increasing evidence that these weather systems will change their probability frequency distribution related to storm intensity as the climate warms. A better understanding of how this interplays with more water vapor could be important for some regions.

Lastly, a thorough testing of the combination of statistical, structural, and global climate model uncertainties using historical observational data would be very useful to help validate uncertainty estimates.

The adjusted IDF values developed in this research are suitable for application to DoD installations. Our research found that water vapor is the dominant factor in determining extreme precipitation amounts. Future increases in water vapor are one of the climate model projections in which scientists are most confident. Thus, use of current IDF values that do not incorporate the non-stationarity of the climate will increasingly underestimate extreme rainfall as time horizons of interest increase.

Literature Cited

- Abadi, M., A. Agarwal, P. Barham, E. Brevdo, Z. Chen, C. Citro, G.S. Corrado, A. Davis, J. Dean, M. Devin, and S. Ghemawat, 2015: TensorFlow: Large-scale machine learning on heterogeneous systems, <https://www.tensorflow.org/>.
- Agilan, V. and N.V. Umamahesh, 2016: Is the covariate based non-stationary rainfall IDF curve capable of encompassing future rainfall changes? *Journal of Hydrology*, **541**, 1441–1455. <http://dx.doi.org/10.1016/j.jhydrol.2016.08.052>
- Bergstra, J., O. Breuleux, F. Bastien, P. Lamblin, R. Pascanu, G. Desjardins, J. Turian, D. Warde-Farley, and Y. Bengio, 2010: Theano: A CPU and GPU Math Expression Compiler. Proceedings of the Python for Scientific Computing Conference (SciPy) 2010.
- Biard, J.C. and K.E. Kunkel, 2019: Automated detection of weather fronts using a deep learning neural network. *Advances in Statistical Climatology, Meteorology and Oceanography*, **5** (2), 147–160. <http://dx.doi.org/10.5194/asmo-5-147-2019>
- Bonnin, G.M., D. Martin, B. Lin, T. Parzybok, M. Yekta, and D. Riley, 2004: Precipitation Frequency Atlas of the United States. Volume 1, Version 5.0: Semiarid Southwest (Arizona, Southeast California, Nevada, New Mexico, Utah) NOAA Atlas 14. 277 pp.
- Chandra, R., U. Saha, and P.P. Mujumdar, 2015: Model and parameter uncertainty in IDF relationships under climate change. *Advances in Water Resources*, **79**, 127–139. <http://dx.doi.org/10.1016/j.advwatres.2015.02.011>
- Cheng, L. and A. AghaKouchak, 2014: Nonstationary precipitation Intensity-Duration-Frequency curves for infrastructure design in a changing climate. *Scientific Reports*, **4** (1), 7093. <http://dx.doi.org/10.1038/srep07093>
- Chollet, F., 2015: Keras: The Python Deep Learning library, <https://keras.io>.
- Coles, S.G., 2001: An Introduction to the Statistical Modeling of Extreme Values. Springer, New York.
- DeGaetano, A.T. and C.M. Castellano, 2017: Future projections of extreme precipitation intensity-duration-frequency curves for climate adaptation planning in New York State. *Climate Services*, **5**, 23–35. <http://dx.doi.org/10.1016/j.cliser.2017.03.003>
- Deng, L. and D. Yu, 2014: Deep learning: Methods and Applications. *Foundations and Trends® in Signal Processing*, **7** (3–4), 197–387. <http://dx.doi.org/10.1561/20000000039>
- Durre, I., M.J. Menne, and R.S. Vose, 2008: Strategies for evaluating quality assurance procedures. *Journal of Applied Meteorology and Climatology*, **47** (6), 1785–1791. <http://dx.doi.org/10.1175/2007JAMC1706.1>
- Durre, I., M.J. Menne, B.E. Gleason, T.G. Houston, and R.S. Vose, 2010: Comprehensive automated quality assurance of daily surface observations. *Journal of Applied Meteorology and Climatology*, **49** (8), 1615–1633. <http://dx.doi.org/10.1175/2010JAMC2375.1>
- Easterling, D.R. and M.F. Wehner, 2009: Is the climate warming or cooling? *Geophysical Research Letters*, **36** (8). <http://dx.doi.org/10.1029/2009GL037810>

- Emori, S. and S.J. Brown, 2005: Dynamic and thermodynamic changes in mean and extreme precipitation under changed climate. *Geophysical Research Letters*, **32** (17). <http://dx.doi.org/doi:10.1029/2005GL023272>
- Ganguli, P. and P. Coulibaly, 2017: Does nonstationarity in rainfall require nonstationary intensity–duration–frequency curves? *Hydrology and Earth System Sciences*, **21** (12), 6461–6483. <http://dx.doi.org/10.5194/hess-21-6461-2017>
- Gelaro, R., W. McCarty, M.J. Suárez, R. Todling, A. Molod, L. Takacs, C.A. Randles, A. Darmenov, M.G. Bosilovich, R. Reichle, K. Wargan, L. Coy, R. Cullather, C. Draper, S. Akella, V. Buchard, A. Conaty, A.M. da Silva, W. Gu, G.-K. Kim, R. Koster, R. Lucchesi, D. Merkova, J.E. Nielsen, G. Partyka, S. Pawson, W. Putman, M. Rienecker, S.D. Schubert, M. Sienkiewicz, and B. Zhao, 2017: The Modern-Era Retrospective Analysis for Research and Applications, Version 2 (MERRA-2). *Journal of Climate*, **30** (14), 5419–5454. <http://dx.doi.org/10.1175/JCLI-D-16-0758.1>
- Giorgi, F. and L.O. Mearns, 2003: Probability of regional climate change based on the Reliability Ensemble Averaging (REA) method. *Geophysical Research Letters*, **30** (12). <http://dx.doi.org/10.1029/2003GL017130>
- Goodfellow, I., Y. Bengio, and A. Courville, 2016: *Deep Learning*. MIT Press, 800 pp.
- IPCC, 2013: Climate Change 2013: The Physical Science Basis. Contribution of Working Group I to the Fifth Assessment Report of the Intergovernmental Panel on Climate Change. Stocker, T.F., D. Qin, G.-K. Plattner, M. Tignor, S.K. Allen, J. Boschung, A. Nauels, Y. Xia, V. Bex, and P.M. Midgley, Eds. Cambridge University Press, Cambridge, UK and New York, NY, 1535 pp. <http://www.climatechange2013.org/report/>
- Kalnay, E., M. Kanamitsu, R. Kistler, W. Collins, D. Deaven, L. Gandin, M. Iredell, S. Saha, G. White, J. Woollen, Y. Zhu, M. Chelliah, W. Ebisuzaki, W. Higgins, J. Janowiak, K.C. Mo, C. Ropelewski, J. Wang, A. Leetmaa, R. Reynolds, R. Jenne, and D. Joseph, 1996: The NCEP/NCAR 40-Year Reanalysis Project. *Bulletin of the American Meteorological Society*, **77** (3), 437–472. [http://dx.doi.org/10.1175/1520-0477\(1996\)077](http://dx.doi.org/10.1175/1520-0477(1996)077)
- Kanamitsu, M., W. Ebisuzaki, J. Woollen, S.-K. Yang, J.J. Hnilo, M. Fiorino, and G.L. Potter, 2002: NCEP–DOE AMIP-II Reanalysis (R-2). *Bulletin of the American Meteorological Society*, **83** (11), 1631–1644. <http://dx.doi.org/10.1175/BAMS-83-11-1631>
- Karl, T.R. and A.J. Koscielny, 1982: Drought in the United States: 1895–1981. *Journal of Climatology*, **2** (4), 313–329. <http://dx.doi.org/10.1002/joc.3370020402>
- Karl, T.R. and W.J. Koss, 1984: Regional and National Monthly, Seasonal, and Annual Temperature Weighted by Area, 1895–1983. Historical Climatology Series 4–3. National Climatic Data Center, Asheville, NC, 38 pp.
- Kingma, D. and J. Ba, 2015: Adam: a method for stochastic optimization, arXiv, arXiv:1412.6980, 15.
- Knapp, K.R., S. Applequist, H.J. Diamond, J.P. Kossin, M. Kruk, and C. Schreck. 2010: *NCDC International Best Track Archive for Climate Stewardship (IBTrACS) Project, Version 3*. NOAA National Centers for Environmental Information. <http://dx.doi.org/10.7289/V5NK3BZP>

- Knutson, T., S.J. Camargo, J.C.L. Chan, K. Emanuel, C.-H. Ho, J. Kossin, M. Mohapatra, M. Satoh, M. Sugi, K. Walsh, and L. Wu, 2020: Tropical Cyclones and Climate Change Assessment: Part II: Projected Response to Anthropogenic Warming. *Bulletin of the American Meteorological Society*, **101** (3), E303–E322. <http://dx.doi.org/10.1175/BAMS-D-18-0194.1>
- Kunkel, K. E., D.R. Easterling, K. Redmond, and K. Hubbard, 2003: Temporal variations of extreme precipitation events in the United States: 1895–2000, *Geophys. Res. Lett.*, **30**, 1900, 10.1029/2003GL018052.
- Kunkel, K.E., T.R. Karl, and D.R. Easterling, 2007: A Monte Carlo assessment of uncertainties in heavy precipitation frequency variations. *J. Hydrometeor.*, **8**, 1152–1160
- Kunkel, K., T.R. Karl, D. Easterling, K. Redmond, J. Young, X. Yin, and P. Hennon, 2013: Probable maximum precipitation and climate change. *Geophysical Research Letters*, **40**, 1402–1408. <http://dx.doi.org/10.1002/grl.50334>
- Kunkel, K.E., D.R. Easterling, D.A.R. Kristovich, B. Gleason, L. Stoecker, and R. Smith, 2012: Meteorological causes of the secular variations in observed extreme precipitation events for the conterminous United States. *Journal of Hydrometeorology*, **13** (3), 1131–1141. <http://dx.doi.org/10.1175/JHM-D-11-0108.1>
- Kunkel, K.E., T.R. Karl, H. Brooks, J. Kossin, J. Lawrimore, D. Arndt, L. Bosart, D. Changnon, S.L. Cutter, N. Doesken, K. Emanuel, P.Ya. Groisman, R.W. Katz, T. Knutson, J. O’Brien, C. J. Paciorek, T. Peterson, K. Redmond, D. Robinson, J. Trapp, R. Vose, S. Weaver., M. Wehner, K. Wolter, D. Wuebbles, 2013: Monitoring and understanding changes in extreme storms: state of knowledge. *Bull. Amer. Meteor. Soc.*, **94**, 499–514, doi: <http://dx.doi.org/10.1175/BAMS-D-12-00066.1>.
- Kunkel, K.E., S. Stevens, L. Stevens, and T.R. Karl, 2020a: Observed climatological relationships of extreme daily precipitation events and precipitable water and vertical velocity in the contiguous United States. *Geophysical Research Letters*, **47**, e2019GL086721. <http://dx.doi.org/10.1029/2019GL086721>
- Kunkel, K.E., T.R. Karl, M.F. Squires, X. Yin, S.T. Stegall, and D.R. Easterling, 2020b: Precipitation extremes: Trends and relationships with average precipitation and precipitable water in the contiguous United States. *Journal of Applied Meteorology and Climatology*, **59** (1), 125–142. <http://dx.doi.org/10.1175/JAMC-D-19-0185.1>
- Lanza, L., M. Leroy, C. Alexandropoulos, L. Stagi, and W. Wauben, 2007: WMO Laboratory Intercomparison of Rainfall Intensity Gauges. World Meteorological Organization Laboratory. https://www.wmo.int/pages/prog/www/IMOP/reports/2003-2007/RI-IC_Final_Report.pdf
- Lanzante, J.R., K.W. Dixon, M.J. Nath, C.E. Whitlock, and D. Adams-Smith, 2018: Some pitfalls in statistical downscaling of future climate. *Bulletin of the American Meteorological Society*, **99** (4), 791–803. <http://dx.doi.org/10.1175/BAMS-D-17-0046.1>
- Li, H., J. Sheffield, and E.F. Wood, 2010: Bias correction of monthly precipitation and temperature fields from Intergovernmental Panel on Climate Change AR4 models using equidistant quantile matching. *Journal of Geophysical Research (Atmospheres)*, **115**, D10101. <http://dx.doi.org/10.1029/2009JD012882>

- Lima, C.H.R., H.-H. Kwon, and J.-Y. Kim, 2016: A Bayesian beta distribution model for estimating rainfall IDF curves in a changing climate. *Journal of Hydrology*, **540**, 744–756. <http://dx.doi.org/10.1016/j.jhydrol.2016.06.062>
- Menne, M.J., I. Durre, R.S. Vose, B.E. Gleason, and T.G. Houston, 2012: An overview of the Global Historical Climatology Network-Daily database. *Journal of Atmospheric and Oceanic Technology*, **29** (7), 897–910. <http://dx.doi.org/10.1175/JTECH-D-11-00103.1>
- Mesinger, F., G. DiMego, E. Kalnay, K. Mitchell, P.C. Shafran, W. Ebisuzaki, D. Jović, J. Woollen, E. Rogers, E.H. Berbery, M.B. Ek, Y. Fan, R. Grumbine, W. Higgins, H. Li, Y. Lin, G. Manikin, D. Parrish, and W. Shi, 2006: North American Regional Reanalysis. *Bulletin of the American Meteorological Society*, **87** (3), 343–360. <http://dx.doi.org/10.1175/BAMS-87-3-343>
- Meyer, J.D.D. and J. Jin, 2017: The response of future projections of the North American monsoon when combining dynamical downscaling and bias correction of CCSM4 output. *Climate Dynamics*, **49** (1), 433–447. <http://dx.doi.org/10.1007/s00382-016-3352-8>
- Nie, J., A.H. Sobel, D.A. Shaevitz, and S. Wang, 2018: Dynamic amplification of extreme precipitation sensitivity. *Proceedings of the National Academy of Sciences*, **115** (38), 9467. <http://dx.doi.org/10.1073/pnas.1800357115>
- NOAA NWS, 2020: Precipitation Frequency Data Server (NOAA Atlas 14). National Oceanic and Atmospheric Administration National Weather Service. <https://hdsc.nws.noaa.gov/hdsc/pfds/>
- Otkin, J.A. and J.E. Martin, 2004: A synoptic climatology of the subtropical kona storm. *Monthly Weather Review*, **132** (6), 1502–1517. [https://doi.org/10.1175/1520-0493\(2004\)132<1502:ASCOTS>2.0.CO;2](https://doi.org/10.1175/1520-0493(2004)132<1502:ASCOTS>2.0.CO;2)
- O’Gorman, P.A. and T. Schneider, 2009: The physical basis for increases in precipitation extremes in simulations of 21st-century climate change. *Proceedings of the National Academy of Sciences*, **106** (35), 14773–14777. <http://dx.doi.org/10.1073/pnas.0907610106>
- Pascale, S., W.R. Boos, S. Bordoni, T.L. Delworth, S.B. Kapnick, H. Murakami, G.A. Vecchi, and W. Zhang, 2017: Weakening of the North American monsoon with global warming. *Nature Climate Change*, **7** (11), 806–812. <http://dx.doi.org/10.1038/nclimate3412>
- Pedregosa, F., G. Varoquaux, A. Gramfort, V. Michel, B. Thirion, O. Grisel, M. Blondel, P. Prettenhofer, R. Weiss, V. Dubourg, J. Vanderplas, A. Passos, D. Cournapeau, M. Perrot, and É. Duchesnay, 2011: Scikit-learn: Machine Learning in Python, *Journal of Machine Learning Research*, **12**, 2825–2830.
- Pierce, D.W., D.R. Cayan, and B.L. Thrasher, 2014: Statistical downscaling using Localized Constructed Analogs (LOCA). *Journal of Hydrometeorology*, **15** (6), 2558–2585. <http://dx.doi.org/10.1175/JHM-D-14-0082.1>
- Simonovic, S.P., A. Schardong, D. Sandink, and R. Srivastav, 2016: A web-based tool for the development of Intensity Duration Frequency curves under changing climate. *Environmental Modelling & Software*, **81**, 136–153. <http://dx.doi.org/10.1016/j.envsoft.2016.03.016>

- Srivastav, R.K., A. Schardong, and S.P. Simonovic, 2014: Equidistance quantile matching method for updating IDF curves under climate change. *Water Resources Management*, **28** (9), 2539–2562. <http://dx.doi.org/10.1007/s11269-014-0626-y>
- Stull, R., 2016: Practical Meteorology: An Algebra-based Survey of Atmospheric Science. Sundog Publishing, LLC, 942 pp.
- Taylor, K.E., R.J. Stouffer, and G.A. Meehl, 2012: An overview of CMIP5 and the experiment design. *Bulletin of the American Meteorological Society*, **93** (4), 485–498. <http://dx.doi.org/10.1175/BAMS-D-11-00094.1>
- van der Walt, S., C. Colbert, and G. Varoquaux, 2011: The NumPy array: A structure for efficient numerical computation. *Computing in Science and Engineering, Institute of Electrical and Electronics Engineers*, **13** (2), 22–30. <https://hal.inria.fr/inria-00564007/document>
- van der Walt, S., J.L. Schönberger, J. Nunez-Iglesias, F. Boulogne, J.D. Warner, N. Yager, E. Gouillart, T. Yu, and scikit-image contributors, 2014: *Scikit-image: Image processing in Python*. <http://dx.doi.org/10.7717/peerj.453>
- Walsh, J., D. Wuebbles, K. Hayhoe, J. Kossin, K. Kunkel, G. Stephens, P. Thorne, R. Vose, M. Wehner, J. Willis, D. Anderson, V. Kharin, T. Knutson, F. Landerer, T. Lenton, J. Kennedy, and R. Somerville, 2014: Appendix 3: Climate Science Supplement. *Climate Change Impacts in the United States: The Third National Climate Assessment*. Melillo, J.M., Terese (T.C.) Richmond, and G.W. Yohe, Eds. U.S. Global Change Research Program, Washington, DC, 735–789. <http://dx.doi.org/10.7930/J0KS6PHH>
- Westra, S., H.J. Fowler, J.P. Evans, L.V. Alexander, P. Berg, F. Johnson, E.J. Kendon, G. Lenderink, and N.M. Roberts, 2014: Future changes to the intensity and frequency of short-duration extreme rainfall. *Reviews of Geophysics*, **52** (3), 522–555. <http://dx.doi.org/doi:10.1002/2014RG000464>
- Zenodo, 2019: National Weather Service Coded Surface Bulletins, 2003–. <https://zenodo.org/record/2642801#.Xtajv55Kjeo>

Appendices

Supporting Data

Additional Water Vapor Analyses

Figure A1 shows the probability distributions by region of the number of all days and the number of days with extreme precipitation exceeding the threshold for a 1-yr recurrence interval as a function of the upward vertical velocity ($-\omega$). Figures A2a and A2b provide a warm-season and cold-season disaggregation of the annual results in Figure 18. Figures A3a and A3b provide a warm-season and cold-season disaggregation of the annual results in Figure A1. Figure A4 shows the relationship between PW and the areal coverage of precipitation amounts exceeding the threshold for a 1-yr recurrence on days when at least 1 station observed such an event. The figure illustrates the dependence of extreme precipitation area on PW. Figure A5 displays boxplots of **A** relative to PW for events of the annual maximum series, similar to Figure 20b. Figure A6 compares the NCEP/NCAR and MERRA-2 reanalyses for the set of analyses shown in Figure 20b. Figure A7 depicts the regional breakdown of Figure 20b.

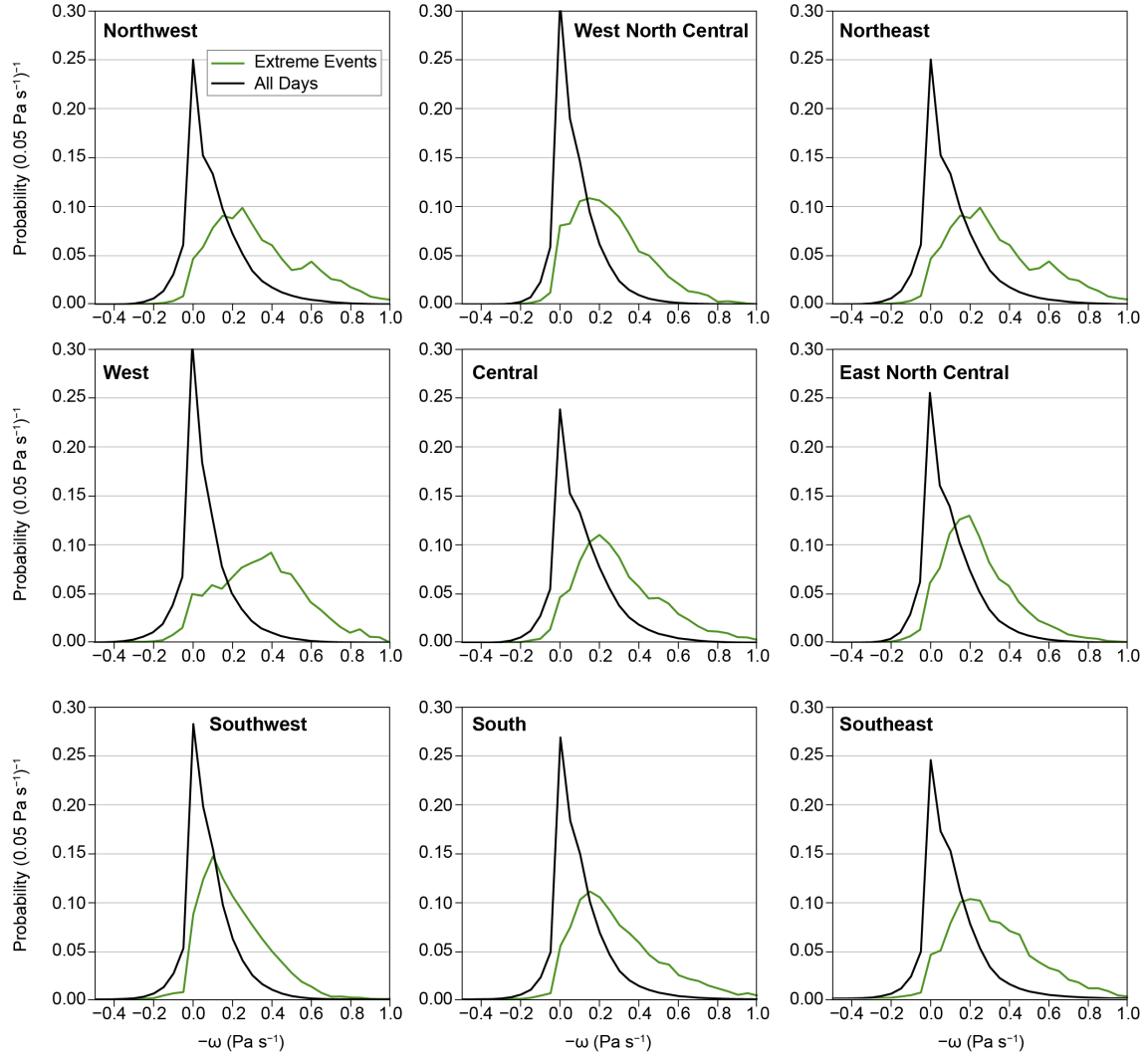
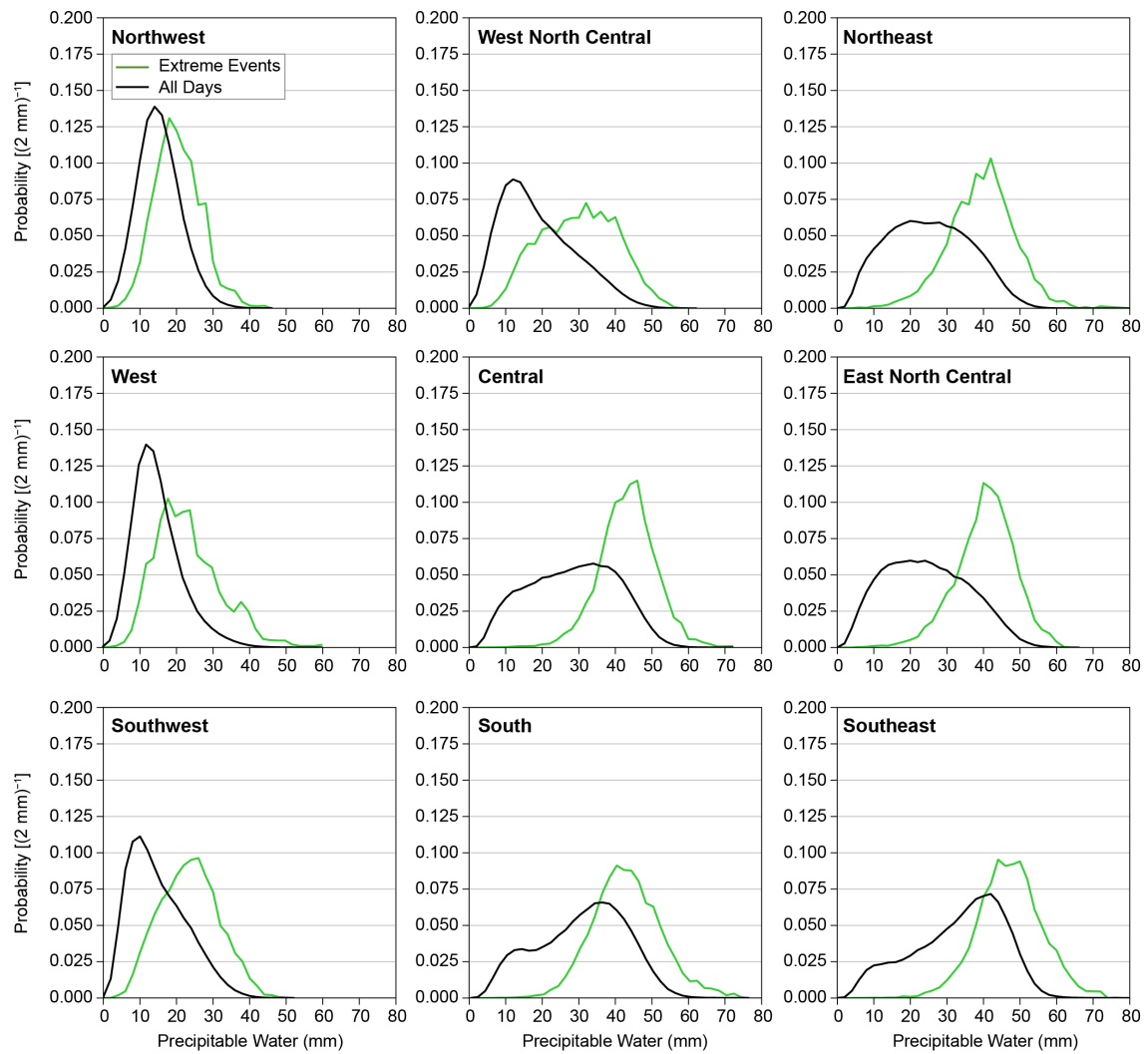


Figure A1. Annual fractional probability distribution of all days (black line) and days with an extreme (1-yr, 1-day recurrence) precipitation event (green line) vs $-\omega$ (the 3-hr maximum during the day of the event) in increments of 0.05 Pa s^{-1} by climate region.

(a) Precipitation vs. Precipitable Water (warm season)



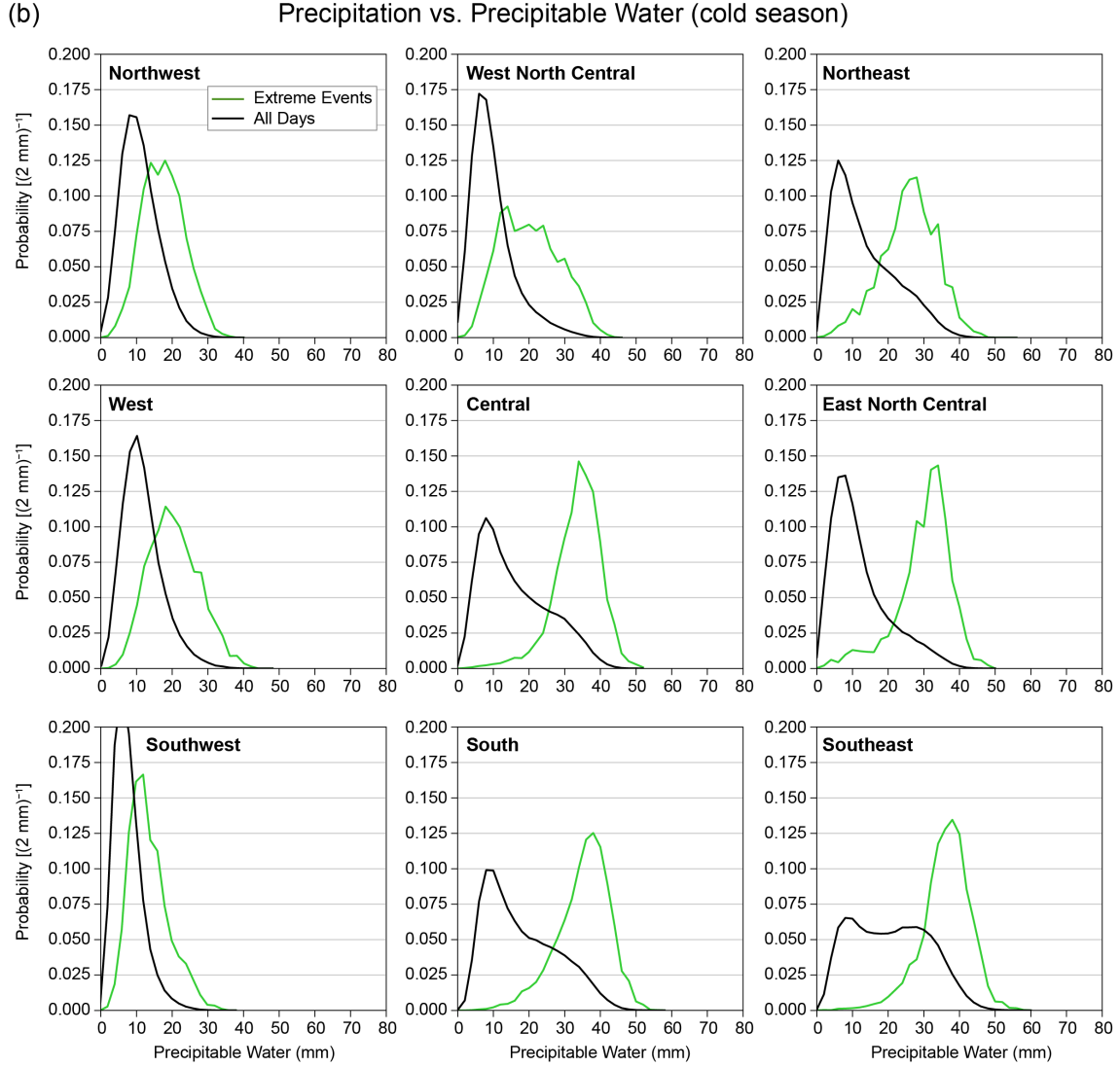
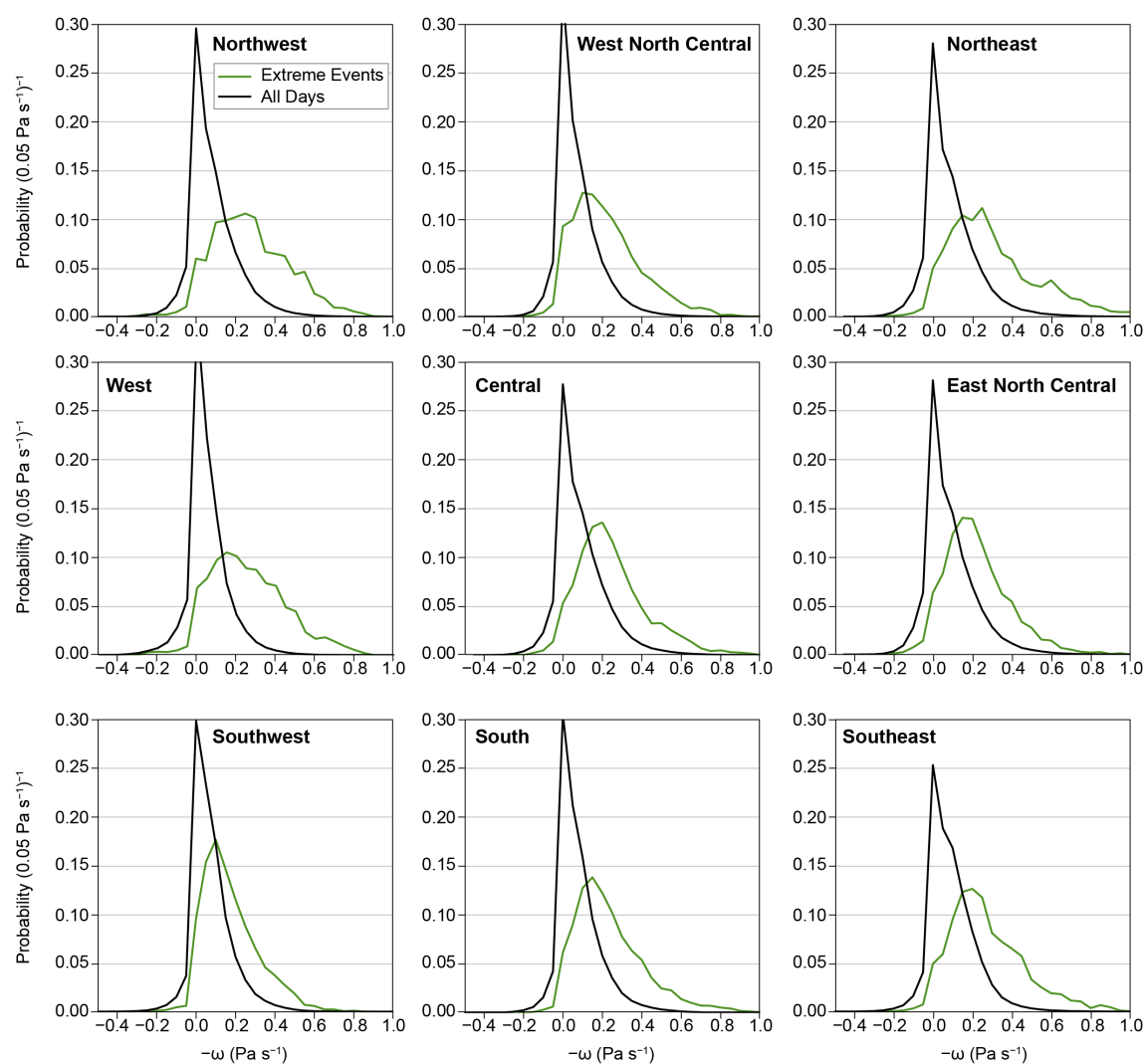


Figure A2. Fractional probability distribution of all days (black line) and days with an extreme (1-yr, 1-day recurrence) precipitation event (green line) vs precipitable water (the 3-hr maximum during the day of the event) in 2 mm increments by climate region for (a) warm season and (b) cold season.

(a) Precipitation vs. $-\omega$ (warm season)



(b)

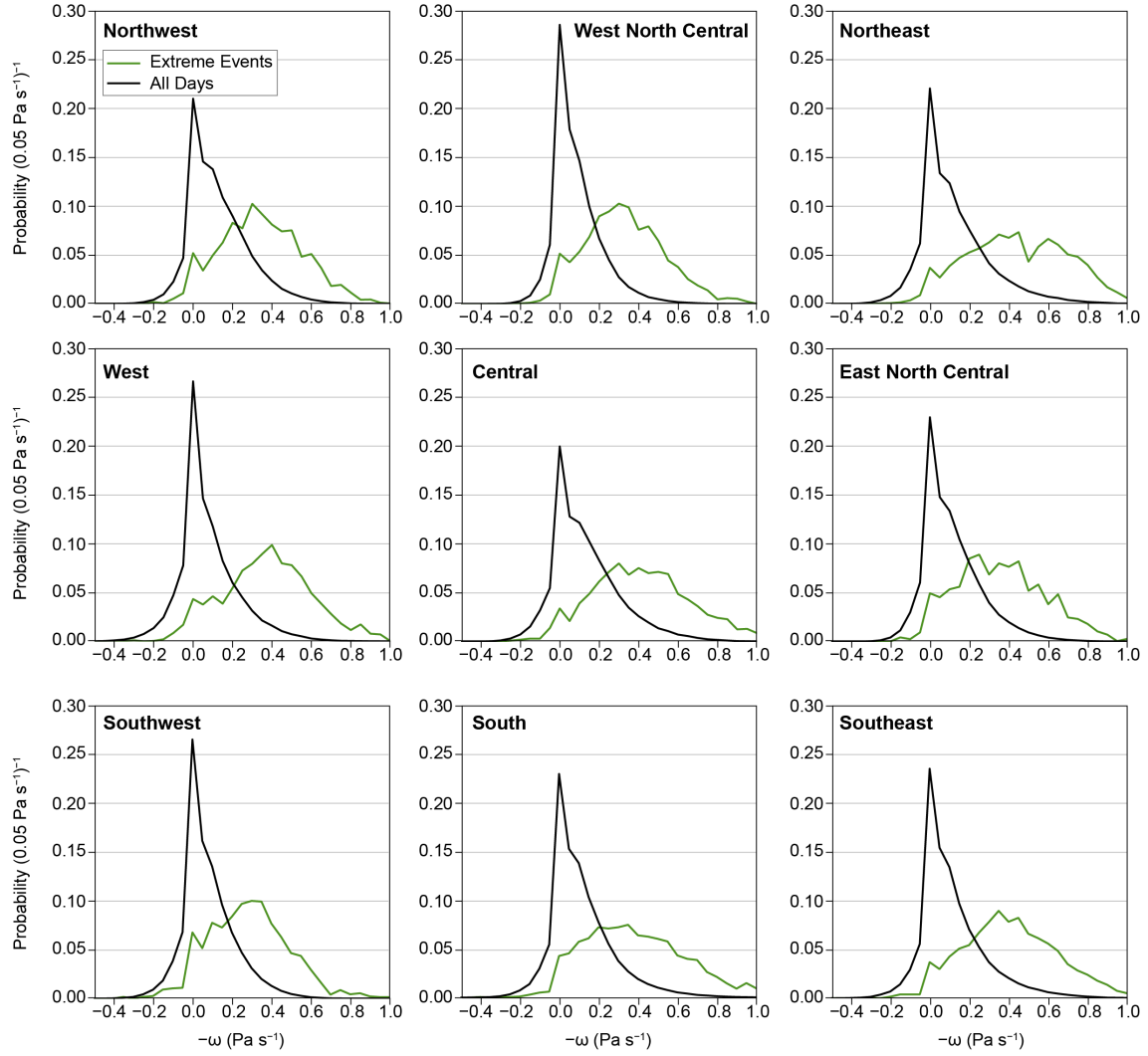
Precipitation vs. $-\omega$ (cold season)

Figure A3. Fractional probability distribution of all days (black line) and days with an extreme (1-yr, 1-day recurrence) precipitation event (green line) vs $-\omega$ (the 3-hr maximum during the day of the event) in increments of 0.05 Pa s^{-1} by climate region for (a) warm season and (b) cold season.

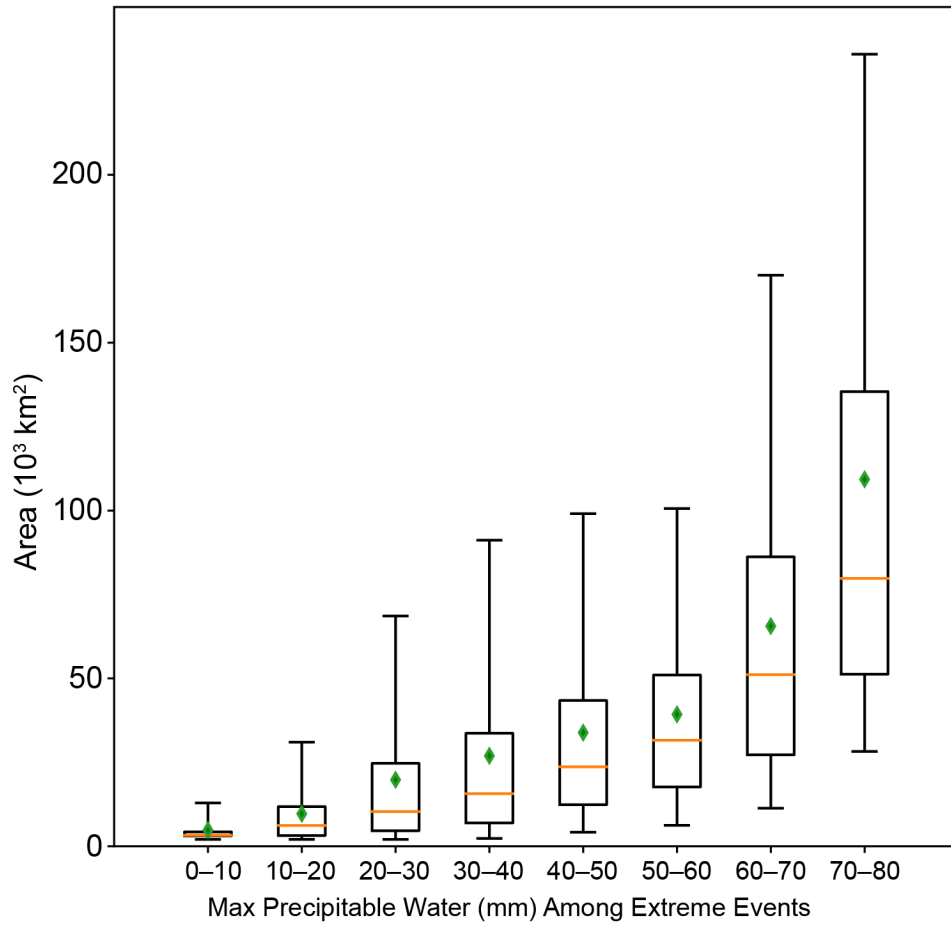


Figure A4. Boxplot distributions of the areal coverage of daily precipitation exceeding the threshold for a 1-yr recurrence interval on days when at least 1 station experienced such an event. Boxplot parameters include mean (green diamonds), median (orange horizontal lines), 25th and 75th percentiles (box limits), and 5th and 95th percentiles (whiskers). The mean, median, and all displayed percentile values of the boxplots increase monotonically with precipitable water.

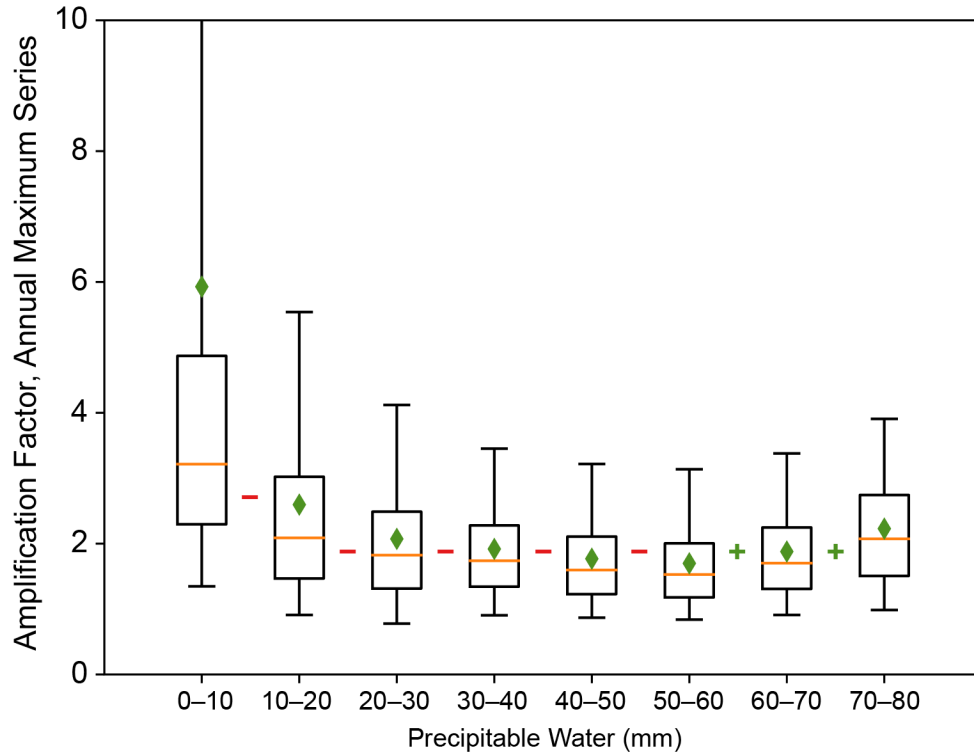


Figure A5. Boxplot distributions of the ratio of precipitation magnitude to same-day 3-hour maximum precipitable water for events in the AMS. Boxplot parameters include mean (green diamonds), median (orange horizontal lines), 25th and 75th percentiles (box limits), and 5th and 95th percentiles (whiskers). The statistical significance ($p < 0.05$) of the difference in mean ratios of adjacent precipitable water bins is indicated by the symbols between the box plots, where “–” and “+” denote a statistically significant decrease and a statistically significant increase, respectively, of the ratio with respect to PW (higher PW bin minus lower PW bin).

Amplification Factor vs Precipitable Water

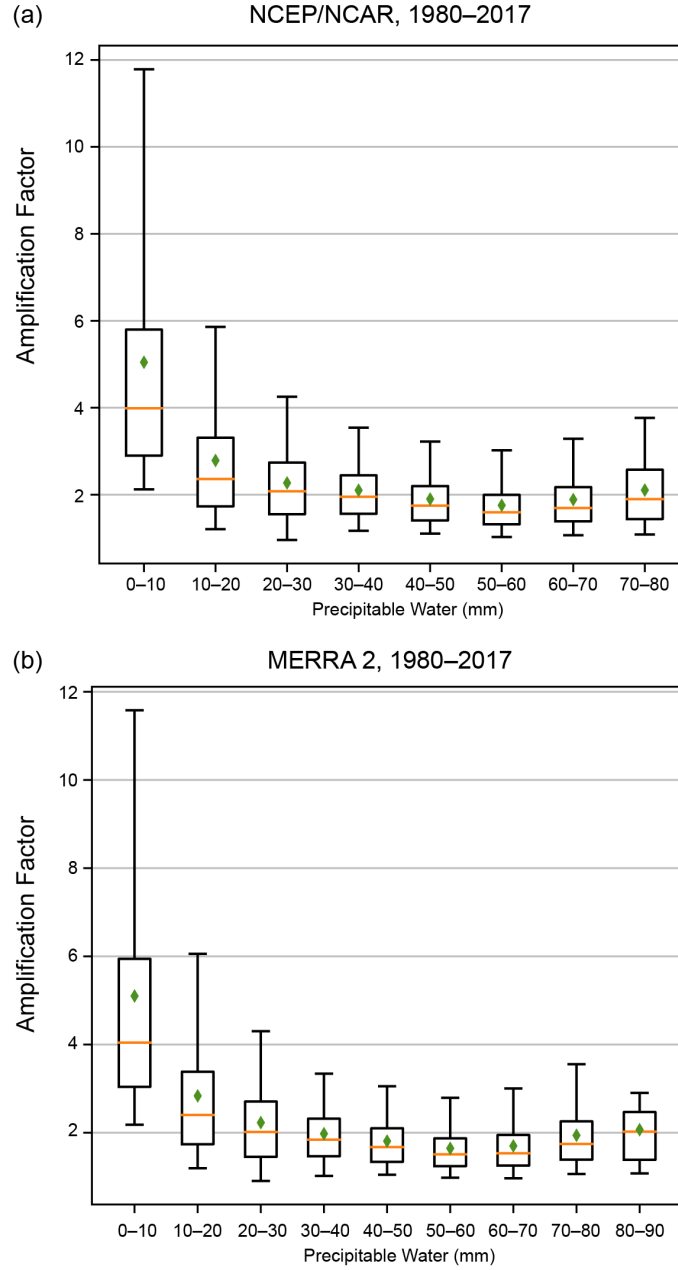


Figure A6. Boxplot distributions for the 1-yr, 1-day PDS of the amplification factor A (EP/PW) for (a) NCEP/NCAR, 1980–2017, and (b) MERRA-2, 1980–2017. Boxplot parameters include mean (green diamonds), median (orange horizontal lines), 25th and 75th percentiles (box limits), and 5th and 95th percentiles (whiskers).

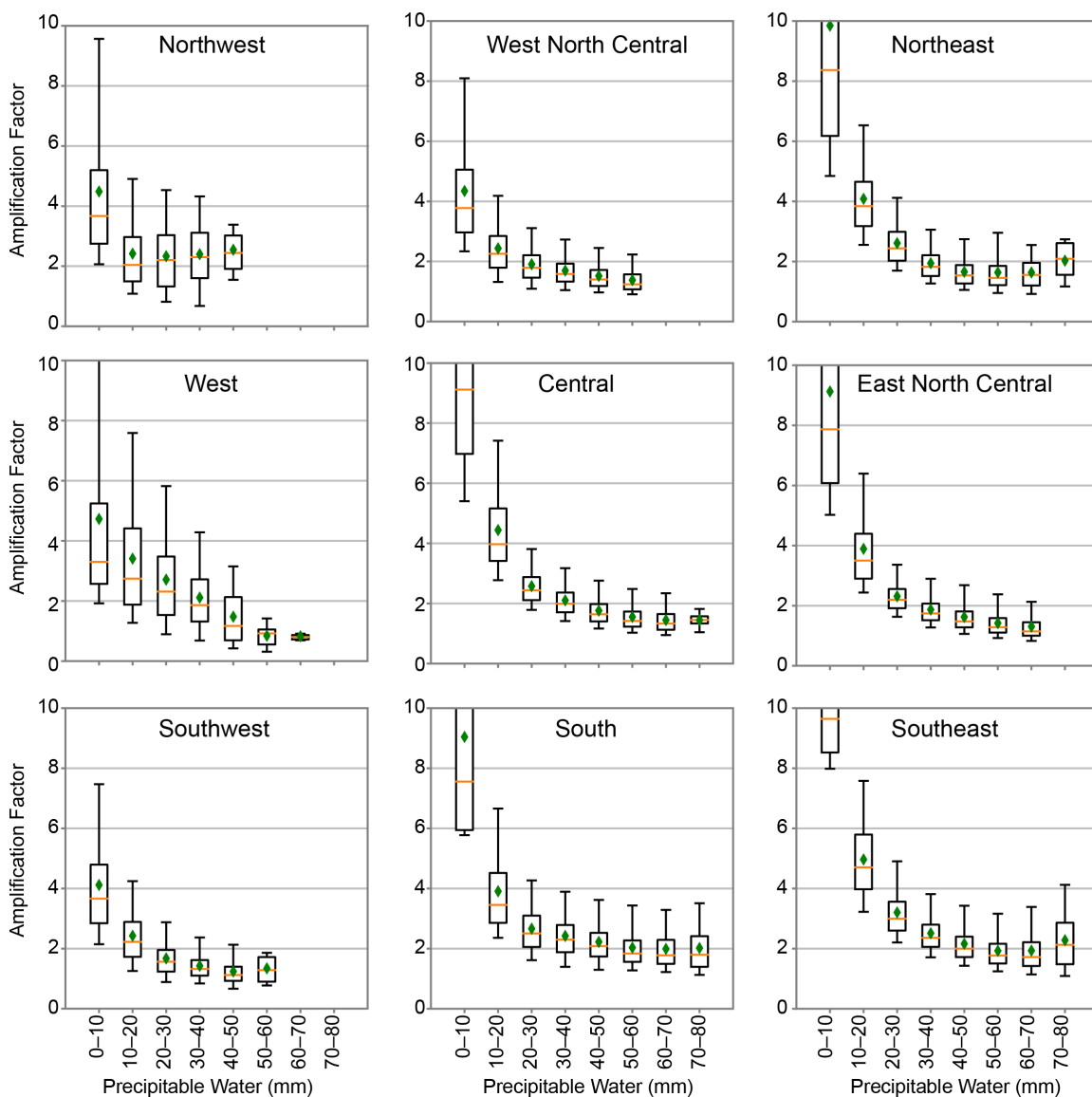


Figure A7. Regional boxplot distributions of the ratio of 1-yr, 1-day EP to the same-day 3-hour maximum PW for 10 mm intervals. Boxplot parameters include mean (green diamonds), median (orange horizontal lines), 25th and 75th percentiles (box limits), and 5th and 95th percentiles (whiskers).

Scientific/Technical Publications

- Biard, J.C. and K.E. Kunkel, 2019: Automated detection of weather fronts using a deep learning neural network. *Advances in Statistical Climatology, Meteorology and Oceanography*, **5** (2), 147–160. <http://dx.doi.org/10.5194/ascmo-5-147-2019>
- Champion, S.M., 2017: The importance of summer season fronts in extreme precipitation events [abstract]. *23rd Conference on Applied Climatology of the American Meteorological Society*, Asheville, NC, June 27, 2017.
- Kunkel, K.E., 2017: Climate change adjustments for Intensity-Duration-Frequency extreme precipitation values [abstract]. *Annual Meeting of the American Meteorological Society*, Seattle, WA, January 24, 2017.
- Kunkel, K.E., 2017: DoD needs: Memories of the past and a look to the future [abstract]. Army Research Laboratory, White Sands Missile Range, NM, September 25, 2017.
- Kunkel, K.E. and J. Biard, 2017: Front detection in MERRA and NARR [abstract]. *MERRA-2 Applications Workshop*, NASA Goddard Space Flight Center, Greenbelt, MD, June 19, 2017.
- Kunkel, K.E. and D.R. Easterling, 2017: Effect of global warming on extreme precipitation design values [abstract]. *SERDP/ESTCP Symposium 2017: Enhancing DoD's Mission Effectiveness*, Washington, DC, November 28, 2017.
- Kunkel, K.E. and D.R. Easterling, 2017: An approach toward Incorporation of global warming effects into Intensity-Duration-Frequency values [abstract]. *Fall Meeting of the American Geophysical Union*, New Orleans, LA, December 12, 2017.
- Kunkel, K.E., D.R. Easterling, and T.R. Karl, 2017: Climate change adjustments for Intensity-Duration-Frequency extreme precipitation values [abstract]. *Annual Meeting of the American Meteorological Society*, Seattle, WA, January 24, 2017.
- Kunkel, K.E., J. Biard, and E. Racah, 2018: Automated detection of fronts using a deep learning algorithm [abstract]. *Annual Meeting of the American Meteorological Society*, Austin, TX, January 10, 2018.
- Kunkel, K.E., J. Biard, and L. Sun, 2018: Impacts of weather system changes on future extreme precipitation design values [abstract]. *Fall Meeting of the American Geophysical Union*, Washington, DC, December 11, 2018.
- Kunkel, K.E. and S.M. Champion, 2018: The meteorology of extreme precipitation and implications for future planning [abstract]. *Annual Meeting of the American Meteorological Society*, Austin, TX, January 9, 2018.
- Kunkel, K.E. and D.R. Easterling, 2018: Effect of global warming on weather systems causing extreme precipitation [abstract]. *SERDP/ESTCP Symposium 2018: Enhancing DoD's Missions Effectiveness*, Washington, DC, November 27, 2018.
- Kunkel, K.E., 2019: Extreme precipitation and climate change: Observations and projections [abstract]. *Association of State Dam Safety Officials Dam Safety 2019 Conference*, Orlando, FL, September 9, 2019.

- Kunkel, K.E., 2019: Effects of anthropogenically-forced global warming on the risks of extreme rainfall and flooding [abstract]. *Association of Environmental and Engineering Geologists 62nd Annual Meeting*, Asheville, NC, September 18, 2019.
- Kunkel, K.E. and S.M. Champion, 2019: An assessment of rainfall from Hurricanes Harvey and Florence relative to other extremely wet storms in the United States. *Geophysical Research Letters*, **46** (22), 13500–13506. <http://dx.doi.org/10.1029/2019GL085034>
- Kunkel, K.E. and D.R. Easterling, 2019: Incorporation of the effects of future anthropogenically-forced climate change in Intensity-Duration-Frequency design values [abstract]. *SERDP/ESTCP Symposium 2019: Enhancing DoD's Missions Effectiveness*, Washington, DC, December 3, 2019.
- Kunkel, K.E., S. Stevens, L. Stevens, and T. Karl, 2019: Observed climatological relationships between precipitable water and extreme precipitation in the contiguous United States [abstract]. *Fall Meeting of the American Geophysical Union*, San Francisco, CA, December 13, 2019.
- Kunkel, K.E., 2020: Extreme precipitation and climate change: Observations and projections. *ASDO Journal of Dam Safety*, 17(3), 22-28.
- Kunkel, K.E., 2020: Extreme precipitation and climate change: Observations and projections [abstract]. *FEMA National Dam Safety Program Technical Seminar (NDSPTS): Dam and Levee Resiliency in the Era of Intensifying Natural Hazards and Climate Conditions*, Emmitsburg, MD, February 19, 2020.
- Kunkel, K.E., T.R. Karl, M.F. Squires, X. Yin, S.T. Stegall, and D.R. Easterling, 2020: Trends and relationships with average precipitation and precipitable water in the contiguous United States. *Journal of Applied Meteorology and Climatology*, **59** (1), 125-142. <http://dx.doi.org/10.1175/JAMC-D-19-0185.1>
- Kunkel, K.E., S. Stevens, L. Stevens, and T. Karl, 2020: Observed climatological relationships between precipitable water and extreme precipitation in the contiguous United States [abstract]. *Annual Meeting of the American Meteorological Society*, Boston, MA, January 14, 2020.
- Kunkel, K.E., S.E. Stevens, L.E. Stevens, and T.R. Karl, 2020: Observed climatological relationships of extreme daily precipitation events with precipitable water and vertical velocity in the contiguous United States. *Geophysical Research Letters*, **47**, e2019GL086721. <http://dx.doi.org/10.1029/2019GL086721>
- Paquin, D., A. Frigon, and K.E. Kunkel, 2016: Evaluation of total precipitable water from CRCM4 using the NVAP-MEaSURES dataset and ERA-Interim reanalysis data. *Atmosphere-Ocean*, **54** (5), 541–548. <http://dx.doi.org/10.1080/07055900.2016.1230043>
- Prat, O.P., R.D. Leeper, S.E. Stevens, B.R. Nelson, D.R. Easterling, and K.E. Kunkel, 2016: Long-term quantification of extreme precipitation in relation with tropical and extra-tropical cyclonic activity over the Carolinas. *Proceedings, Carolinas Climate Resilience Conference*, Charlotte, NC, September 12–14, 2016.